

INFORMATION TO USERS

This manuscript has been reproduced from the microfilm master. UMI films the text directly from the original or copy submitted. Thus, some thesis and dissertation copies are in typewriter face, while others may be from any type of computer printer.

The quality of this reproduction is dependent upon the quality of the copy submitted. Broken or indistinct print, colored or poor quality illustrations and photographs, print bleedthrough, substandard margins, and improper alignment can adversely affect reproduction.

In the unlikely event that the author did not send UMI a complete manuscript and there are missing pages, these will be noted. Also, if unauthorized copyright material had to be removed, a note will indicate the deletion.

Oversize materials (e.g., maps, drawings, charts) are reproduced by sectioning the original, beginning at the upper left-hand corner and continuing from left to right in equal sections with small overlaps.

Photographs included in the original manuscript have been reproduced xerographically in this copy. Higher quality 6" x 9" black and white photographic prints are available for any photographs or illustrations appearing in this copy for an additional charge. Contact UMI directly to order.

ProQuest Information and Learning
300 North Zeeb Road, Ann Arbor, MI 48106-1346 USA
800-521-0600

UMI[®]

A TWO-DIMENSIONAL, SELF-CONSISTENT MODEL OF
GALACTIC AND ANOMALOUS COSMIC RAYS IN THE SOLAR
WIND

by
Vladimir A. Florinski

A Dissertation Submitted to the Faculty of the
DEPARTMENT OF PLANETARY SCIENCES

In Partial Fulfillment of the Requirements
For the Degree of

DOCTOR OF PHILOSOPHY

In the Graduate College

THE UNIVERSITY OF ARIZONA

2001

UMI Number: 3010247

UMI[®]

UMI Microform 3010247

Copyright 2001 by Bell & Howell Information and Learning Company.

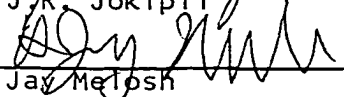
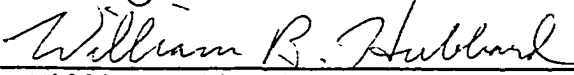
All rights reserved. This microform edition is protected against
unauthorized copying under Title 17, United States Code.

Bell & Howell Information and Learning Company
300 North Zeeb Road
P.O. Box 1346
Ann Arbor, MI 48106-1346

THE UNIVERSITY OF ARIZONA @
GRADUATE COLLEGE

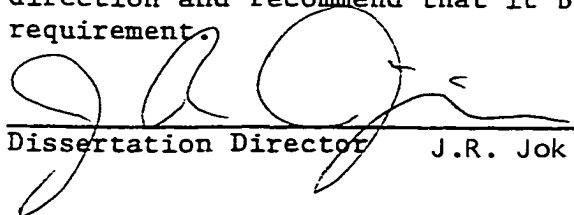
As members of the Final Examination Committee, we certify that we have read the dissertation prepared by Vladimir A. Florinski entitled A TWO-DIMENSIONAL, SELF-CONSISTENT MODEL OF GALACTIC AND ANOMALOUS COSMIC RAYS IN THE SOLAR WIND

and recommend that it be accepted as fulfilling the dissertation requirement for the Degree of Doctor of Philosophy

 _____ J.R. Jokipii	<u>4/12/01</u> Date
 _____ Jay Melosh	<u>4/12/01</u> Date
 _____ William Hubbard	<u>4/12/01</u> Date
 _____ Adam Burrows	<u>4/12/2001</u> Date
 _____ Matthias Steinmetz	<u>4/12/2001</u> Date

Final approval and acceptance of this dissertation is contingent upon the candidate's submission of the final copy of the dissertation to the Graduate College.

I hereby certify that I have read this dissertation prepared under my direction and recommend that it be accepted as fulfilling the dissertation requirement.

 _____ Dissertation Director J.R. Jokipii	<u>4/12/01</u> Date
--	------------------------

ACKNOWLEDGMENTS

I would like to express my deep gratitude to my advisor, Professor Randy Jokipii, for suggesting the topic, and greatly contributing to this work by sharing his exceptional knowledge of the physics of cosmic rays with me. This dissertation wouldn't have been possible without his expertise in cosmic-ray modeling. I am also thankful to Professor Jokipii for financially supporting me in a Research Assistant position in the Department.

I would like express my thanks to Dr. Joe Giacalone and Dr. Jozsef Kota for helpful discussions concerning the subject of this work, on several occasions. I acknowledge useful discussions with Dr. Aramais Zacharian, a fellow graduate student, concerning numerical methods. Many thanks to the members of my dissertation committee, especially to Professor Adam Burrows and Professor Jay Melosh, for pointing out errors in the draft version of the thesis.

I am grateful to my wife Luba for her support and care during times that were very difficult for me. Finally, thanks to my little son, Andre, for our time together, that made my life more complete and meaningful.

TABLE OF CONTENTS

LIST OF FIGURES	7
LIST OF TABLES	9
ABSTRACT	10
INTRODUCTION	11
CHAPTER 1 COSMIC RAYS IN THE HELIOSPHERE: INTRODUCTION TO THE THEORY	18
1.1 Cosmic-ray transport and modulation	18
1.2 Anomalous cosmic ray acceleration	25
1.3 Self-consistent models of the heliosphere	33
CHAPTER 2 GALACTIC COSMIC RAYS IN A 2-DIMENSIONAL MODEL	43
2.1 Introduction	43
2.2 Solar wind model	46
2.3 Magnetic field equations	50
2.4 Cosmic-ray model	54
2.5 Numerical method for the wind	60
2.6 Numerical method for the CR equation	68
2.7 Results: solar wind effects produced by the cosmic rays	70
2.8 Results: cosmic ray distribution	75
2.9 Discussion	83

TABLE OF CONTENTS – *Continued*

CHAPTER 3 ANOMALOUS COSMIC RAYS IN A SELF-CONSISTENT MODEL	85
3.1 Introduction	85
3.2 New solar wind–PUI model	87
3.3 New ACR model	93
3.4 Adaptive mesh refinement technique	98
3.5 Numerical integration of the cosmic–ray equation	106
3.6 Grid structure and the solar wind flow	109
3.7 Anomalous cosmic–ray distribution and spectra	117
3.8 Discussion	124
CONCLUSIONS AND FUTURE WORK	127
APPENDIX A 3-FLUID PUI-SOLAR WIND EQUATIONS	130
APPENDIX B SPECTRAL "BUMP" IN SPHERICALLY-SYMMETRIC GEOMETRY	135
LIST OF ACRONYMS USED IN THE TEXT	141
REFERENCES	142

LIST OF FIGURES

Figure I.1 A schematic view of the heliosphere as seen from above the ecliptic plane along the north polar axis.	12
Figure 2.1 A schematic view of the heliosphere used by the self-consistent model.	44
Figure 2.2 Wind velocity and streamlines for the case $A > 0$	71
Figure 2.3 Same as Fig. 2.2, but for $A < 0$	72
Figure 2.4 Radial profiles of the wind speed, plasma pressure and cosmic ray pressure for $A > 0$ and $A < 0$	74
Figure 2.5 Cosmic-ray intensity contours for 1.6GeV protons for $A > 0$	76
Figure 2.6 Same as Fig. 2.5, but for $A < 0$	77
Figure 2.7 Same as Fig. 2.5, but for 72MeV protons.	78
Figure 2.8 Same as Fig. 2.7, but for $A < 0$	79
Figure 2.9 GCR spectra at 0 and 90 degrees latitude for $A > 0$	81
Figure 2.10 Same as Fig. 2.9, but for $A < 0$	82
Figure 3.1 Solar wind number density, velocity and momentum flux at 1AU as a function of latitude.	92
Figure 3.2 "Snapshots" of the AMR grid generation procedure used in this work.	103
Figure 3.3 Computer representation of the adaptive mesh hierarchy based on an object-oriented model.	105
Figure 3.4 Grid structure for case I.	108
Figure 3.5 Radial solar wind velocity contours for case I (TS between 80 and 90 AU).	110
Figure 3.6 Same as Figure 3.5, but for case II (shock between 90 and 100 AU).	111

LIST OF FIGURES – *Continued*

Figure 3.7 Radial SW velocity, gas and ACR pressures, and expanded SW velocity profiles for cases I and II.	113
Figure 3.8 Same as Figure 3.7, but for case II.	114
Figure 3.9 Solar wind proton density and pickup ion number density for 0° and 90° latitude.	115
Figure 3.10 10MeV ACR intensity profiles for case I.	118
Figure 3.11 Same as Figure 3.10, but for case II.	119
Figure 3.12 Computed ACR spectra for case I at 30° latitude.	121
Figure 3.13 Same as in Figure 3.12, but for case II.	122
Figure 3.14 Magnified ACR spectra before the cutoff for case I for four different latitudes at the shock.	123
Figure B.1 Particle spectra resulting from solving two different transport equations with both a jump in the transport coefficients (κ , u) and a smooth shock.	136
Figure B.2 Particle concentration at the source, according to Eq. (B.4).	138

LIST OF TABLES

I.1 A summary of existing self-consistent cosmic ray models.	15
3.1 Solar wind parameters at 1 AU.	93
C.1 A comparison of the dynamical effects of the various particle species.	128

ABSTRACT

We have developed a two-dimensional heliospheric model that includes galactic and anomalous cosmic rays as well as pickup ions. Cosmic rays are described via their number density in phase space, rather than pressure, as every preceding 2-D model has done. Cosmic-ray pressure is included in the total energy budget, allowing us to compute dynamical effects of the energetic particles on the solar wind. We include the magnetic field as well in order to consistently compute cosmic-ray diffusion coefficients. To accommodate lower-energy cosmic rays with their short diffusion length, we implemented an adaptive mesh refinement code featuring improved spatial resolution near the termination shock.

Our simulations show that galactic cosmic rays could substantially change the solar wind flow in the outer heliosphere. In particular, the solar wind is deflected towards the ecliptic plane during the positive solar cycle, resulting in faster wind near the current sheet. This is a result of large latitudinal gradients in the cosmic-ray pressure, caused by the difference in cosmic-ray drift patterns over latitude.

We also found that anomalous cosmic rays have a minor effect on the solar wind. Their pressure is not sufficient to modify the termination shock significantly, a conclusion based on comparing model cosmic-ray spectra with observations. However, anomalous cosmic-ray acceleration occurs somewhat differently than thought before, and shock drift effects are not prominent. The spectra of these particles have an enhancement near the cutoff, that is not caused by shock drifts.

INTRODUCTION

This work sets its goal to study in detail one of the central problems of space physics: the interaction between the high and low energy particle (mostly proton) populations in the Solar System. The low energy or thermal population has its origin in the solar corona, the hot ($2 \times 10^6 \text{K}$) outermost layer of the solar atmosphere, which is expanding in all directions into interplanetary space at high speed forming the solar wind (SW). This highly supersonic flow creates a "bubble" filled with solar plasma around the Sun, of roughly 150–300AU (astronomical units) in size, called the heliosphere. The size and shape of the heliosphere is determined by the density and temperature in the local interstellar medium (LISM), surrounding the Solar System, as well as by the motion of the Solar System relative to the LISM. Interaction between the solar wind and the interstellar medium creates a complex flow structure with several distinct surfaces (called discontinuities) separating flows with drastically different velocities and densities.

Two steady-state discontinuity surfaces are predicted within the heliosphere: the termination shock (TS) and the heliopause (HP) (Figure I.1). The former occurs because the solar wind must slow down to match velocity and pressure in the LISM. Such a transition from a supersonic flow to subsonic can only happen as a velocity jump (shock wave), because signals cannot propagate backwards (towards the Sun) in the supersonic wind and therefore are unable to communicate the presence of the LISM to establish a gradual slowdown. The heliocentric distance to the TS is estimated to be between 80 and 120AU. The heliopause, on the other hand, is a contact discontinuity (i.e., a surface without a flow of a gas across), separating the solar wind from the interstellar plasma,

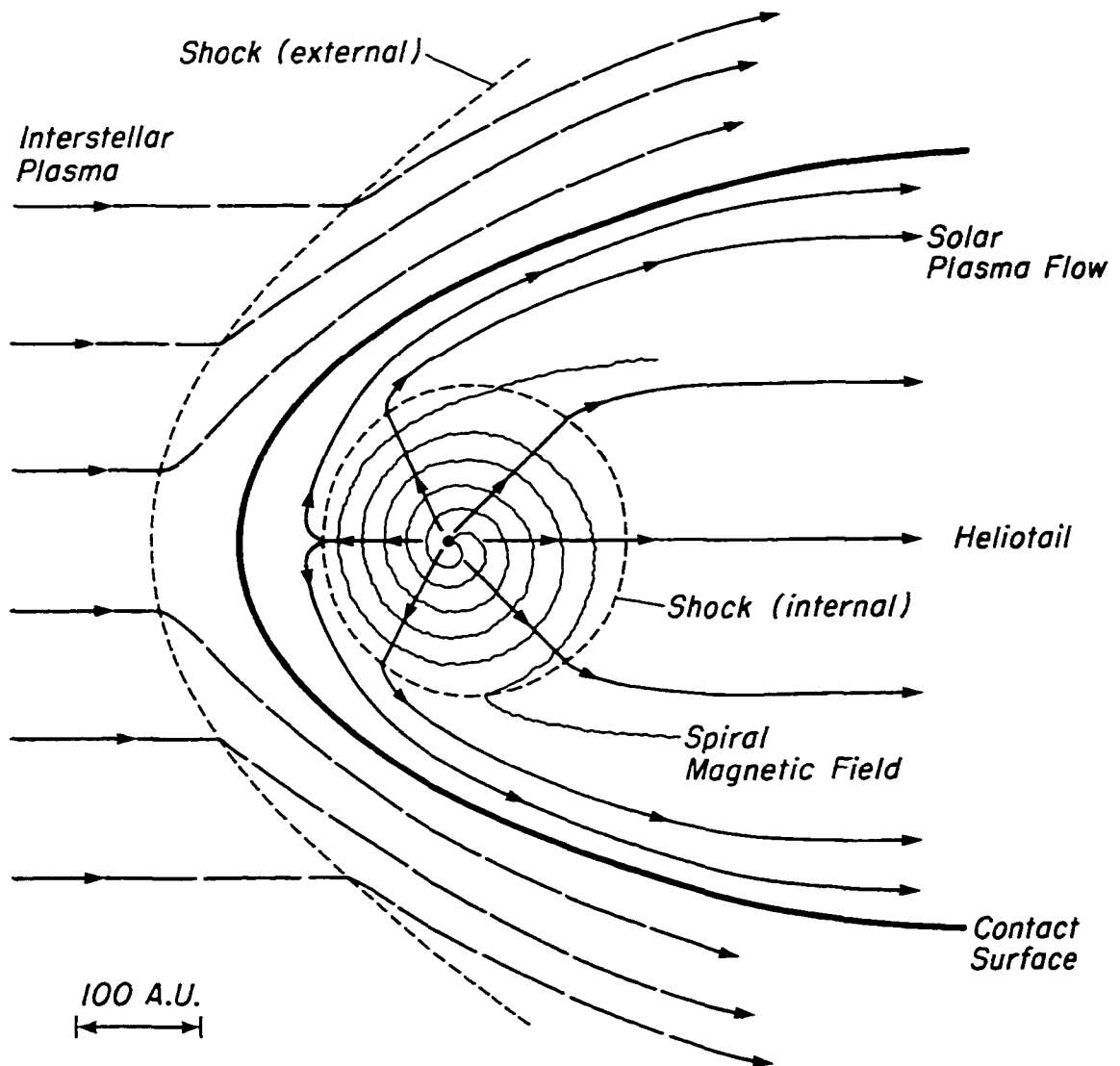


Figure I.1 A schematic view of the heliosphere as seen from above the ecliptic plane along the north polar axis. The "internal shock" is the termination shock, and the "contact surface" is the heliopause. Lines with arrows show the direction of the plasma flow. Graphic by J. R. Jokipii.

that flow along each other parallel to the contact surface. Across the surface, the pressure of the tenuous hot solar wind plasma is exactly balanced by the pressure of the cold, but dense, interstellar plasma. The heliopause is estimated to lie between 100 and 150AU in the direction of the interstellar wind (the "nose" of the HP), but farther away in other directions, and is considered the boundary of the heliosphere. The third surface, the bow shock, forms in the interstellar medium, but is not, technically, part of the heliosphere. Modern reviews of the heliospheric structure can be found in *Suess (1990)* and *Suess and Nerney (1997)*.

The high-energy particle population is referred to as cosmic rays (CR). Two major CR populations are observed in the heliosphere: galactic (GCR) and anomalous (ACR). GCRs are very high energy and originate outside the Solar System, while ACRs originate in the outer heliosphere and have lower energies. The third CR component, the solar cosmic rays, has even lower energies and will not be discussed here.

While the basic structure of the plasma flow in and around the heliosphere is now well understood, cosmic rays present certain challenges. Propagation of these particles from their origin is a complicated process, involving particles moving along, or across, the magnetic fields (MF) present in the interplanetary plasma. Knowledge of the structure of these fields is required in order to understand the particle transport. The large-scale field configuration, well understood now, consists of two sets of Archimedian spirals, with the field directed oppositely in the northern and the southern solar hemisphere and separated by the so called neutral sheet (HNS) (*Parker, 1965*). Because of the specific MF pattern on the Sun, involving regions of open field lines (coronal holes) and closed field lines (the streamer belt), the solar wind is faster at high latitudes and slower near the

heliographic equator. This pattern is not static: due to the solar magnetic field reversal every 11 years the region of slow wind expands or contracts and the interaction between the streams of different speeds creates shock structures called corotating interacting regions (CIRs). So far much of the study of the CR propagation has been focusing on a simpler case of the solar minimum (time when the solar magnetic dipole axis is essentially co-aligned with its rotational axis) and this is the path taken in this work. An outline of problems in modeling CR propagation during the changing solar cycle can be found in *Potgieter* (1993, 1995).

Besides the large-scale MF structure there exist smaller-scale irregularities (turbulence), caused by random processes on the solar surface or by the interaction between the solar wind and the interstellar medium. These irregularities cause the cosmic rays to carry out a random walk, also known as diffusion. The diffusion coefficients are model-dependent; finding appropriate diffusion coefficients to explain the observed CR measurements is one of the principal goals of the modulation theory. A review on CR propagation in the heliosphere can be found in *Jokipii* (1997), while a review of modern modulation models with references can be found in Section 1.1.

The picture of the heliosphere outlined above is complicated by the fact that the high and the low energy populations are interacting with each other. The physical nature of this interaction is discussed in some detail in Section 1.3. In addition, an intermediate energy solar wind component, consisting of the former interstellar neutral atoms, ionized in the wind, also needs to be accounted for. This component, called the pickup ions (PUI) serves as a seed population for the ACRs. Acceleration of particles to ACR energies is discussed in Section 1.2.

This work is a result of research conducted by the author during 1997–2001 when the author was a graduate student in the Department of Planetary Sciences at the University of Arizona. Presented here is the first ever 2–dimensional kinetic model including the two CR species self–consistently interacting with the solar wind. Pickup ions are also included, although in a somewhat limited fashion.

Table I.1 A summary of existing self–consistent cosmic ray models.

	1–D	2–D solar wind	2–D global	3–D
Fluid CR	<i>Ko et al. (1988)</i> <i>Banaszkiewicz and Ziemkiewicz (1997)</i>	<i>Fahr et al. (1992)</i>	<i>Myasnikov et al. (2000)</i> <i>Fahr et al. (2000)</i>	–
Kinetic CR	<i>Le Roux and Fichtner (1997)</i>	<i>Florinski and Jokipii (1999)</i> This work	–	–

Table I.1 presents a summary of major papers on self–consistent cosmic–ray models. Section 1.3 analyzes each particular model in detail. At this point we would only like to point out that "2–D solar wind models" provide a better description of the inner heliosphere, but are restricted to the region inside the heliopause, while "2–D global models" include a larger region of space around the heliosphere at the expense of losing some details of the CR transport. This distinction is discussed more extensively in Sections 1.3 and 2.1. "Fluid" CR models are so called because they use integral (over momentum) quantities (usually pressure) to describe the cosmic rays, so that the latter are considered a second fluid. Kinetic models use the phase space distribution function (PSD), that depends on both spatial coordinates and particle energy, thus providing a considerably higher degree of detail.

We believe that extension of 1–D kinetic models to two dimensions (or upgrade of 2–

D fluid models with kinetic CR description), done in this work, is an important step in understanding the physical processes of the cosmic-ray-solar-wind interaction. Specifically, the 2-D extension allows inclusion of drift motions, non-uniform solar wind, and latitude-dependent PUI production, while the advantage of the kinetic approach is the availability of the particle spectra, which can be directly compared with the observations, plus the use of more realistic (energy-dependent) diffusion coefficients. A sophisticated numerical model was created that has the potential to be used in global (possibly, 3-dimensional) heliospheric simulations. A number of important results were obtained, showing that cosmic-ray-solar-wind interaction may be somewhat different than previously thought.

This work consists of three chapters. Chapter 1 provides a detailed review of modulation and acceleration of the cosmic rays as well as self-consistent models. Chapter 2 focuses on GCR effects on the solar wind in two dimensions. In this chapter we will show that the overall pattern of the solar wind flow can change significantly due to latitudinal gradients in GCR distribution. In particular, the wind downstream of the TS is deflected either towards the pole or towards the equator, depending on the solar cycle, an effect not seen in 1-dimensional models. In Chapter 3 we study acceleration of anomalous cosmic rays as well as their production from the pickup ion distribution. We find that ACRs have an insignificant effect on the solar wind, for a range of plausible shock locations and injection rates. A set of equations, describing the two-temperature solar-wind-pickup-ion system is derived in Appendix A. Finally, an interesting new feature has been identified in ACR spectra at intermediate (tens of MeV) energies. This spectral enhancement, or "bump" appears to be a 1-dimensional effect, most prominent

when the CR diffusion coefficient undergoes a jump at the shock. We devote Appendix B to discussing this phenomenon in some detail.

A reader may notice that three cells in Table I.1 are left blank. We believe that the model presented in this paper can be extended in the future to include the region outside the heliopause, i.e., become a global heliospheric model. Such extension would require considerable computing power, but is not very difficult conceptually. The problems one would expect to encounter are discussed in the Conclusions Section. The ultimate goal in the future will be to build a complete 3-dimensional model of the heliosphere, including every major constituent of the SW and the LISM, as well as the cosmic rays. We believe that this work is an important step in achieving this goal.

CHAPTER 1

COSMIC RAYS IN THE HELIOSPHERE: INTRODUCTION TO THE THEORY

1.1 Cosmic-ray transport and modulation

The solar wind and its frozen-in magnetic field have a profound effect on the propagation of galactic cosmic rays within the heliosphere. First, the wind sweeps these particles away with the solar wind speed; this is equivalent to a transformation from the comoving frame where their distribution is isotropic. Second, particles experience guiding center drifts in nonuniform magnetic fields, such as the Parker's spiral field. In addition, small-scale irregularities in the form of Alfvén and magnetosonic waves are always present in the interplanetary medium superimposed over the large-scale magnetic field. A random superposition of such waves (turbulence) is capable of scattering the particles in pitch angle with the result that they execute random walk or diffusive motion. Finally, cosmic rays experience energy loss (adiabatic cooling) due to the expansion of the solar wind into interplanetary space. The change in particle number density and spectra as a result of all these processes is called solar modulation.

Any study of the cosmic-ray modulation begins with the energetic particle transport equation (e.g., *Parker 1965, Dolginov and Toptygin 1967, Gleeson and Axford 1967, Gleeson 1969*) which can be written, in its modern form, as follows:

$$\frac{\partial f}{\partial t} + \mathbf{u}_i \frac{\partial f}{\partial x_i} - \frac{\partial}{\partial x_i} \left(\kappa_{ij} \frac{\partial f}{\partial x_j} \right) = \frac{1}{3} \frac{\partial u_i}{\partial x_i} p \frac{\partial f}{\partial p}. \quad (1.1)$$

Here $f(t, x_i, p) = dN / (4\pi p^2 dp d^3x)$, N being the number of particles, is the cosmic-ray phase space density, which is a function of time t , position r_i and momentum p , \mathbf{u} is the flow velocity and κ_{ij} is the diffusion tensor. The particle distribution is assumed to be isotropic in momentum, which requires, in general, that the particle velocity $w \gg u$ (the wind speed). A more specific derivation of this criterion applied to the termination shock conditions is provided in Chapter 3. The second term in Eq. (1.1) contains the electric drift, the third diffusion and gradient/curvature drifts, and the fourth the adiabatic cooling.

The nature of the diffusion is quite different in the directions parallel and perpendicular to the mean magnetic field \mathbf{B} . Scattering in pitch-angle (the angle between the particle velocity vector and the direction of the MF), for example, mostly causes particles to diffuse parallel to the field, while diffusion perpendicular to the field is probably caused by the random walk of the field lines themselves, as a result of convection on the solar surface (*Jokipii, 1971*). The diffusion coefficient is, in general, a tensor and can be written as

$$\kappa_{ij} = \kappa_{\perp} \delta_{ij} + \frac{(\kappa_{\parallel} - \kappa_{\perp}) B_i B_j}{B^2} + \frac{pcw}{3e} \epsilon_{ijk} \frac{B_k}{B^2}. \quad (1.2)$$

The last term contains the particle drift velocity (*Rossi and Olbert, 1970*) which can also be written as

$$\mathbf{v}_d = \frac{pcw}{3e} \nabla \times \frac{\mathbf{B}}{B^2}, \quad (1.3)$$

where c is the speed of light and e is the elementary charge (in this paper we assume everywhere that all positively charged particles are protons). Equation (1.1) is often written in a form where only the symmetric diffusion tensor components are included in κ_{ij} , while the drift term is added to the convection term as $v_{di}\partial f/\partial x_i$.

Modulation theory sets its goal to find solutions to the transport equation (1.1) that adequately describe the particle distributions observed by instruments (usually spacecraft-based). Early work in this area focused on finding analytic solutions under the approximation of a spherical symmetry (hence, no drifts were allowed). Assuming a constant speed solar wind (a good approximation beyond 1AU), this equation reduces to

$$u \frac{\partial f}{\partial r} - \frac{1}{r^2} \frac{\partial}{\partial r} \left(r^2 \kappa_{rr} \frac{\partial f}{\partial r} \right) = \frac{2u}{3r} p \frac{\partial f}{\partial p}. \quad (1.4)$$

Modulation studies often omit the time-dependent term in the transport equation. Transport parameters vary on the timescale of the 11-year solar cycle which is usually larger than the dynamic timescale $r/u \sim 100\text{AU}/500\text{km/s} \sim 1\text{yr}$ or the diffusive timescale $r^2/\kappa \sim (100\text{AU})^2/10^{22}\text{cm}^2/\text{s} \sim 7\text{yrs}$ (100AU being the typical size of the heliosphere). Equation (1.4) also shows that cosmic rays evolve on spatial scales of the order of κ/u .

While solutions of equation (1.4) are, in general, quite complex because κ_{rr} is a function of both r and p , several simple analytic solutions exist for special cases. One is the so-called force-field solution, valid if $ur/\kappa \ll 1$, which corresponds to particles of energies above several hundred MeV. As shown in *Gleeson and Axford (1968)*, Eq. (1.4) reduces to the form similar to Liouville's theorem (conservation of phase space density), with an effective "force" $upw/3\kappa$. The solution is the unmodulated spectrum taken at a

different momentum p , which is a function of u , κ and r , i.e.,

$$f(r,p)=f(r_b,p(\zeta(p)+\phi(r))), \quad (1.5)$$

where r_b is the external modulation boundary, beyond which the particle distribution is set equal to their galactic spectrum. The functions ζ and ϕ depend on momentum and radial distance, respectively. In Eq. (1.5) it is implied that $p(\zeta)$ is the inverse function of $\zeta(p)$. This solution was found to be quite accurate when compared with numerical solutions for high energy GCRs by *Fisk et al.* (1969).

The second analytic solution corresponds to the lowest energy particles and small heliocentric distances. In this case $ur/\kappa \ll 0$ and the second term in (1.4) can be neglected. *Fisk et al.* (1973) (see also *Fisk*, 1979, p. 196) suggested that radial gradients should be very small in this case (this conclusion is based on observational evidence, there is apparently no solid theoretical explanation) and the only source of the low-energy particles is the cooled-off high-energy distribution. From (1.4) the solution is therefore simply

$$f(r,p)=\text{const.} \quad (1.6)$$

The main implication of this is that the spectral slope here is independent of the spectrum at large distances. The differential intensity (number of particles crossing a unit area in any direction per unit energy, per unit time), defined as $J=fp^2$, is proportional to T , where T is the kinetic energy. This spectral slope is seen in many modulation models (see, e.g., *Webber et al.*, 1990; *Burger and Hattingh*, 1996; also *le Roux et al.*, 1996 for a case of ACRs).

Several more complicated analytic solutions to equation (1.4) are available, obtained

by separating the variables using prescribed forms for the diffusion coefficient (*Webb and Gleeson, 1977; Webb, 1982; Webb et al., 1985*), see also a review by *Fisk (1979)*. *Owens and Jokipii (1971)* found analytic solutions to (1.1) in two dimensions under the assumption of a radially-directed magnetic field and energy-independent, but varying in latitude, diffusion. Their conclusion was that latitudinal dependence of κ_{ij} has little effect on the particle density in the inner heliosphere. Still, their model did not include drifts which turn out to be an important contributor to cosmic ray modulation.

The effects of gradient and curvature drifts in Eq. (1.1) were first studied by *Jokipii et al. (1977)*. The authors described particle drift patterns in the Parker's spiral field (*Parker, 1963*). For 11-year solar periods when B_r is directed away from the Sun in the northern hemisphere (this is historically named $A > 0$ case, where $A = B_{\oplus} r_{\oplus}^2$, subscript ' \oplus ' referring to values at 1AU), particles drift inward mostly along the polar axis and are expelled from the heliosphere along the current sheet, where magnetic field reverses its polarity. For $A < 0$ the direction of drifts is opposite, i.e., cosmic rays drift inwards along the ecliptic and exit in the polar region. Drift velocities in most of the heliosphere were found to exceed the convection speed u for particles with energies greater than a few MeV, resulting in reduced modulation of these particles. The work of *Jokipii et al. (1977)* demonstrated that drifts could not be neglected in modulation models. Since relevant analytic solutions become impossible to obtain (drifts are, by definition, a multidimensional phenomena), further modulation efforts concentrated on numerical solutions to Eq. (1.1).

Jokipii and Kopriva (1979) and *Jokipii and Davila (1981)* presented the first realistic 2-dimensional drift models for the GCR propagation. The first of these papers showed a

way to incorporate the singular drift velocity at the heliospheric neutral sheet as a boundary condition. Because the magnetic field changes polarity across the sheet, the drift velocity (1.3) contains a delta function. It can then be shown that condition of zero streaming flux at this boundary leads to a relation balancing ∂ diffusion into the current sheet and drift within the sheet.

A fully 3-dimensional model was presented in *Kota and Jokipii (1983)*. The authors included a "wavy" heliospheric neutral sheet and studied the dependence of the particle gradients on the tilt angle of the current sheet. Later, *Potgieter and Moraal (1985)* suggested a way to simulate a current sheet in 2 dimensions by spreading the singular drift velocity over a finite angle. This approach was shown to produce results consistent with the full 3-D model, as demonstrated in *Burger and Potgieter (1989)*.

Many attempts have been made to bring drift modulation models in agreement with the observations. The latter include both spectral features and spatial gradients inferred from the Voyagers 1 and 2 and Pioneer 10 as well as the Earth-orbiting IMP-8 (see, e.g., *Webber and Lockwood, 1987; Lockwood et al., 1988*). *Webber et al. (1990)* demonstrated that drift models predicted very different radial gradients for $A > 0$ and $A < 0$ cases, which apparently contradicted the observations available at the time. Additionally, latitudinal gradients predicted were too large due to easy polar access to the inner heliosphere, a result confirmed later, when Ulysses CR measurements became available (*Heber et al., 1996*). To remedy the situation, *Jokipii and Kota (1989)* proposed a modification of the Parker's spiral field in the polar regions. The idea is that convective motion of the magnetic field footpoints in the solar atmosphere produces a variable transverse component of the field that has a radial dependence of r^{-1} , unlike the radial

component which is $\sim r^{-2}$. While the average B_i of the modified field is zero, the average magnitude is not and in fact dominates B^2 beyond a few AU. This effectively reduces both drift (1.3) and diffusion (1.2) since both are inversely proportional to B^2 , resulting in smaller \mathcal{D} gradients. The presence of the fluctuations with the required timescales was confirmed by the Ulysses magnetic field measurements (*Jokipii et al., 1995*). Most later numerical models incorporated the Jokipii–Kota field in one form or another (*Haasbroek and Potgieter, 1995, Burger and Hattingh, 1998*), even though more recent Voyager and Pioneer measurements in the outer heliosphere appear to support the earlier notion of large differences in radial gradients during $A > 0$ and $A < 0$ solar minima, according to the usual drift concept (*Webber and Lockwood, 1997*).

Much of the contemporary research in the field of the GCR modulation is focusing on refining the existing models, e.g., by using different forms for the diffusion coefficients and drift modifications (e.g., in the strong scattering case). Recent reviews can be found in *Potgieter (1995, 1998)*. We should note that many of these models do not include the termination shock, but rather consider the shock to be the "modulation boundary" (*Haasbroek and Potgieter, 1995, Burger and Hattingh, 1995*). As shown in *Kota and Jokipii (1993)*, there exist discontinuous change in the CR radial gradients across the shock as a result of the streaming flux conservation. That the modulation region extends into the heliosheath (the region between the TS and the HP) has also received some observational evidence recently. *McDonald et al. (2000)* have found that GCR recovery time measured by Voyager 1 after a passage of a large-scale interplanetary disturbance, called global merged interaction region (GMIR) following the 1991 solar minimum was larger than the ACR recovery time with the implication that the GMIR continued to

modulate GCRs after it crossed the shock and moved into the heliosheath.

Finally, we would like to point out that, while the ability of the current modulation models to explain many of the CR features observed by spacecraft is remarkable, they do not necessarily provide deep insights into the actual transport mechanism, mostly because similar results can be obtained using different sets of parameters (i.e., diffusion coefficients and drift reduction), making it somewhat difficult to test the underlying CR transport theories.

1.2 Anomalous cosmic ray acceleration

Anomalous cosmic rays (ACRs) were first observed in early 1970s at the orbit of Earth as enhancements in the spectra of heavier ions (He^+ , N^+ , O^+) at about 10MeV per nucleon energy (*McDonald et al.*, 1974; *Garcia-Munoz et al.*, 1975; see also *Gloeckler*, 1979 for a review). It soon became clear that ACR do not come from the Sun but originate in the outer heliosphere. The concept for the origin of these particles as accelerated interstellar neutral atoms still stands today as first suggested by *Fisk et al.* (1974). As these authors suggested, ACRs start out as interstellar neutral atoms that, after entering the heliosphere, are ionized by charge exchange with the solar wind protons. They are then picked up by the solar wind and start drifting away from the Sun with velocity

$$\mathbf{u} = \frac{\mathbf{E} \times \mathbf{B}}{B^2} \quad (1.7)$$

until they encounter the termination shock. At the shock the ions are accelerated to hundreds of MeV, as originally predicted by *Pesses et al.* (1981) and later diffuse back towards the Sun where they are detected. While this theory is extremely popular, its ultimate test will come when the Voyager 1 spacecraft crosses the termination shock which is likely to happen within the next few years.

Work on ACRs in the past two decades has focused on two areas: injection of particles into the diffusive shock acceleration process and ACR acceleration and propagation. We will start with acceleration because this topic is much better understood. A common set of notations will be used, i.e., indices '1' and '2' will refer to up- and downstream values and [...] will designate jump conditions at the shock. The shock itself has a compression ratio $r=u_1/u_2$.

The diffusive shock acceleration theory was originally developed for quasiparallel shocks, for which the direction of the magnetic field B is parallel to the shock normal. Particles scatter off magnetic turbulence (which is essentially frozen into the solar wind) and gain energy by crossing the shock from the up- to downstream and back again. The average gain in momentum for one crossing of the shock in the fluid frame is (*Drury*, 1983)

$$\langle \Delta p \rangle = \frac{2}{3} \frac{p}{w} (u_1 - u_2), \quad (1.8)$$

Because $\Delta p \propto p$, this is a first order acceleration mechanism (similar to Fermi acceleration). Particles can reach high energies after crossing the shock multiple times.

Particle spectra resulting from shock acceleration can be obtained by solving the transport equation (1.1) and using the jump conditions for the cosmic rays at the shock.

Two such conditions are available. First, the distribution function itself must be continuous and second, the differential streaming flux \perp to the shock normal must also be continuous at the shock (*Drury, 1983*). This gives, in one dimension

$$[f]=0, \quad \left[\kappa_{xx} \frac{\partial f}{\partial x} + \frac{u_x}{3} p \frac{\partial f}{\partial p} \right] = 0, \quad (1.9)$$

where x is the direction of the shock normal. Solving (1.1) with boundary conditions of the type (1.9) is possible only for a few simple cases. For a 1-dimensional planar shock with κ_{xx} , u_x constant, the solution is especially simple (e.g., *Drury, 1983; Jones and Ellison, 1991*)

$$f(x,p) = Cp^{-a} \exp\left(\frac{u_{x,l}x}{\kappa_{xx,l}}\right), \quad \text{upstream} \quad (1.10)$$

$$f(x,p) = Cp^{-a}, \quad \text{downstream.}$$

The spectral index is dependent on the shock compression ratio and is given by

$$a = \frac{3u_2}{u_1 - u_2} = \frac{3r}{r-1}. \quad (1.11)$$

Notice that for a strong shock with $r=4$ Eq. (1.11) gives $f \sim p^{-4}$, a spectrum which produces unbound pressure at high energies (see Section 1.3). Real shocks are not infinite and the termination shock, in particular, has a finite curvature. Analytic solutions for spherical shocks are quite complicated, and only available for the case when $\kappa_{rr} \sim r$ and is independent of the particle's momentum (*Webb et al., 1985*). These authors found that the spectral slope of the ACR distribution is steeper than for the planar case and critically depends on the modulation parameter ur_{sh}/κ_{rr} . This parameter, it turns out, actually determines the maximum energy a particle can reach at a termination shock in a

spherically symmetric geometry. The distance to the modulation boundary also influences the cutoff energy because higher-energy particles are convected out and do not return to the shock.

While the above discussion applies to both parallel and perpendicular shocks, the latter offer another possibility for particle acceleration, as suggested by *Jokipii* (1982). He pointed out that the drift velocity parallel to the shock front is singular at the shock itself, meaning particles can drift along the shock face where they will be efficiently accelerated by the motional electric field. The streaming BC at the shock, similar to (1.9), should be written as

$$\left[\kappa_{xx} \frac{\partial f}{\partial x} + \frac{u_x}{3} p \frac{\partial f}{\partial p} - \frac{pcw}{3e} \frac{B_z}{B^2} \frac{\partial f}{\partial y} \right] = 0. \quad (1.12)$$

The solution is similar to (1.10) but the energy also depends on the distance that any given particle has drifted along the shock face. The energy gained this way at a finite shock can be estimated by taking the potential energy that a particle gains in the motional electric field, given by

$$\mathbf{E} = -\frac{1}{c}(\mathbf{u} \times \mathbf{B}), \quad (1.13)$$

as it drifts from the equatorial region towards the pole, for $A > 0$. For a Parker spiral field the typical energy of the particles accelerated by the electric field is

$$T_{ef} \sim \frac{euB_\phi r_{sh}}{c} \simeq \frac{eB_0 r_0^2 \Omega_0}{c}, \quad (1.14)$$

which is approximately 200MeV for $B_0 = 3 \times 10^{-7}$ Gs, independent of the shock location.

Several numerical models were presented to extend the analytic results to more

realistic solar wind conditions. In particular, *Potgieter and Moraal (1988)* studied the dependence of ACR spectra on the diffusion coefficient in the context of a spherically symmetric model. Because diffusion coefficients increase with energy, less energetic particles see the shock as planar, while higher energy particles are affected by the curvature of the shock. The relevant parameter is, again, ur_{sh}/κ_{rr} : when this is >1 , the shock can be approximated as planar and vice versa. Cosmic-ray spectra will fall off above the cutoff energy determined from

$$\kappa_{rr}(T_{curv}) \sim ur_{sh}. \quad (1.15)$$

Estimates show that T_{curv} is of the order of 10–100 MeV for protons, depending on the assumed form of the diffusion coefficient. Because of modulation lower energy particles are attenuated more and ACR spectra in the inner heliosphere will have maxima below the cutoff energy. Measurements show they do indeed exhibit maxima at predicted energies (*Cummings and Stone, 1998*).

Le Roux, Potgieter and Ptuskin (1996) presented a spherically-symmetric model with injection at the shock from the PUI population. Finding their results in general agreement with observed spectra, these authors also noted that the ACR energy density is comparable to the energy of the solar wind with implications that the shock could be strongly mediated by these particles.

Also, *Jokipii (1986)* has tested the idea of shock drift and acceleration at perpendicular shocks with a 2-dimensional model. His results show that high energy particle distributions peak at high latitudes for $A > 0$ and in the equatorial region for $A < 0$, according to the direction of the drift along the shock face. An important consequence of

this is that observed ACR spectra would be shifted towards higher energy for the $A < 0$ solar cycles.

Particle injection into the shock acceleration process described above is a much more controversial subject. *Jokipii* (1987) studied the applicability of the diffusion theory to particle acceleration at shocks for hard-sphere scattering (mentioned in Chapter 3). The idea is that particles drifting along the perpendicular shock must scatter often enough to redistribute perpendicular energy gains to maintain isotropy. This is not a problem for parallel shocks since particles can only cross the shock after they scatter up- or downstream. The condition for the applicability of the diffusion approximation at the shock in the classic scattering case can be shown to be (*Jones and Ellison, 1991, Webb et al., 1995*).

$$\begin{aligned} w \gg u, & \quad \text{parallel shocks} \\ w \gg u \frac{\lambda_{\parallel}}{r_g}, & \quad \text{perpendicular shocks.} \end{aligned} \quad (1.16)$$

The second condition would be modified if a different κ_{\perp} is used (such as the QLT result for field-line mixing). We derive a similar condition with a different assumptions regarding κ_{\perp} in Section 3.3. In any case, the following condition must be satisfied for acceleration to occur, as shown in *Jokipii* (1987)

$$\kappa_{rr} > ur_g, \quad (1.17)$$

which means that diffusion must be large enough for the particles to be able to move upstream. Clearly, this condition is more difficult to satisfy for perpendicular shocks for which $\kappa_{rr} \sim \kappa_{\perp} \ll \kappa_{\parallel}$.

Constraints of the kind of (1.16) show that, in general, diffusion-convection equations

similar to (1.1) cannot be used to study direct injection of the PUIs which only have $w \sim u$. A popular approach to lower energies is hybrid individual particle simulations (Giacalone *et al.*, 1994; Kucharek and Scholer, 1995; Ellison *et al.*, 1996) where protons are treated as individual particles while electrons are described as a fluid. Shock structure can be determined self-consistently and diffusion can be simulated by a prescribed scattering mechanism or by including turbulent electromagnetic fields. Results from hybrid simulations of Giacalone and Jokipii (1998) and Jones *et al.* (1998) confirm that direct PUI acceleration is possible at perpendicular shocks if turbulence is sufficiently strong. The former also showed that the field-line mixing regime for κ_{\perp} is much more efficient than classic scattering.

Besides direct PUI injection, several authors have proposed their pre-acceleration to low MeV energies either in other regions of the heliosphere or by a different mechanism. One theory, known as "shock surfing" (Zank *et al.*, 1996), is based on multiple reflections of low energy PUIs from the electrostatic potential within the subshock structure itself, caused by charge separation between protons and electrons. Efficient acceleration by the $\mathbf{u} \times \mathbf{B}$ electric field follows producing very hard particle spectra ($f \sim p^{-3}$) up to ~ 1 MeV, when particles are able to convect through the shock. The effectiveness of this mechanism depends on the thickness of the shock, since the reflective potential is large only for very thin shocks, of the order of the electron inertial length c/ω_{pe} , where $\omega_{pe} = (4\pi n e^2/m_e)^{1/2}$ is the electron plasma frequency. It is more likely, however, that strong shocks have a thickness $\sim c/\omega_{pp}$, where ω_{pp} is the proton plasma frequency (smaller by a factor $(m_e/m_p)^{1/2}$), in which case "shock surfing" will play

only a small role.

Besides the termination shock, several other pre-acceleration sites have been proposed. *Giacalone et al.* (1997) suggested that the first step in PUI acceleration occurs at the corotating interaction regions (CIRs) which are regions between the fast and the slow solar wind bounded by two propagating shock waves. Because propagating shocks move slowly relative to the solar wind, individual pickup ion velocities are much higher than u_1 in the shock frame, especially for PUIs ionized in the fast wind, i.e., the condition $w \gg u$ is more readily satisfied. Because interplanetary shocks are closer to quasi-parallel in the inner heliosphere, pre-acceleration will most likely occur within 10 AU solar distance.

Finally, stochastic or second order pre-acceleration of PUIs has also been considered as a source of injected ACRs (*le Roux and Ptuskin, 1998*). Acceleration is caused by resonant interaction of the PUIs with the circularly polarized MHD waves (Alfvén or ion-cyclotron) and can be represented by diffusion in momentum space. The authors computed self-consistently MHD wave spectra under the influence of wave damping by the PUIs. While second-order stochastic acceleration is inefficient and produces exponentially falling spectra, *le Roux and Ptuskin (1998)* find that some acceleration is possible inside CIRs, where the magnetic field is several times stronger than in the surrounding quiet solar wind.

1.3 Self-consistent models of the heliosphere

As discussed in the previous sections, energetic particles (cosmic rays and pickup ions) are accelerated and modulated in the heliosphere by the solar wind and its magnetic field. Because the energy density of the high-energy species is comparable to the energy density in the thermal plasma, we expect the solar wind to be modified by CR and PUI pressure gradients. Such a possibility was recognized quite early by *Axford and Newman* (1965) who suggested that galactic cosmic rays can, in principle, decelerate the wind assuming large gradients in GCR intensity existed (the effect predicted in that paper was actually too large). The general structure of a shock transition modified by CRs was studied by *Drury and Volk* (1981) and *Axford et al.* (1982) in a two-fluid hydrodynamic approximation. This approximation involves a fluid equation for the cosmic ray energy E_c or pressure P_c , derived by taking the second moment of Eq. (1.1). We can write in this case

$$\frac{\partial P_c}{\partial t} + u_i \frac{\partial P_c}{\partial x_i} - \frac{\partial}{\partial x_i} \left(\bar{\kappa}_{ij} \frac{\partial P_c}{\partial x_j} \right) + \gamma_c P_c \frac{\partial u_i}{\partial x_i} = Q_{in}, \quad (1.18)$$

where $\bar{\kappa}$ is diffusion coefficient, averaged over particle's energy, and γ_c is the adiabatic index for the cosmic rays. The last term describes injection from the solar wind or PUIs and will be discussed later. The adiabatic index relates CR pressure and energy according to

$$E_c = \frac{P_c}{\gamma - 1}. \quad (1.19)$$

The CR pressure itself is computed from the distribution function as

$$P_c = \frac{4\pi}{3} \int_0^\infty f(r, p) w p^3 dp. \quad (1.20)$$

In the presence of energetic particles, the solar wind equations need to be modified to include the cosmic-ray pressure gradients. Because cosmic rays have negligible mass density, the continuity equation is unchanged. The momentum and energy equations can be found in Section 2.2 (Eqs. 2.3 and 2.4) and will not be repeated here. From these equations we see that the energy exchange rate between the wind and the particles is

$$\frac{\partial F_{c,i}}{\partial x_i} = -\frac{\partial F_{g,i}}{\partial x_i} = u_i \frac{\partial P_c}{\partial x_i} \quad (1.21)$$

where F_c and F_g are the energy fluxes of the two fluids. In the solar wind the cosmic ray gradients are usually positive which means that the wind does work on the particles.

Because cosmic rays are able to diffuse upstream of the shock they create an extended pressure gradient in this region. The 1-D plane shock structure, as shown in *Drury and Völk (1981)*, consists of a smooth region of deceleration, also called a precursor and the gas subshock, where the entropy of the flow changes discontinuously. The extent of the precursor is set by the CR diffusive length scale κ/u . The subshock compression ratio is still determined by the plasma only, because cosmic-ray density and energy fluxes are continuous (unless there is a source of particles at the shock).

A notable results of the CR-shock theories was the existence of smooth transitions without the subshock, that occur when the CR pressure downstream exceeds the thermal pressure. Also the total compression ratio across the transition can be larger than the gas-dynamic limit of 4.0 for strong shocks if the particles are relativistic ($\gamma_c=4/3$) because the gas+CR fluid is more compressible due to its softer equation of state (1.19).

However, unphysical solutions also exist, such as finite downstream CR pressure without any incident CRs for strong shocks which is actually due to unbounded pressure at high energies, where $f \sim p^{-4}$.

We would like to note here that cosmic-ray modified shocks in general have been the subject of numerous investigations (see, e.g., *Falle and Giddings, 1987; Jones and Kang, 1990; Zank et al., 1993; Duffy et al., 1994*). The subject is extremely broad and will not be discussed in full because the primary focus of this work is heliospheric applications. A review of some of the models can be found in *Fichtner (1996)*. Additionally, cosmic rays may conceivably have important heliospheric effects away from the shocks, as proposed in *Jokipii and Morfill (1993)*, and tested in *Florinski and Jokipii (1997)*, who showed that energetic particles of solar origin could help accelerate the solar wind.

Lee and Axford (1988) and Ko and co-workers (*Ko and Webb, 1987, 1988; Ko et al., 1988*), studied the modification of the spherical SWTS by analytic and numerical means. *Lee and Axford (1988)* used a cold plasma ($P_g=0$) approach with cosmic rays providing all the confining pressure. Of course, only smooth transitions are possible (unless $\kappa=0$), which does not apply to the HTS because a smooth shock would produce no ACRs. On the other hand, *Ko and Webb (1988)* employed a perturbation approach ($P_{c,\infty} \ll P_{g,\infty}$) by solving the test-particle cosmic ray transport equation and using the resulting P_c to perturb the solar wind equations. One of the major results of that paper is that the shock is pushed closer to the Sun if P_c at the shock is less than $P_{c,\infty}$, which is true for galactic cosmic rays. This effect is actually caused by a combination of two processes. First, the wind upstream of the shock is decelerated by the CR pressure gradient in the precursor,

making its upstream dynamic pressure, $\rho_1 u_1^2$, smaller. Second, the nearly incompressible flow downstream of the shock tends to conserve $P_g + P_c$, from momentum conservation (*Donohue and Zank, 1993*, this is strictly true for a planar shock):

$$u^2 + P_g + P_c \simeq \text{const.} \quad (1.22)$$

Because the first term is quite small in the postshock region, this equation implies that the gas pressure at the shock will be larger in the presence of the cosmic rays (since P_c increases with distance), pushing the shock inward. The opposite is true for the ACRs which take the thermal energy away from the wind in the downstream region, which overcomes the deceleration upstream thus moving the shock away from the Sun. This effect is discussed in some detail in *Lee (1997)*. There is, however, a fundamental problem with his solution for anomalous P_c , which Lee finds to be proportional to ρ in downstream region: it would be impossible to satisfy the requirement that P_c is 0 at infinity, as expected from the propagation theory, because ρ is, essentially, a constant. However, the picture is correct if the ACRs have a local maximum at the shock and indeed in this case we would expect the shock radius to increase.

With the advent of numerical models beginning in the early 90s, a more realistic treatment of the CR-modified heliosphere became possible. An interesting early 2-dimensional model was presented by *Fahr et al. (1992)* as an attempt to simulate the asymmetric production of ACRs at the shock due to the shock being closer to the Sun in the direction of the interstellar wind. The shock itself was not included in the simulation and the authors only investigated the deceleration of the wind in the supersonic (upstream) region. About 10% radial slowdown of the wind was found, with no effect in

the ϑ direction.

Donohue and Zank (1993) studied the modified shock solutions found by *Drury and Völk* (1981) with a 1-D plane geometry model including ACR seed particle injection from the thermal plasma, based on the injection term of *Zank et al.* (1993). They both obtained the steady-state shock structure, featuring an increase in gas pressure due to a decrease of the CR pressure downstream (see Eq. 1.22), as well as studied interaction between colliding shocks and instabilities associated with CR pressure gradients (see also *Drury and Falle* (1986) for a discussion of this so-called "squeezing" instability).

In a series of two papers, *Chalov and Fahr* (1994, 1996) presented a parametric study of the shock modification by anomalous cosmic rays. Two different injection models were used with injection efficiency as a parameter. In their first model particles are injected directly from the solar wind assuming they gain a certain energy T_{inj} in the process, so that the source term in (1.18) becomes (see also *Falle and Giddings*, 1987)

$$Q_{inj} = \eta T_{inj} \frac{\rho u}{m_p} \delta(x - x_{sh}), \quad (1.23)$$

where x_{sh} is the shock location (in plane geometry) and η is the injection efficiency. Their second model featured pickup ions put in by hand, i.e., not produced by charge exchange with the neutrals. The injection term was derived from an analytic form of the PUI distribution function

$$Q_{inj} = -\alpha P_{pui} \frac{\partial u}{\partial x}, \quad (1.24)$$

where P_{pui} is the pickup ion pressure and α is a constant of the order of 1. Injection rate (1.24) is similar to that derived by *Zank et al.* (1993) by integrating the transport

equation (1.1) between T_{inj} and ∞ . However the derivation in *Chalov and Fahr* (1996) from the known PUI distribution function is questionable because the authors violate the condition of constant wind velocity, used when deriving the distribution function.

A rather complete, spherically symmetric model of the termination shock was developed in *Banaszkiewicz and Ziemkiewicz* (1997). Both galactic and anomalous cosmic rays were present and the PUIs were produced by charge exchange with neutrals and incorporated into the wind. Because of the latter, however, injection was taken to be proportional to the total wind+PUI energy flux across the shock, similar to (1.23). For some of their simulations, very large ACR effects were computed, with the shock moving away from the Sun by as much as 40 AU. However, their results are not directly comparable to those presented in this work because they specify only GCR $P_{c,\infty}$ at large distances allowing $P_{g,\infty}$ to be different in each run. The ACR diffusion coefficient was also apparently taken too large downstream.

The next important step towards a complete self-consistent heliospheric model was made in a series of papers by le Roux and co-workers. All papers on the subject discussed so far used a hydrodynamic approach to the cosmic rays. The fundamental problem with this approach is that the momentum dependence of the diffusion coefficient is omitted (contained in the "average" $\bar{\kappa}$, which must be taken as a free parameter). Additionally, the effective adiabatic constant γ_c must also be specified (5/3 for ACRs and 4/3 for GCRs), which makes it difficult to include both species. Finally, particle spectra are not available, which often makes it impossible to compare model results with the observations.

In the first two papers, *le Roux and Ptuskin* (1995a, 1995b) used a complete kinetic transport equation for the cosmic rays (1.1) in a spherically-symmetric model of the heliosphere including the dynamic effects of the magnetic field. In these models the shock was placed at large heliocentric distances (~ 200 AU), which is probably too far according to modern estimates of 80–120 AU based on radio emissions (*Whang et al.*, 1995) and ACR data (*Stone and Cummings*, 1996). In both of their models, the confining pressure was provided by the cosmic rays only while the subshock structure was mediated by the magnetic field, which was strongly enhanced due to a large amount of wind deceleration upstream. While it appears that this picture does not describe the real heliosphere, it is useful from a theoretical standpoint because it describes possible CR effects that were never discussed before.

This model was later extended by *le Roux and Fichtner* (1997) to include pickup ions and a continuous ACR production at the shock which was proportional to the production rate of the PUIs. Significant deceleration was found for high injection efficiencies and the subshock compression ratio was reduced to 3.4–1.6. Outward movement of the shock by about 3 AU was computed, while the GCRs were found to have only a minor effect. We would like to note here that the authors used the transport equation (1.1) to accelerate freshly injected PUIs at $T \sim 1$ keV, corresponding to a particle speed $w \sim u$. Whether the diffusion theory is applicable at these energies was discussed in the previous section and the criteria are also derived in Section 3.3. It appears that diffusive shock acceleration cannot be used unless $w \gg u$. The outer boundary condition for the ACRs ($\partial f_{ACR} / \partial r = 0$) is also inconsistent with their GCR boundary conditions (i.e., $f_{GCR} = f_{\infty}$). As shown in Section

3.3, $f_{ACR}=0$ is a better condition for the anomalous cosmic rays at the outer boundary.

Very recently, global heliospheric models that included dynamical CR effects began to appear. A global heliospheric model includes all relevant shocks and discontinuities (the termination shock, heliopause and, possibly, the bow shock) and is the most complete method to study the large-scale structure of the heliosphere. Until recently, only neutral hydrogen and PUIs were considered. Neutral hydrogen is usually included as either a second fluid (*Pauls et al.*, 1995; *Pauls and Zank*, 1996) or kinetically via the Boltzmann equation (*Baranov and Malama*, 1993). A review of global heliospheric models can be found in *Zank* (1998). Because our models do not extend beyond the heliopause, the only relevant effect that the PUI have is to decelerate the wind upstream of the termination shock in a linear fashion (as demonstrated by *Lee*, 1997). This effect is not due to a pressure gradient, as is the case for the cosmic rays, but rather to loss of momentum by the solar wind and mass loading by the hot pickup ions.

At least two global 2-dimensional heliospheric models are available today. *Myasnikov et al.* (2000a, 2000b) studied GCRs only and included kinetic neutral atoms. Influence of the galactic cosmic rays on the location of all three surfaces for a realistic $P_{GCR,\infty}=0.18\text{eV/cm}^3$ were mostly overshadowed by the much stronger effects caused by interaction with interstellar neutrals. However, galactic cosmic rays were found to be strongly reaccelerated in the vicinity of the heliopause and the bow shock, while their acceleration at the termination shock was suppressed due to weakening of the shock and curvature effects. The major problem with this analysis is that the diffusion coefficient was taken constant and unrealistically small ($<10^{22}\text{cm}^2/\text{s}$), especially in the interstellar wind. It is more likely that the GCR diffusion coefficient is many orders of magnitude

larger which would suppress the acceleration completely.

The second global heliospheric model was developed by *Fahr et al.* (2000) and includes all relevant particle species: solar wind, pickup ions, neutrals and galactic and anomalous cosmic rays. The ACR injection model was from *Chalov and Fahr* (1996) and pickup ions were treated as a second thermal fluid, distinct from the solar wind, but only inside the heliopause (outside PUIs have a very different distribution function because they charge-exchange in the interstellar medium). Anomalous and galactic cosmic rays were treated separately with different γ_c and $\bar{\kappa}$ and $P_{GCR,\infty}$ was 0.28 eV/cm³. Results for the cosmic-ray distributions were qualitatively similar to *Myasnikov et al.* (2000b), Again, large changes in the GCR pressures between the SWTS and the heliopause were found for unrealistically small κ . Both models use a fluid description for the cosmic rays.

The models developed by the author in this work are somewhat similar in spirit to those developed by *le Roux and Fichtner* (1997). Together with that paper these models remain the only in existence to use a kinetic description for the cosmic rays. Major improvements include:

- a) Our models are 2-dimensional. This means particle drifts can be consistently included which are quite important for GCR transport (*Jokipii and Kopriva, 1979*).
- b) A more realistic wind model is used to study ACR-wind with the solar wind dynamic pressure dependent on heliographic latitude.
- c) Including the magnetic field allows us to actually compute the diffusion coefficients. Most of the previous research in this area use prescribed or even constant diffusion.

d) A different injection model for the ACRs (described in Section 3.3) avoids the difficulty with the applicability of diffusion theory to particle acceleration at low energies.

While not a global heliospheric model (Section 2.1), the much more detailed cosmic-ray description used allows us to gain valuable insights into the multidimensional effects of the cosmic rays in the regions of the heliosphere inside the heliopause.

CHAPTER 2

GALACTIC COSMIC RAYS IN A 2-DIMENSIONAL MODEL

2.1 Introduction

This chapter studies the 2-dimensional effects of the galactic cosmic rays on the solar wind. These high-energy particles are thought to be produced in supernova remnants throughout the Galaxy by the first order (shock) acceleration mechanism (see, e.g., *Biermann, 1995*). Due to expansion of the acceleration region and interaction with interstellar matter during their propagation in the Galaxy, GCRs attain spectra J (see Section 1.1) with a power law of -2.6 (steeper than the ideal production spectrum with a slope of -2.0 , see Eq. 1.11) at relativistic energies. The model described in this chapter studies the propagation of these particles inside the heliosphere and their effects on the solar wind. The interstellar GCR spectrum serves as a boundary condition at the "modulation boundary", a surface outside of which there is little or no modulation.

The basic geometry of the model, approximating the actual heliosphere, is illustrated in Fig. 2.1. This is essentially a 2-dimensional cross-section through the polar axis and the direction of the interstellar wind (the "nose" of the heliosphere). The complete description of the heliosphere requires a 3-dimensional treatment, a formidable task, if cosmic rays are to be included. Because of the large size of the simulation domain and the fact that fine resolution is often required at discontinuities, the problem is

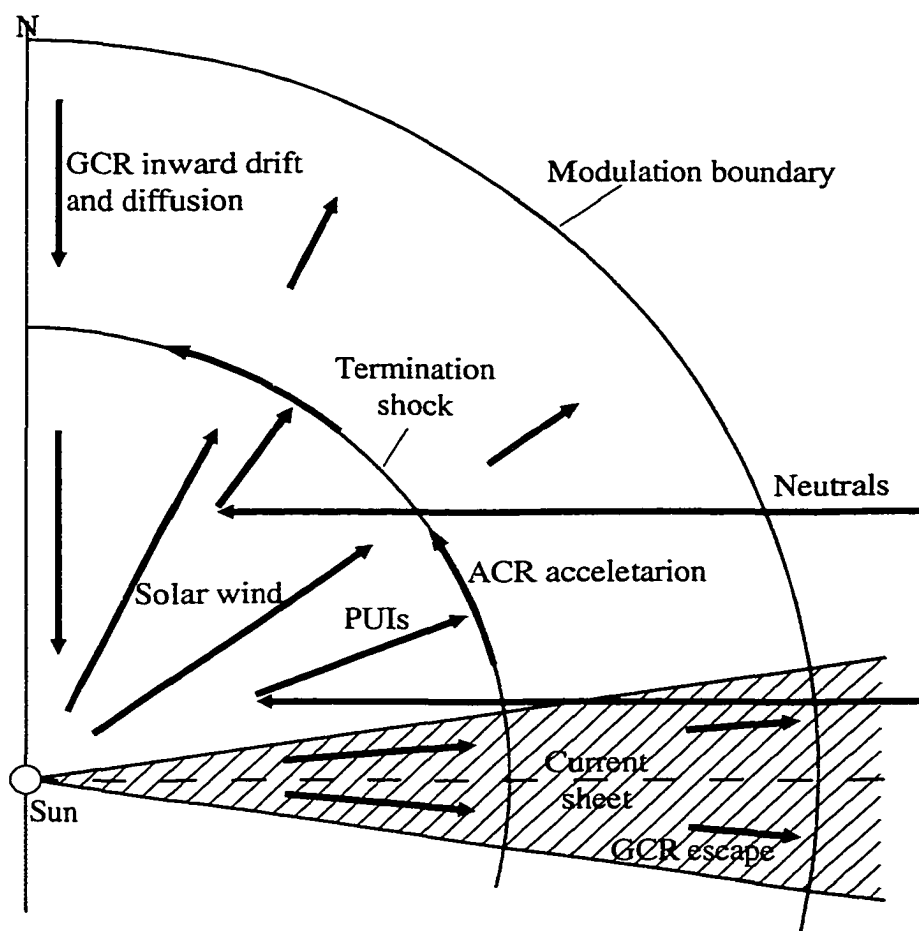


Figure 2.1 A schematic view of the heliosphere used by the self-consistent model. Green lines show the boundary surfaces and discontinuities, light blue arrows show the direction of the solar wind flow, red arrows are drift velocity vectors (notice singular drift at the termination shock), green arrows show the direction of the flow of the interstellar neutrals and dark blue arrows show the flow of the pickup ions. The termination shock lies between 80 and 100AU. The picture corresponds to the region between the Sun and the HP, in the direction of the "nose" of the heliopause (see Fig. I.1). The contact surface is not included in the model due to an axial symmetry about the solar polar axis, rather than the direction of the interstellar flow (an approach adopted by global heliospheric models). This picture illustrates the $A > 0$ solar cycle, the direction of drift is reversed for $A < 0$.

exceptionally computationally-intensive. Examples of 3-dimensional models, which do not, however, include cosmic rays, are *Pauls and Zank (1996)*, *Linde et al. (1998)*, and *McNutt et al. (1999)*. A recent review can be found in *Zank (1999)*.

Limited to two dimensions, global heliospheric CR models available today (see Section 1.3) include a volume outside the heliopause filled with the interstellar medium, allowing the self-consistent computation of the flow of plasma and the neutral component around and into the heliosphere as well as the structure of the three major discontinuities (the termination shock, the heliopause, and the bow shock), resulting from the interaction of the solar wind with the interstellar medium. The drawback of such models is the relatively crude description of the region inside the TS, where most of the cosmic-ray modulation occurs. It is difficult to include the polar-equatorial asymmetry in the diffusion coefficients as well as in the drift velocities and, in fact, the two global heliospheric models described in the previous section both ignore the drift completely and assume a spatially uniform diffusion (a poor approximation, considering κ varies by at least an order of magnitude with radial distance and latitude, possibly much more).

The approach taken in this work differs radically from that described above. We do not explicitly include the interstellar medium, instead the "modulation boundary" is also the outflow boundary for the solar wind (approximating the heliopause, to some extent, considering u is already very small at large distances). The interstellar medium is specified through the confining pressure as well as the flow of neutral hydrogen. This is described in more detail in Sections 2.2 and 3.2. The current model provides a much more detailed description for the particle transport, including drifts (shown with red arrows in Fig. 2.1) and spatially-varying diffusion, computed from the magnetic field

distribution, rather than specified by hand. Note that the green and dark blue arrows in Fig. 2.1 show the flow of the neutral atoms and pickup ions, respectively. These two species of particles will be considered in Chapter 3, but are ignored here.

This chapter has the following structure. Section 2.2 sets up the fluid equations and the boundary conditions for the solar wind plasma. Magnetic field equations, including the new approach to the modified polar field, are discussed in Section 2.3. Section 2.4 describes the CR transport equation and the transport coefficients used. Sections 2.5 and 2.6 describe numerical methods used to solve the fluid and the cosmic-ray equations, respectively. Results from the model showing changes in the solar wind flow produced by the GCR pressure gradients in two dimensions are discussed in Section 2.7. Section 2.8 focuses on the differences in GCR distribution for the test-particle case vs. the self-consistent case. Finally, some discussion and conclusions are given in Section 2.9.

2.2 Solar wind model

In this section we use the standard hydrodynamic solar wind model with an addition of the cosmic-ray pressure terms. The solar wind plasma is considered to be a polytropic gas with mass density ρ , bulk velocity u , and thermal pressure P_g . In this one-fluid model, electrons are considered massless (therefore they carry no mass or bulk momentum), but have a temperature T equal to that of protons (Parker, 1965). The total gas pressure is therefore

$$P_g = 2 n k T. \quad (2.1)$$

Equations of continuity, momentum and energy conservation for a fluid can be written as follows:

$$\frac{\partial \rho}{\partial t} + \nabla \cdot (\rho \mathbf{u}) = 0, \quad (2.2)$$

$$\frac{\partial(\rho \mathbf{u})}{\partial t} + \nabla \cdot (\rho \mathbf{u} \mathbf{u}) + \nabla P_g = -\nabla P_c, \quad (2.3)$$

$$\frac{\partial}{\partial t} \left(\frac{\rho \mathbf{u}^2}{2} + \frac{P_g}{\gamma-1} \right) + \nabla \cdot \left[\mathbf{u} \left(\frac{\rho \mathbf{u}^2}{2} + \frac{\gamma P_g}{\gamma-1} \right) \right] = -\mathbf{u} \cdot \nabla P_c, \quad (2.4)$$

where $\gamma=5/3$ is the polytropic index. The cosmic ray terms on the right hand side will be explained in Section 2.4. We are ignoring magnetic forces here, see Section 2.3 for a discussion of why this can be done.

Another form of the second moment equation that contains only P_g and \mathbf{u} , can be obtained by subtracting (2.2), multiplied by $\mathbf{u}^2/2$, and (2.3), scalar-multiplied by \mathbf{u} , from (2.4). Then it can easily be shown that

$$\frac{\partial P_g}{\partial t} + \mathbf{u} \cdot \nabla P_g + \gamma P_g \nabla \cdot \mathbf{u} = 0 \quad (2.5)$$

By substituting $\nabla \cdot \mathbf{u}$ from (2.2) it then follows that

$$\frac{\partial P_g}{\partial t} - \gamma \frac{P_g}{\rho} \frac{\partial \rho}{\partial t} + \mathbf{u} \cdot \left(\nabla P_g - \gamma \frac{P_g}{\rho} \nabla \rho \right) = 0 \quad (2.6)$$

Eq. (2.6) describes the conservation of the convective derivative of P_g/ρ^γ , showing the entropy of the gas is a constant of motion (see *Landau and Lifshitz*, 1988, p. 448). It is, however, invalid at discontinuities, where entropy can undergo arbitrarily large jumps. Eq. (2.4) can be used at shocks because it describes the conservation of the energy flux.

Because we are interested primarily in shocks, we will not use the polytropic law but rather the actual energy conservation equation (2.4).

We now rewrite Eqs. (2.2) through (2.4) in the spherical coordinate system ($r-\vartheta$).

Note that in this coordinate system $\mathbf{u}=(u,v)$.

$$\frac{\partial \rho}{\partial t} + \frac{1}{r^2} \frac{\partial(\rho u r^2)}{\partial r} + \frac{1}{r \sin \vartheta} \frac{\partial(\rho v \sin \vartheta)}{\partial \vartheta} = 0, \quad (2.7)$$

$$\frac{\partial(\rho u)}{\partial t} + \frac{1}{r^2} \frac{\partial(\rho u^2 r^2)}{\partial r} + \frac{1}{r \sin \vartheta} \frac{\partial(\rho u v \sin \vartheta)}{\partial r} + \frac{\partial P_g}{\partial r} = -\frac{\partial P_c}{\partial r}, \quad (2.8)$$

$$\frac{\partial(\rho v)}{\partial t} + \frac{1}{r^2} \frac{\partial(\rho u v r^2)}{\partial r} + \frac{1}{r \sin \vartheta} \frac{\partial(\rho v^2 \sin \vartheta)}{\partial r} + \frac{1}{r} \frac{\partial P_g}{\partial \vartheta} = -\frac{1}{r} \frac{\partial P_c}{\partial \vartheta}, \quad (2.9)$$

$$\begin{aligned} & \frac{\partial}{\partial t} \left(\frac{\rho(u^2+v^2)}{2} + \frac{P_g}{\gamma-1} \right) + \frac{1}{r^2} \frac{\partial}{\partial r} \left[u r^2 \left(\frac{\rho(u^2+v^2)}{2} + \frac{\gamma P_g}{\gamma-1} \right) \right] \\ & + \frac{1}{r \sin \vartheta} \frac{\partial}{\partial \vartheta} \left[v \sin \vartheta \left(\frac{\rho(u^2+v^2)}{2} + \frac{\gamma P_g}{\gamma-1} \right) \right] = -u \frac{\partial P_c}{\partial r} - \frac{v}{r} \frac{\partial P_c}{\partial \vartheta}. \end{aligned} \quad (2.10)$$

The system of equations (2.7)–(2.10) needs to be solved numerically. The standard technique for systems with shocks is to use wave-propagation algorithms, such as Godunov-type (*Godunov et al.*, 1961). The method itself will be described in Section 2.5. The rest of this section will discuss initial and boundary conditions for the solar wind.

For the model described in this chapter, we assume the solar wind is uniform in latitude. The reason behind this choice is that we would like to isolate cosmic-ray related latitudinal effects from those caused by the asymmetry of the solar wind flow (but see Chapter 3 for a latitude-dependent solar wind model). The wind speed was taken to be

$u_0=400\text{km/s}$, in the radial direction. Its density was taken to be 4.6cm^{-3} and temperature 10^5K at the orbit of Earth. All four parameters (ρ , u , v and P_g) must be specified at the inner boundary, because all three types of waves (left and right sound and entropy) propagate into the domain from the boundary in the supersonic flow (*Landau and Lifshitz*, 1988, p.549). Note that the second velocity component (v) is only a passive variable at the inner boundary. Because we expect the shock to form somewhere within the domain, the wind will become subsonic at some point and will remain subsonic on the outflow (far) boundary. Only one type of wave (a sound wave moving in the $-r$ direction) can propagate into the domain and, hence, one BC must be specified. We chose to set the pressure ($P_{g,\infty}$) because it dominates the subsonic postshock flow and sets the location of the termination shock. For this model, we took $P_{g,\infty}=1.1\text{eV/cm}^3$.

The initial conditions are quite simple. When there is no ϑ dependence, the supersonic wind has a constant velocity and density falling off as r^{-2} . The subsonic postshock flow is nearly incompressible, hence both P_g and ρ are $\sim\text{const}$, while $u\sim r^{-2}$. At a strong shock the jump condition is

$$P_{g2} \simeq \frac{2\rho_1 u_1^2}{\gamma+1}, \quad (2.11)$$

where index 1 refers to pre-shock values and 2 to post-shock values. The shock will be located at

$$\frac{r_{sh}}{r_0} = C \left(\frac{\rho_0 u^2}{P_{g,\infty}} \right)^{1/2}, \quad (2.12)$$

where r_0 is 1AU and C is determined from the downstream conditions. For

incompressible flow ($P_{g2}=P_{g\infty}$), $C=[2/(\gamma+1)]^{1/2}\simeq 0.87$, while for a general polytropic flow the expression is slightly more complicated and $C\simeq 0.94$ (*Parker, 1963*). It is, in fact, not necessary to put a shock in the initial condition as it will appear by itself and eventually reach the steady state (2.12).

2.3 Magnetic field equations

To complete the system of equations for our problem, we need to write the Faraday's law for the three magnetic field (MF) components in a spherical coordinate system. Throughout this paper we neglect the dynamical effects of the MF on the solar wind, i.e., omit the magnetic pressure terms from the momentum and energy equations. This approach is justified because the model only extends a few tens of AU beyond the termination shock and does not include the build-up of the field near the heliopause due to slowing down of the wind approaching the stagnation point (*Nerney et al., 1991, 1993*). As shown in the first of these papers, the MF (or, rather, its dominating ϕ -component), will be proportional to the radial distance if the wind is approximately incompressible (downstream of the shock), since $uB_\phi r \sim \text{const}$ (see Eq. 2.16 below) and $u \sim r^{-2}$. When the field becomes large enough, the MF pressure gradient starts to accelerate the wind to a constant speed. This causes B_ϕ to stop increasing and eventually become $B_\phi \sim r^{-1}$ at a heliocentric distance of several r_{sh} (this is called the Cranfill effect).

In order for the magnetic field to be unimportant dynamically, its pressure $P_m = B^2/8\pi$ must be smaller than the larger of the wind dynamic pressure $P_u = \rho u^2/2$ and its thermal

pressure, P_{gas} . Taking 1AU equatorial values of $n=10\text{cm}^{-3}$, $u=450\text{km/s}$ and $B=3\times 10^{-5}$ Gs, we find that in the supersonic wind $P_m/P_u \sim 2\times 10^{-3}$. At the termination shock the magnetic field has a jump of about 4 and therefore beyond the shock $P_m/P_{gas} \sim 0.03r/r_{sh}$, which is still small until many shock radii. Our assumption that the MF is dynamically unimportant for our problem is therefore correct and the Cranfill effect will not be in evidence at these distances.

The magnetic field equation for an ideal plasma without dissipation can be written as

$$\frac{\partial \mathbf{B}}{\partial t} - \nabla \times (\mathbf{u} \times \mathbf{B}) = 0. \quad (2.13)$$

Converting this equation into spherical coordinates ($r-\theta$) gives

$$\frac{\partial B_r}{\partial t} - \frac{1}{r \sin \vartheta} \frac{\partial}{\partial \vartheta} \left[\sin \vartheta (u B_\vartheta - v B_r) \right] = 0, \quad (2.14)$$

$$\frac{\partial B_\vartheta}{\partial t} + \frac{1}{r} \frac{\partial}{\partial r} \left[r (u B_\vartheta - v B_r) \right] = 0, \quad (2.15)$$

$$\frac{\partial B_\phi}{\partial t} + \frac{1}{r} \frac{\partial (r u B_\phi)}{\partial r} + \frac{1}{r} \frac{\partial (v B_\phi)}{\partial \vartheta} = 0. \quad (2.16)$$

Unlike Eq. (2.16), Eqs. (2.14) and (2.15) are not transport equations for the individual MF components but rather provide a relationship between B_r and B_ϑ . Because we are interested in a steady state configuration, we can use the steady-state limit in (2.14) and (2.15) to obtain

$$u B_\vartheta = v B_r. \quad (2.17)$$

Note that Eq. (2.17) is not valid at the neutral sheet, where both v and B_ϑ vanish. To supplement (2.17) we need Maxwell's equation for the magnetic field, $\nabla \cdot \mathbf{B} = 0$:

$$\frac{1}{r^2} \frac{\partial(r^2 B_r)}{\partial r} + \frac{1}{r \sin \vartheta} \frac{\partial(\sin \vartheta B_\vartheta)}{\partial \vartheta} = 0. \quad (2.18)$$

This equation can be treated as a transport equation for B_r with B_ϑ obtained from (2.17). It is in fact solved in the code by a finite volume method similar to the solar wind equations (see Section 2.5).

It remains to describe the polar magnetic field model we use in our simulations. As suggested by *Jokipii and Kota* (1989), the solar magnetic field contains a long-wavelength fluctuating component in the transverse direction. Supergranulation on the surface of the Sun is thought to be the source of the fluctuations. Because the transverse field falls off with distance as r^{-1} instead of r^{-2} for the radial field, we expect the mean square magnetic field to be significantly larger in the polar regions. As noted in *Jokipii and Kota* (1989) this leads to inhibited access of the particles to the inner solar system over the poles due to the reduction in drift velocity, according to Eq. (1.3), as well as radial diffusion (see Eq. 2.30 below).

In general, fluctuations affect the perpendicular diffusion coefficient according to the quasi-linear theory (*Jokipii*, 1971), where the perpendicular diffusion coefficient, κ_\perp , is proportional to the power at zero wavenumber, i.e., the mean square displacement of the field line due to random walk. However, because we are not using QLT results for the perpendicular diffusion (see the next section), we concentrate instead on deriving the equation for the magnitude of the fluctuations in the quasi-static limit.

Let us assume for simplicity that the field lines undergo random walk in the ϑ direction. Similar to Eq. (2.15), we can write the equation for $B_\vartheta = B_{\vartheta 0} + B_{\vartheta m} g(r, t)$, where

B_{g_0} is the standard Archimedian spiral field and g is some random function (actually, a map of the transverse velocity of supergranulation $u_g(t)$) with B_{g_m} being the slowly varying amplitude of the fluctuating component (it need not be small compared with B_{g_0}):

$$\frac{\partial(B_{g_0}+B_{g_m}g(r,t))}{\partial t} + \frac{1}{r} \frac{\partial}{\partial r} [ru(B_{g_0}+B_{g_m}g(r,t))-rvB_r] = 0. \quad (2.19)$$

We now multiply this equation by $g(r,t)$ and average over a distance Δr and time Δt , large compared to the wavelength and period of the fluctuations, but small compared to the distance and timescales of the model, such that $\langle g \rangle_{r,t} = 0$. Taking a period of 1 day, typical for supergranulation, and a solar wind velocity of 750 km/s, we obtain $\Delta r > 6 \times 10^{12} \text{cm} \sim 0.4 \text{AU}$, which is smaller than the relevant distance scales in the problem. We now obtain

$$\begin{aligned} \langle g \rangle_{r,t} \frac{\partial B_{g_0}}{\partial t} + \left\langle g \frac{\partial(B_{g_m}g)}{\partial t} \right\rangle_{r,t} + \frac{1}{r} \langle g \rangle_{r,t} \frac{\partial(ruB_{g_0})}{\partial r} + \frac{1}{r} \left\langle g \frac{\partial(ruB_{g_m}g)}{\partial r} \right\rangle_{r,t} \\ - \frac{1}{r} \langle g \rangle_{r,t} \frac{\partial(rvB_r)}{\partial r} = 0. \end{aligned} \quad (2.20)$$

It can be shown that for any random function $g(r,t)$ $\langle g \partial g / \partial t \rangle_{r,t} = \langle g \partial g / \partial r \rangle_{r,t} = 0$. Indeed,

$$\left\langle \frac{1}{\Delta r} \int_r^{r+\Delta r} g \frac{\partial g}{\partial r} dr \right\rangle_t = \frac{1}{2\Delta r} [\langle g^2(r,t) \rangle_t - \langle g^2(r+\Delta r,t) \rangle_t] = 0. \quad (2.21)$$

Eq. (2.20) yields then

$$\frac{\partial B_{g_m}}{\partial t} + \frac{1}{r} \frac{\partial(ruB_{g_m})}{\partial r} = 0 \quad (2.22)$$

Equation (2.22) is valid at the shock in the sense that it gives appropriate jump

conditions $[\mathbf{u}B_{\theta,m}] = 0$ or $[B_{\theta,m}] = [\rho]$ for a spherical shock.

The system of equations (2.16), (2.17), (2.18) and (2.22) are the desired transport equations for the magnetic field. Notice that the wind velocity \mathbf{u} should be considered a known variable because it can be determined independently from the solar wind equations, which do not include MHD effects. Fixed boundary conditions are specified at the inner boundary, and reflective BC are set at $\theta = 0, \pi/2$.

2.4 Cosmic-ray model

Equation (1.1) is the cornerstone of any cosmic-ray propagation model. Cosmic-ray energy and pressure are defined as second moments of the distribution function,

$$E_c = 4\pi \int f T p^2 dp, \quad (2.23)$$

with P_c given by (1.20). Equation (1.1) can be multiplied by T and integrated over momentum space, to obtain the energy conservation equation for the cosmic rays,

$$\frac{\partial E_c}{\partial t} + \nabla \cdot [\mathbf{u}(E_c + P_c) - \bar{\kappa} \cdot \nabla E_c] = \mathbf{u} \cdot \nabla P_c. \quad (2.24)$$

Here the κ term refers to the average over the momentum diffusion tensor. The second term is the conserved cosmic-ray energy flux. The last term describes the transfer of energy to the solar wind and is the same as in (2.4). Eq. (2.24) is often used instead of (1.1) because it has one less degree of freedom. In this work, however, we are solving the complete 2-dimensional transport equation including the momentum variable. This equation can be written in the spherical coordinate system as follows:

$$\begin{aligned}
& \frac{\partial f}{\partial t} + (u + v_{d,r} + v_{k,r}) \frac{\partial f}{\partial r} + (v + v_{d,\vartheta} + v_{k,\vartheta}) \frac{1}{r} \frac{\partial f}{\partial \vartheta} - \frac{1}{r^2} \frac{\partial}{\partial r} \left(\kappa_{rr} r^2 \frac{\partial f}{\partial r} \right) \\
& - \frac{1}{r^2 \sin \vartheta} \frac{\partial}{\partial \vartheta} \left(\kappa_{\vartheta\vartheta} \sin \vartheta \frac{\partial f}{\partial \vartheta} \right) - 2 \kappa_{r\vartheta} \frac{\partial f}{r \partial r \partial \vartheta} \\
& = \frac{1}{3} \left[\frac{1}{r^2} \frac{\partial (r^2 u)}{\partial r} + \frac{1}{r \sin \vartheta} \frac{\partial (\sin \vartheta v)}{\partial \vartheta} \right] \frac{\partial f}{\partial \ln p},
\end{aligned} \tag{2.25}$$

where v_k is the additional term due to cross-diffusion. Its components are:

$$v_{k,r} = -\frac{1}{\sin \vartheta} \frac{\partial (\kappa_{r\vartheta} \sin \vartheta)}{r \partial \vartheta}, \tag{2.26}$$

$$v_{k,\vartheta} = -\frac{1}{r} \frac{\partial (\kappa_{r\vartheta} r)}{\partial r}. \tag{2.27}$$

An important quantity is the differential streaming flux S , or number of particles crossing a unit area in a given energy interval. It can be written as

$$S = -\frac{4\pi p^2}{w} \left(\kappa^T \cdot \nabla f + \frac{\mathbf{u}}{3} p \frac{\partial f}{\partial p} \right), \tag{2.28}$$

where w is the particle's velocity, and κ^T is the total diffusion coefficient, including the antisymmetric terms (drifts). The diffusion tensor can be found from (1.2) and the drift velocities can be written as:

$$v_{d,r} = \frac{pcw}{3e} \frac{1}{r \sin \vartheta} \frac{\partial}{\partial \vartheta} \left(\sin \vartheta \frac{B_\phi}{B^2} \right), \tag{2.29}$$

$$v_{d,\vartheta} = -\frac{pcw}{3e} \frac{1}{r} \frac{\partial}{\partial r} \left(r \frac{B_\phi}{B^2} \right). \tag{2.30}$$

The radial drift velocity can become extremely large near the poles. Substituting the Parker spiral magnetic field into (2.29), we can see (*Jokipii and Kopriva, 1979*) that

$$v_{d,r} = -\frac{pcw}{3e} \frac{2r^2 \Omega_0 u^3}{B_0 r_0^2 (u^2 + r^2 \Omega_0^2 \sin^2 \vartheta)^2 \cos \vartheta}, \quad (2.31)$$

where $\Omega_0 = 2.7 \times 10^{-6} \text{s}^{-1}$ is the angular velocity of the solar rotation. When $\sin \vartheta \rightarrow 0$ the drift velocity can become very large, possibly exceeding the speed of light for GeV particles. This is not in fact unphysical because the drift velocity needs to be averaged over a particle's gyroradius (*Isenberg and Jokipii, 1979*), which itself increases with energy in the same fashion as the drift velocity. However, because of our use of a modified polar magnetic field, described in Section 2.3, polar drift velocity will depend on r^{-1} rather than r^{-2} , reducing substantially the drift at large radii.

We have adopted the often used form for the diffusion coefficient (e.g., *Kota and Jokipii, 1993, le Roux and Ptuskin, 1995*)

$$\kappa_{\parallel} = \kappa_0 \frac{w}{c} \left(\frac{P}{P_0} \right)^{1/2} \frac{B_0}{|B|}, \quad (2.32)$$

where $P = pc/e$ is the particle's rigidity. The physical meaning of this dependence is that the parallel mean free path scales as the gyroradius with distance (or magnetic field). The momentum dependence however, is purely empirical. Values for κ_0 found in the literature vary in the range between 10^{21} and $10^{23} \text{cm}^2/\text{s}$, depending on which CR data the authors are trying to fit (if any). In this simulation, we took $\kappa_0 = 1.5 \times 10^{22} \text{cm}^2/\text{s}$.

Perpendicular diffusion is a separate topic and has been a focus of many investigations into particle transport phenomena. Perpendicular transport models are dependent on the form of the magnetic field fluctuations in the direction perpendicular to the mean field. The two distinct turbulence types are slab and 2-dimensional. In slab turbulence, δB_{\perp} is

axisymmetric about the mean field, while in 2-D turbulence δB_{\perp} varies in the directions perpendicular to \mathbf{B} .

Two well-established diffusion models that are in use today are the hard-sphere scattering (Axford, 1965) and the quasi-linear theory (QLT, Jokipii and Parker, 1969). In the hard-sphere model the perpendicular diffusion coefficient can be written as

$$\kappa_{\perp} = \frac{w r_c}{3} \frac{\omega_c \tau}{1 + \omega_c^2 \tau^2}, \quad (2.33)$$

where τ is a "relaxation time" or time over which particle orbits decorrelate, which in some cases is equal to the time between scatterings. The QLT, on the other hand, uses a slab turbulence model to show that perpendicular diffusion is caused by random walk of the field lines (expressed by the power spectrum of the fluctuations at zero wavenumber, see Jokipii, 1971), rather than scattering. It then gives a result similar to (2.33) with

$$\omega_c \tau \sim \frac{r_c}{l_c} \frac{B^2}{\delta B_{\perp}^2} \quad (2.34)$$

(Forman *et al.*, 1974), where l_c is the correlation length of the slab turbulence, corresponding roughly to a knee in the turbulence spectra signifying a transition between the energy and the Kolmogorov intervals. The precise numerical dependence is determined by the actual slab turbulence spectrum $P_{\perp}(k)$.

While the QLT is physically sound, it is restricted to axisymmetric turbulence. It is in fact rarely used in actual cosmic-ray simulations. The reason is that it gives perpendicular diffusion that is too small to explain the observed particle phenomena (see Zank *et al.*, 1998 and le Roux *et al.*, 1999 for a discussion on why QLT doesn't work very well for GCR and ACR modulation). Instead, empirical or semi-empirical

expressions are used for κ_{\perp} (e.g., *Potgieter and Moraal, 1985; Webber et al., 1990*). In this work, we assume

$$\kappa_{\perp} = \eta \kappa_{\parallel}, \quad (2.35)$$

a dependence commonly used in the literature (see e.g., *Kota and Jokipii, 1993* and *le Roux and Fichtner, 1997*). The free parameter η is a constant and was taken to be 0.05.

We should mention that the perpendicular diffusion described by (2.35) recently received theoretical support from hybrid simulations (*Giacalone, 1998, Giacalone and Jokipii, 1999*). Using combined slab–2D turbulence models, these authors obtained a constant ratio of κ_{\perp} to κ_{\parallel} over a wide range of particle energies. *Le Roux et al (1999)* point out that for mostly 2–D turbulence

$$\kappa_{\perp} \sim \frac{\delta B_{\perp}^2}{B^2} \kappa_{\parallel}. \quad (2.36)$$

Note that Eq. (2.36) can be formally obtained by setting κ_{\perp} equal to zero in (1.2) and computing a diffusion coefficient perpendicular to the mean magnetic field $\kappa_{\parallel} \sin^2 \vartheta$, where ϑ is the angle between a field line at any point and the mean field. Perpendicular diffusion in this case is caused by diffusion along the diverging field lines (note however that the proportionality constant in (2.36) was $\ll 1$ in *Giacalone and Jokipii, 1999*).

At the far boundary, the interstellar cosmic–ray spectrum needs to be specified. We use the following spectral shape at infinity

$$f_{\infty} = f_0 \frac{(p^2 c^2 + m^2 c^4)^{-1.8}}{p}. \quad (2.37)$$

This gives the observed $T^{-2.6}$ dependence of the galactic CR population at energies where

modulation is weak (*Meyer, 1969*), while the spectrum turns over at low energies. The normalization constant was chosen such as to give a GCR pressure $P_{c,\infty}=0.4\text{eV/cm}^3$. We use an absorbing BC $f=0$ at the inner boundary (but see Chapter 3 for a different choice of the lower boundary condition).

The heliospheric neutral sheet presents an additional difficulty for modulation models that include drifts. As can be seen from Eq. (2.29), $v_{d,r}$ has a singularity there because B_ϕ changes sign across the neutral sheet. There are at least two ways to deal with this situation. The first, mentioned in Section 1.2 was suggested by *Jokipii and Kopriva (1979)*. They derive the $\vartheta=\pi/2$ conditions by integrating the transport equation (1.4) across the boundary between $\pi/2-\epsilon$ and $\pi/2+\epsilon$ with $\epsilon\rightarrow 0$. In this case, ϑ diffusion balances the singular radial drift within the sheet. This condition can also be obtained by setting the ϑ component of the CR streaming flux (2.28) to zero:

$$\frac{\kappa_{\vartheta\vartheta}}{r} \frac{\partial f}{\partial \vartheta} - \frac{pcw}{3e} \frac{B_\phi}{B^2} \frac{\partial f}{\partial r} = 0. \quad (2.38)$$

This equation provides a relation between the known radial gradient and the unknown ϑ gradient at the boundary.

The second method of including the singular drift was put forward by *Potgieter and Moraal (1985)*. They use a smooth transition of the radial drift velocity across the neutral sheet by modifying κ_A . Instead of B_ϕ/B^2 in (2.29) they used $f(t)B_\phi/B^2$, where

$$f = \frac{1}{\alpha} \tan^{-1} \left[\left(1 - \frac{2\vartheta}{\pi} \right) \tan \alpha \right] \quad (2.39)$$

and

$$\alpha = \cos^{-1} \left(\frac{\pi}{2\vartheta_{1/2}} - 1 \right). \quad (2.40)$$

Here, $\vartheta_{1/2}$ is the angle where $f=1/2$. Equations (2.39) and (2.40) are actually an attempt to incorporate a finite width current sheet into a 2-D model and *Burger and Potgieter* (1989) provide a relation between $\vartheta_{1/2}$ and the current sheet tilt angle. However, because we are interested in solar minimum conditions, we take $\vartheta_{1/2}$ close to $\pi/2$ to simulate a flat neutral sheet. This approach is slightly more convenient computationally because there is no need for a complicated boundary condition ($\partial f/\partial \vartheta=0$ can be used instead) which could cause stability problems for dimensionally-split numerical schemes.

2.5 Numerical method for the wind

In this section we will discuss in detail numerical algorithms used to solve the solar wind equations (2.2)–(2.4) or (2.7)–(2.10). This system of partial differential equations is of hyperbolic type, which means its solution is a superposition of propagating waves. For problems like this, ordinary finite difference techniques tend to produce inferior results when applied to fluid flows that admit shocks (*LeVeque*, 1998). Finite difference approximations to derivatives only apply in smooth flows. At discontinuities these methods produce oscillations resulting in unstable solutions, or in smeared-out shocks, when large numerical diffusion is used.

Instead, finite volume or Godunov type methods are used for this type of problem. Such methods operate on sets of differential equations written as conservation laws.

Indeed, Eqs. (2.2)–(2.4) represent conservation of number of particles, their momentum, and total energy. These equations can now be written in a form more convenient for numerical solution as follows:

$$\frac{\partial \mathbf{q}}{\partial t} + \nabla_r \cdot \mathbf{F} + \nabla_\vartheta \cdot \mathbf{G} = \mathbf{S}, \quad (2.41)$$

where \mathbf{q} , \mathbf{F} , \mathbf{G} and \mathbf{S} are the solution, flux and source vectors respectively. We actually use a slightly different format of (2.41), where the spacial variables r and ϑ are treated as Cartesian coordinates, i.e., derivatives are taken over dr and $rd\vartheta$. We have found that this method provides more accurate solutions near latitudinal boundaries. The solution vector can then be written as

$$\mathbf{q} = \begin{pmatrix} D \\ U \\ V \\ E \end{pmatrix} = \begin{pmatrix} \rho r^2 \\ \rho u r^2 \\ \rho v r^2 \\ r^2 [\rho(u^2 + v^2)/2 + P_g / (\gamma - 1)] \end{pmatrix}, \quad (2.42)$$

the fluxes can be written as

$$\mathbf{F} = \begin{pmatrix} U \\ U^2/D + P_g r^2 \\ UV/D \\ U/D(E + P_g r^2) \end{pmatrix}, \quad \mathbf{G} = \begin{pmatrix} V \\ UV/D \\ V^2/D + P_g r^2 \\ V/D(E + P_g r^2) \end{pmatrix}, \quad (2.43)$$

and the sources are

$$\mathbf{S} = \begin{pmatrix} -V/r \cot \vartheta \\ 2P_g r - UV/D \cot \vartheta / r - r^2 \partial P_c / \partial r \\ -V^2/D \cot \vartheta / r - r \partial P_c / \partial \vartheta \\ -V/D(E + P_g r^2) \cot \vartheta / r - U/D r^2 \partial P_c / \partial r - V/D r \partial P_c / \partial \vartheta \end{pmatrix}, \quad (2.44)$$

where P_s is a function of \mathbf{q} , i.e.,

$$P_s = \frac{(\gamma-1)}{r^2} \left(E - \frac{U^2 + V^2}{2D} \right). \quad (2.45)$$

Notice that the S term contains both geometric and 'real' sources.

Let us introduce an evenly spaced grid $r_i = r_0 + i\Delta r$, $\vartheta_j = \vartheta_0 + j\Delta\vartheta$ and time intervals $t\Delta t$.

Eq. (2.41) can be integrated over a volume of a cell and Δt , to obtain

$$\begin{aligned} \mathbf{q}_{i+1/2,j+1/2}^{t+1} = & \mathbf{q}_{i+1/2,j+1/2}^t - \frac{\Delta t}{\Delta r} (\mathbf{F}_{i+1,j+1/2}^{t+1/2} - \mathbf{F}_{i,j+1/2}^{t+1/2}) \\ & - \frac{\Delta t}{r_{i+1/2}\Delta\vartheta} (\mathbf{G}_{i+1/2,j+1}^{t+1/2} - \mathbf{G}_{i+1/2,j}^{t+1/2}) + \frac{\Delta t}{2} \mathbf{S}_{i+1/2,j+1/2}^t + \frac{\Delta t}{2} \mathbf{S}_{i+1/2,j+1/2}^{t+1/2}. \end{aligned} \quad (2.46)$$

In Eq. (2.44) we use the so-called Strang splitting (*LeVeque, 1998*) for the source terms where the last term is computed based on values already updated from the r -step. This preserves second-order (in time) accuracy of the scheme.

Finite volume methods differ from each other according to how they compute the fluxes (F or G). The original Godunov method (*Godunov et al., 1961, Holt, 1984, p. 33*) approximates \mathbf{q} inside every cell by a constant (its value at the midpoint). Fluxes are then found by solving a Riemann problem at each cell interface. In a Riemann problem, a discontinuity at an interface evolves into a self-similar solution consisting of 3 waves, each propagating either to the left or to the right. The central wave is a contact discontinuity, propagating with the fluid speed u , while the remaining waves can be either shocks or rarefactions, moving at $u \pm c_s$, where c_s refers to the sound speed in some intermediate states that must be computed (*Landau and Lifshitz, 1988, p. 519*). *Godunov et al.* (1961) calculate these states by finding the intersection point of the adiabats

(Poisson for rarefaction waves, Hugoniot for the shocks) and connecting them to known left and right states. An iteration method is required because the resulting equations have no analytic solution.

There are two reasons why the original Godunov method is not very good for heliospheric modeling. First, it is only first order accurate. Second, the iterative Riemann solver could fail in front of a strong shock, because the adiabats can intersect very close to $P_g=0$ in the (u, P_g) plane, producing negative pressure in the intermediate state (*van Leer, 1979*). Our tests confirmed that the original Godunov's method is unstable under these circumstances.

Several second-order finite volume methods exist (*van Leer, 1979; Colella and Woodward, 1984*). In this work, we use a somewhat simplified version of the method developed in *Colella (1990)*. The simplification is that we do not use \mathcal{G} -corrections when calculating r -fluxes and vice versa, i.e., we use simple dimensional splitting. Because of this, we will describe the method in one dimension only. The piece of the code that computes fluxes is called twice for r and \mathcal{G} passes. Without the source terms, which have already been included in Eq. (2.46), the transport equation (2.41) can be written in matrix form:

$$\frac{\partial \mathbf{q}}{\partial t} + \mathbf{A} \frac{\partial \mathbf{q}}{\partial r} = 0, \quad (2.47)$$

where $\mathbf{A} = \partial \mathbf{F} / \partial \mathbf{q}$ is the following matrix:

$$A = \begin{pmatrix} 0 & 1 & 0 & 0 \\ \frac{(\gamma-3)U^2 + (\gamma-1)V^2}{2D^2} & (3-\gamma)\frac{U}{D} & (1-\gamma)\frac{V}{D} & \gamma-1 \\ -\frac{UV}{D^2} & \frac{V}{D} & \frac{U}{D} & 0 \\ \frac{U}{D^2} \left(\frac{(\gamma-1)(U^2+V^2)}{D} - \gamma E \right) & (1-\gamma)\frac{3U^2}{2D^2} & (1-\gamma)\frac{UV}{D^2} & \gamma\frac{U}{D} \end{pmatrix}. \quad (2.48)$$

This matrix has 4 real eigenvalues and 4 linearly independent eigenvectors. Any vector, such as q can therefore be expanded as a linear combination of eigenvectors, a property that will be used in the predictor step below.

The method used in this work consists of 6 steps:

- 1) Convert "conserved" variables q into primitive variables $p = (\rho, u, v, P_g)$ according to (2.42). This, according to *Colella* (1990), both simplifies the scheme and produces steeper discontinuities.
- 2) Compute the slopes Δp . A limiter on the slopes is necessary to suppress their calculation at discontinuities. Indeed, a slope calculation is useful in smooth flows to achieve second-order accuracy, but will generate oscillations at shocks. A limiter serves the purpose of reducing the slope at the shock to its value in the nearest adjacent cell. If a cell is a local maximum or minimum, the slope should be set to zero. The popular minmod limiter, for example, calculates the slopes according to

$$\Delta p_i = \begin{cases} p_{i+1} - p_i, & \text{if } |p_{i+1} - p_i| < |p_i - p_{i-1}|, \quad (p_{i+1} - p_i)(p_i - p_{i-1}) > 0 \\ p_i - p_{i-1}, & \text{if } |p_{i+1} - p_i| > |p_i - p_{i-1}|, \quad (p_{i+1} - p_i)(p_i - p_{i-1}) > 0 \\ 0, & \text{if } (p_{i+1} - p_i)(p_i - p_{i-1}) < 0 \end{cases}. \quad (2.49)$$

The limiter used here is a slightly modified version of the minmod limiter that we found provides a more accurate solution for the solar wind density at small radii (i.e., the r^{-2} law), even when the resolution is not good in that region.

- 3) A predictor step and, most complicated. The task is to compute left and right states at each interface, $\mathbf{p}_{i,L}$ and $\mathbf{p}_{i,R}$ at time $t+1/2$ in order to plug them into the Riemann solver later. We can write (2.47) as

$$\mathbf{p}_{i,L}^{t+1/2} = \mathbf{p}_{i-1/2} + \left(\frac{1}{2} - \frac{\Delta t}{2 \Delta r} T_{i-1/2}^{-1} A_{i-1/2} T_{j-1/2} \right) \Delta \mathbf{p}_{i-1/2} \quad (2.50)$$

$$\mathbf{p}_{i,R}^{t+1/2} = \mathbf{p}_{i+1/2} - \left(\frac{1}{2} + \frac{\Delta t}{2 \Delta r} T_{i+1/2}^{-1} A_{i+1/2} T_{i+1/2} \right) \Delta \mathbf{p}_{i+1/2}, \quad (2.51)$$

where $T = \partial \mathbf{q} / \partial \mathbf{p}$ is the transformation matrix between primitive and conserved variables. The eigenvalues of $T^{-1} A T$ are simply, $\lambda^1 = u - c_s$, $\lambda^2 = \lambda^3 = u$, $\lambda^4 = u + c_s$, the characteristic speeds in the i th cell. Its left and right eigenvectors, \mathbf{l}^ν , and \mathbf{r}^ν , respectively, satisfy $\mathbf{l}^\nu T^{-1} A T = \lambda^\nu \mathbf{l}^\nu$ and $T^{-1} A T \mathbf{r}^\nu = \lambda^\nu \mathbf{r}^\nu$. These are given explicitly in *Colella (1990)*. Given that $\Delta \mathbf{p}$ can be expanded in right eigenvectors, we can write

$$\Delta \mathbf{p} = \sum (\mathbf{l}^\nu \cdot \Delta \mathbf{p}) \mathbf{r}^\nu \quad (2.52)$$

$$T^{-1} A T \Delta \mathbf{p} = \sum \lambda^\nu (\mathbf{l}^\nu \cdot \Delta \mathbf{p}) \mathbf{r}^\nu. \quad (2.53)$$

We should note here that the actual scheme only counts those components in (2.52) and (2.53) that propagate towards the appropriate boundary, i.e., those for which $\lambda^\nu > 0$ for the left states and $\lambda^\nu < 0$ for the right states.

- 4) Convert $\mathbf{p}_{i,L}$ and $\mathbf{p}_{i,R}$ back into conserved variables $\mathbf{q}_{i,L}$ and $\mathbf{q}_{i,R}$. Primitive variables are still useful and will be kept because they are needed to compute the wave

speeds (see below). We are now ready to solve the Riemann problem using the left and right states at time $t+1/2$.

- 5) Solve the Riemann problem. As mentioned previously, the iterative method of Godunov doesn't work very well for strong shocks. Several approximate Riemann solvers exist, the most popular being that of Roe (Roe, 1981) that uses a specially constructed constant coefficient matrix A in place of the original non-linear matrix in (2.47). In this work we use the Harten-Lax-van Leer-Einfeldt (HLL) solver (Harten *et al.*, 1983; Einfeldt *et al.*, 1991) because of its superior stability. The solution consists of only three constant states, not four, bound by two waves with speeds approximating the largest and the smallest wave speeds b^\pm (such that $b^+ \geq b^-$) of the exact Riemann problem. These are computed as

$$b^- = u - c_s, \quad b^+ = u + c_s, \quad (2.54)$$

where the average velocity is defined as

$$u = \frac{\sqrt{\rho_L} u_L + \sqrt{\rho_R} u_R}{\sqrt{\rho_L} + \sqrt{\rho_R}}, \quad (2.55)$$

and the average sound speed is computed as

$$c_s^2 = \frac{\sqrt{\rho_L} c_{s,L}^2 + \sqrt{\rho_R} c_{s,R}^2}{\sqrt{\rho_L} + \sqrt{\rho_R}} + \frac{\gamma - 1}{2} \frac{\sqrt{\rho_L \rho_R} (u_R - u_L)^2}{(\sqrt{\rho_L} + \sqrt{\rho_R})^2}. \quad (2.56)$$

The last equation can be better understood if we remember that $c_s^2 = (\gamma - 1)(H - u^2/2)$ (see Roe, 1981), where H is the total enthalpy (per unit mass) defined as

$$H = \frac{u^2}{2} + \frac{P_\varepsilon}{\rho(\gamma-1)} + \frac{P_\varepsilon}{\rho} \quad (2.57)$$

Eq. (2.56) in fact uses the average total enthalpy computed similar to (2.55). Knowing the wave speeds we can now compute the conditions at the cell boundary r_i after a discontinuity breakup. The fluxes are given by

$$F_i^{t+1/2} = \begin{cases} F(q_{i-1/2}), & \text{if } b_i^- > 0 \\ \frac{b_i^+ F(q_{i-1/2}) - b_i^- F(q_{i+1/2}) + b_i^+ b_i^- (q_{i+1/2} - q_{i-1/2})}{b_i^+ - b_i^-}, & \text{if } b_i^- < 0 < b_i^+ \\ F(q_{i+1/2}), & \text{if } b_i^+ < 0 \end{cases} \quad (2.58)$$

To derive the intermediate flux in (2.58), *Harten et al.*, (1983) employ the following approach. First, the conservation law (2.41) (in 1-D) was integrated between $r-\varepsilon$ and $r+\varepsilon$ and over τ , where ε and τ are some small space and time intervals (of course, the CFL stability condition must be met, i.e., $\varepsilon/2 > \tau \max(|b^+|, |b^-|)$). The same conservation law was then integrated between $r-\varepsilon$ and 0 and over τ . Under the assumption that ε and τ are small, left and right states are constant, which after appropriate transformations leads to (2.58).

6) Finally, use just derived fluxes in (2.46) to advance the differencing scheme in the r -direction.

The procedure described above is then performed in the ϑ -direction in exactly the same way, but with $rd\vartheta$ replacing dr and v replacing u . After each half-step source terms are added according to (2.46).

2.6 Numerical method for the CR equation

The cosmic-ray transport equation was written in Section 2.4. Partial differential equations of this type (parabolic) require implicit methods to solve (at least for the diffusion portion), since explicit methods impose very strict constraints on the time step. A two-dimensional case introduces an additional problem, namely, the resulting matrices are block-diagonal, which means they are computationally expensive to solve. An alternative is to use dimensional splitting. In the case of Eq. 2.4, this means treating radial terms implicitly and the ϑ terms explicitly during one half-step, then reversing the order for the second half-step. Additional complications arise when mixed second derivatives and momentum terms are present.

There are two commonly used splitting techniques: Peaceman–Rachford (PR) and Douglas–Rachford (DR) methods (see *Lapidus and Pinder, 1982*). The first method uses symmetric first and second half-steps, while the latter uses only values computed during the first half-step. The second technique is asymmetric in that the second step uses both old and half-step values. The second method is particularly suitable for equations with a mixed derivative (which cannot be easily split into x and y components), as demonstrated in *McKee and Mitchell (1970)*. The version we use is modified slightly to accommodate the momentum terms. The two half-steps can be written as follows:

$$\left(1 - \frac{\Delta t}{2} L_{rr}\right) f^{t+1/2} = \left(1 + \frac{\Delta t}{2} L_{rr} + \Delta t L_{\vartheta\vartheta} + 2\Delta t L_{r\vartheta} + \Delta t L_{pp}\right) f^t, \quad (2.59)$$

$$\left(1 - \frac{\Delta t}{2} L_{\vartheta\vartheta}\right) f^{t+1} = f^{t+1/2} - \frac{\Delta t}{2} L_{\vartheta\vartheta} f^t. \quad (2.60)$$

We use second order space-centered expressions for the differential operators L_{rr} and

L_{99} . Notice that the cross terms and the momentum terms are treated explicitly. The momentum terms use second-order upwind differencing. Therefore,

$$L_{rr} f = \frac{1}{r_i^2 \Delta r^2} \left[r_{i+1/2}^2 \kappa_{i+1/2,j,k}^{rr} (f_{i+1,j,k} - f_{i,j,k}) - r_{i-1/2}^2 \kappa_{i-1/2,j,k}^{rr} (f_{i,j,k} - f_{i-1,j,k}) \right] - \frac{1}{2 \Delta r} v_{i,j,k}^{\text{tot},r} (f_{i+1,j,k} - f_{i-1,j,k}) \quad (2.61)$$

$$L_{99} f = \frac{1}{r_i^2 \sin \vartheta_j \Delta \vartheta^2} \times \left[\sin \vartheta_{j+1/2} \kappa_{i,j+1/2,k}^{99} (f_{i,j+1,k} - f_{i,j,k}) - \sin \vartheta_{j-1/2} \kappa_{i,j-1/2,k}^{99} (f_{i,j,k} - f_{i,j-1,k}) \right] - \frac{1}{2 r \Delta \vartheta} v_{i,j,k}^{\text{tot},9} (f_{i+1,j,k} - f_{i-1,j,k}) \quad (2.62)$$

$$L_{r9} f = \frac{1}{4 t_i \Delta r \Delta \vartheta} \kappa_{ij}^{r9} (f_{i+1,j+1,k} - f_{i+1,j-1,k} - f_{i-1,j+1,k} + f_{i-1,j-1,k}) \quad (2.63)$$

$$L_{pp} = \frac{1}{3 \ln 10 \Delta p} (\nabla \cdot \mathbf{u})_{ij} \times \begin{cases} (1.5 f_{i,j,k} - 2 f_{i,j,k-1} + 0.5 f_{i,j,k-2}), & (\nabla \cdot \mathbf{u})_{ij} < 0 \\ (-0.5 f_{i,j,k+2} + 2 f_{i,j,k+1} - 1.5 f_{i,j,k}), & (\nabla \cdot \mathbf{u})_{ij} > 0 \end{cases}, \quad (2.64)$$

where $v^{\text{tot}} = u + v_d + v_k$. Boundary conditions are always of the first type (constant value) on the grid interfaces except at the physical boundaries of the domain. In the latter case, boundary conditions include reflection (zero gradient) at 0° and 90° latitudes, absorbing or zero differential streaming flux at the lower radial boundary (see Section 3.3) and a fixed galactic cosmic ray spectrum at the upper radial boundary.

The described numerical method has proven to be stable and accurate for a wide range of diffusion and drift values, i.e., for both diffusion- and convection-dominated cases. We were able to reproduce both radial and spectral features of the solution to the one-

dimensional problem of transmission of a monoenergetic initial cosmic-ray distribution at large distances, including particle acceleration at the SWTS, derived by *Webb et al.*, 1985. The code also shows good agreement with earlier 2-dimensional CR simulations (see, e.g., *Jokipii and Davila*, 1981).

2.7 Results: solar wind effects produced by the cosmic rays

We performed a number of simulations to test whether the accuracy of the results depends on grid resolution and boundary conditions. The domain size was chosen to extend from 5AU to 120AU and over 90° in the northern hemisphere (the southern hemisphere is in this case a mirror image due to symmetry about the equatorial plane). We use a uniform grid with a grid size of 1AU by 0.5° . The reason the lower radial boundary was set at 5AU was to avoid problems caused by insufficient resolution in this region (and to avoid computational overhead, since we are only interested in the outer heliosphere). The results presented here were obtained with a "thick" neutral sheet described by (2.39) and (2.40). The angle $\vartheta_{1/2}$ in (2.40) was taken to be 10° . While results obtained with the BC (2.38) were similar, numerical implementation required that the direction of differencing change depending on the sign of A (so that differencing is always upstream). In addition, much higher angular resolution is required at the equatorial boundary, as shown in *Jokipii and Kopriva* (1979), which makes the calculations computationally expensive. In momentum space the simulation spans energies from 10MeV to 20GeV using a logarithmic grid with 90 intervals.

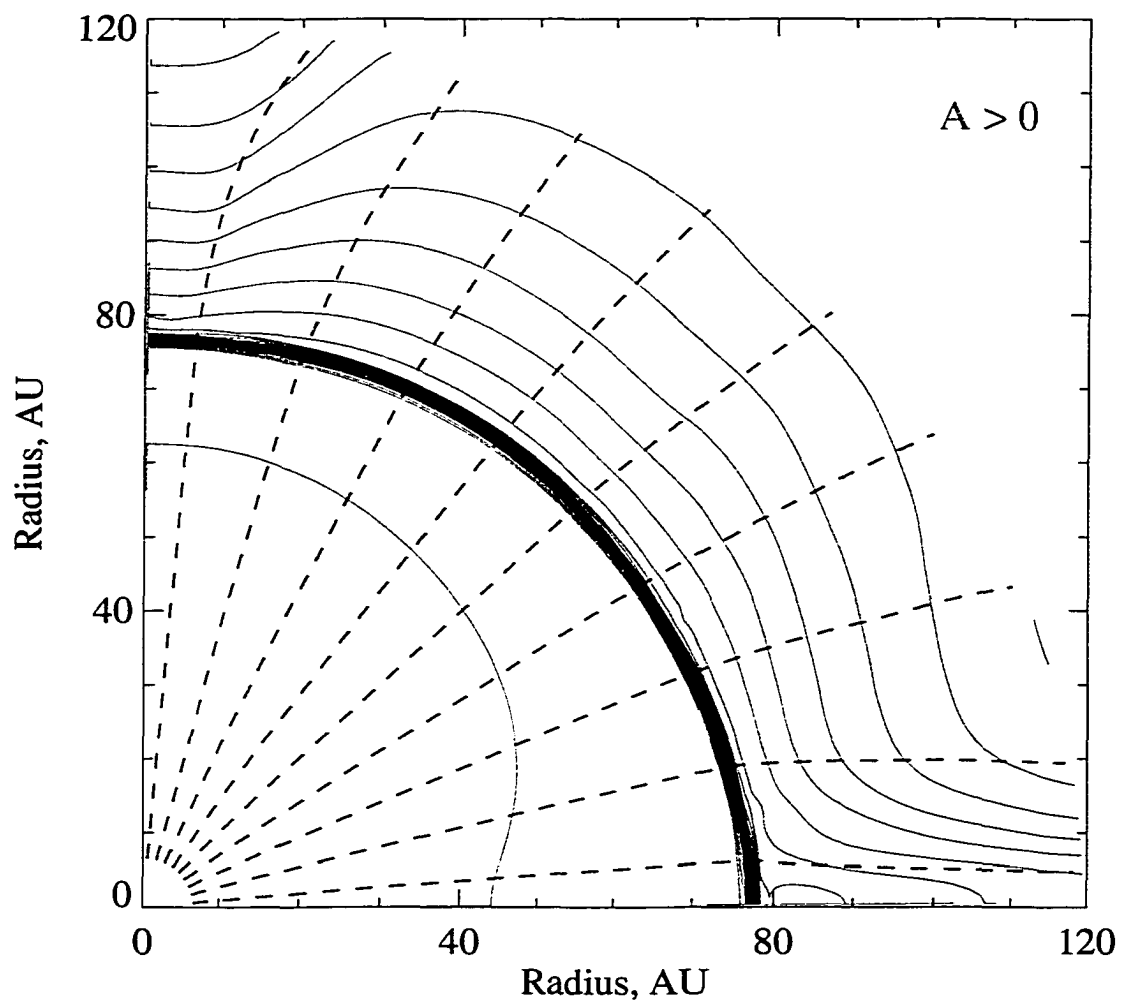


Figure 2.2 Wind velocity and streamlines for the case $A > 0$. The green radial wind velocity contours are evenly spaced between 200km/s and 0. The streamlines (dashed) show the wind is deflected towards the ecliptic downstream of the shock.

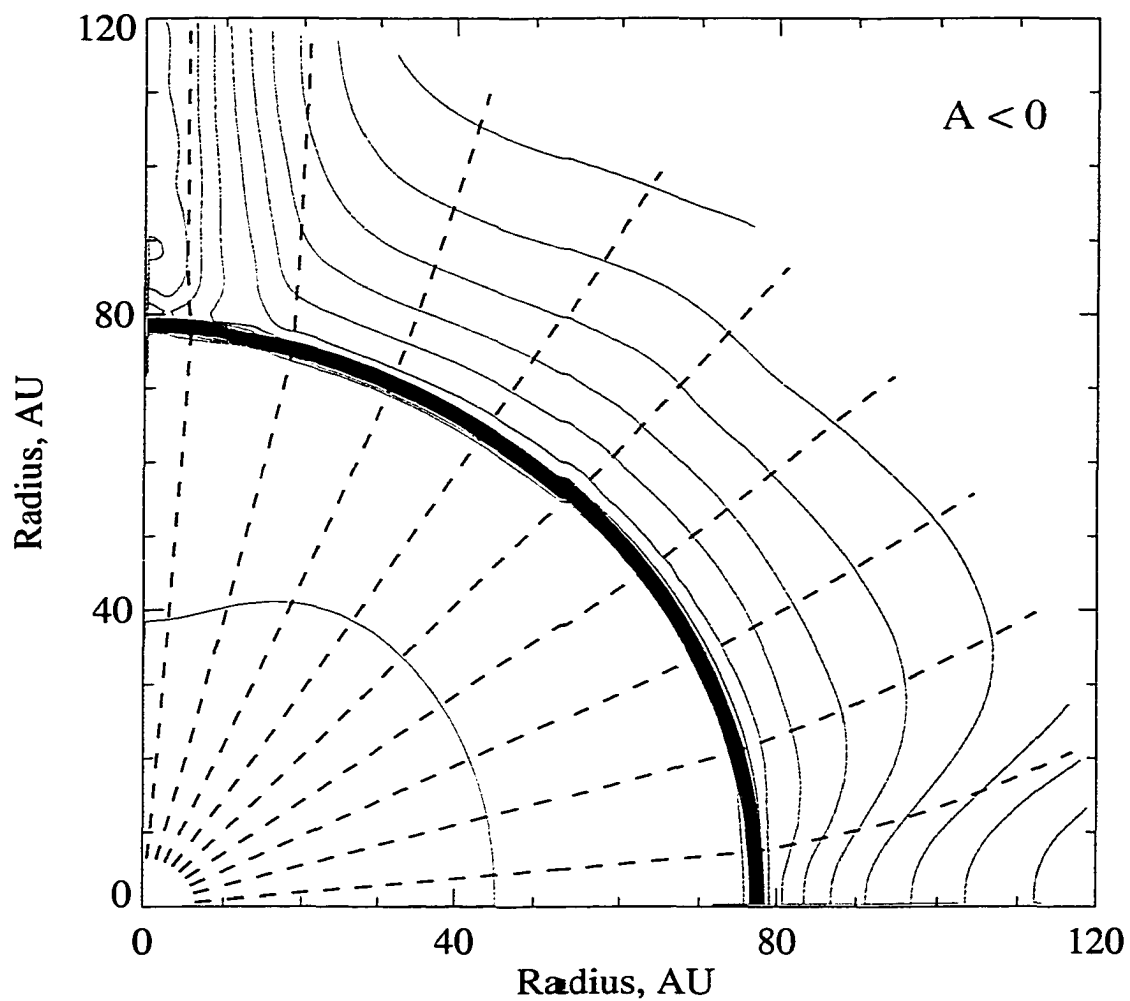


Figure 2.3 Same as Fig. 2.2 but for $A < 0$ case. The wind flow is deflected towards the pole by the GCR pressure gradient.

We should note here that it was impossible to reach a steady-state solution in this simulation. As will be shown below, the slowing down of the solar wind near the outer boundary at certain latitudes may cause an inflow, which is obviously unphysical, since the heliopause would prevent mixing of the solar wind with the interstellar medium. The heliopause would move inward to balance the pressure difference. Because we cannot realistically include the heliopause in the model, the simulation has to stop once an inflow starts to occur. Still, the time to reach such a state is of the order of 10 years which is comparable to the 11-year solar cycle. Because magnetic field reversal would occur during this time, running the simulation any longer would make little sense. The results shown are for a time 8 years from the start of the simulation.

Figures 2.2 and 2.3 show the radial solar wind speed contours for $A > 0$ and $A < 0$, respectively. One can see that there is a significant change in the flow pattern downstream of the shock. In particular, in the first case the wind is deflected towards the ecliptic, where the wind speed is not decreasing as r^{-2} , but remains roughly a constant (see also Fig. 2.4). This is simply a result of mass conservation in a nearly incompressible fluid: as the area of a channel decreases, the flow speed must increase. The wind speed in the polar region is much lower and an inflow will occur here when the radial wind speed drops to zero at the far boundary. The flow at mid-latitudes is essentially unchanged, also as a result of near incompressibility – the entire wind shifts towards the equatorial plane. The picture is reversed for $A < 0$. The termination shock remains essentially spherical with subshock compression ratio very close to the unperturbed value of 4.0, with small (less than 0.2) deviations near the latitudinal boundaries. Fig. 2.4 shows the radial wind speed and the wind and GCR pressures as a

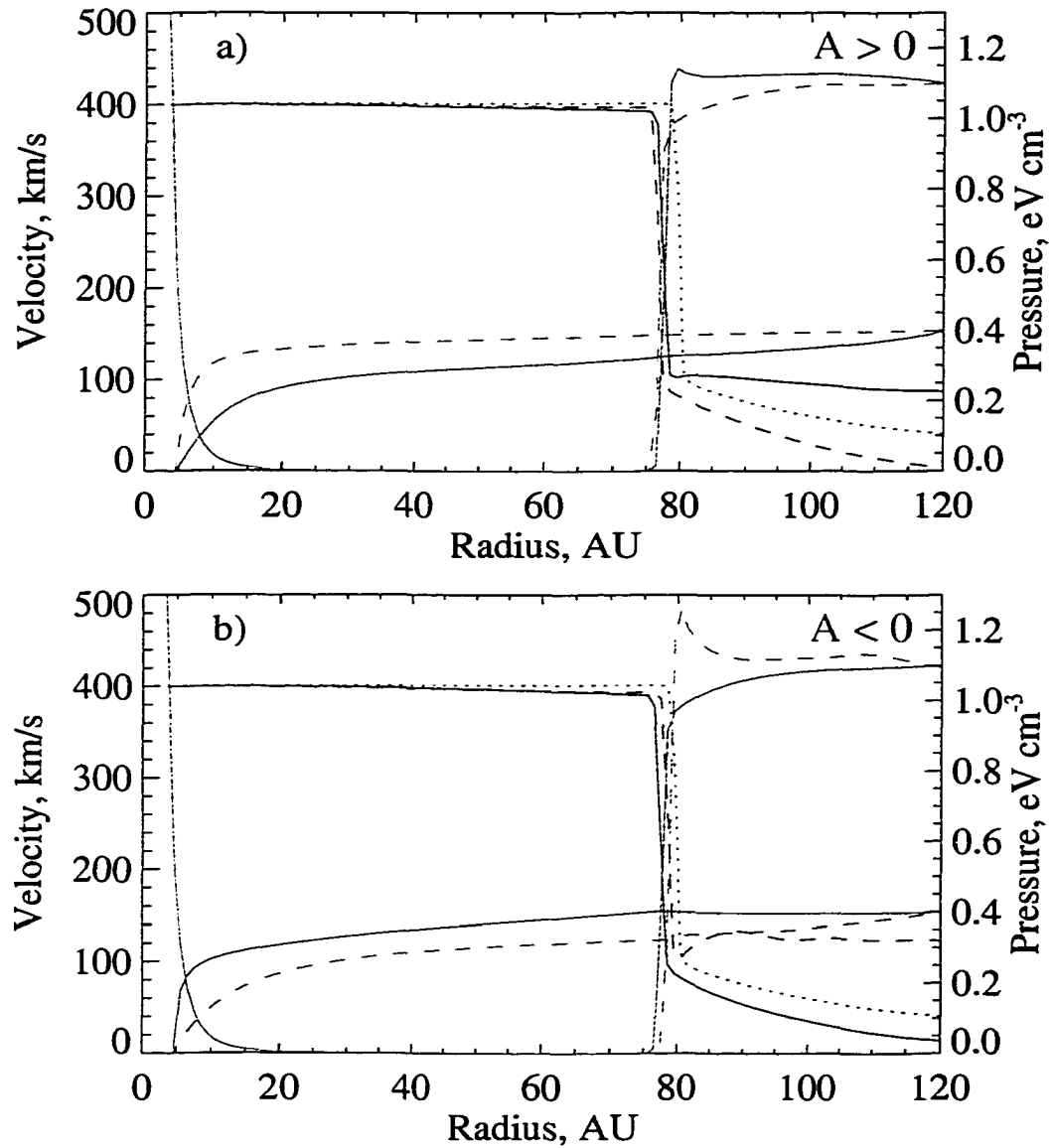


Figure 2.4 Radial profiles of the wind speed (blue), plasma pressure (green) and cosmic-ray pressure (red) for a) $A > 0$ and b) $A < 0$. Solid lines correspond to $\vartheta=90^\circ$ (equator), dashed lines show distributions along the polar axis. Solar wind speed for the case without the CRs is shown with dotted lines.

function of distance near the boundaries. One can see that there is a wide and shallow precursor formed on the upstream side. The shock has moved inward between 3 and 4 AU compared to the case without the cosmic rays, in agreement with the general theory (Lee, 1997). The increase in thermal pressure downstream is caused by a positive GCR pressure gradient (see Eq. 1.22). Another interesting feature of the solutions shown in Fig. 2.4a,b is a pressure peak just downstream of the shock. This seems to be a consequence of large u_s at slightly higher latitude (for $A > 0$). The pressure peak offsets the dynamic pressure $\rho u_s^2/2$. However its magnitude is several times larger (0.08 eV/cm³ vs. 0.013 eV/cm³). It is conceivable that the peaks are artifacts of the solution.

2.8 Results: cosmic ray distribution

Two-dimensional maps of the GCR distribution are shown in Figures 2.5 and 2.6 for $A > 0$, and 2.7 and 2.8 for $A < 0$. The general behavior is similar to that reported by modulation studies (Haasbroek and Potgieter, 1995; Potgieter, 1998). For positive solar cycles, cosmic rays drift in from the poles and towards the equatorial plane in the inner heliosphere, then exit through the neutral sheet, which explains their larger radial gradients in that region. At low energies, modulation is stronger and intensity contours are spaced closer together. Also, drift effects are more important at high energies, because $\kappa \sim p^{1/2} w$ while $v_d \sim p w$, according to Eqs. (2.32) and (2.29). This explains the larger latitudinal gradients in the inner heliosphere in Figures 2.5 and 2.6. The dashed lines in these figures show test-particle contours, e.g., when cosmic ray effects on the

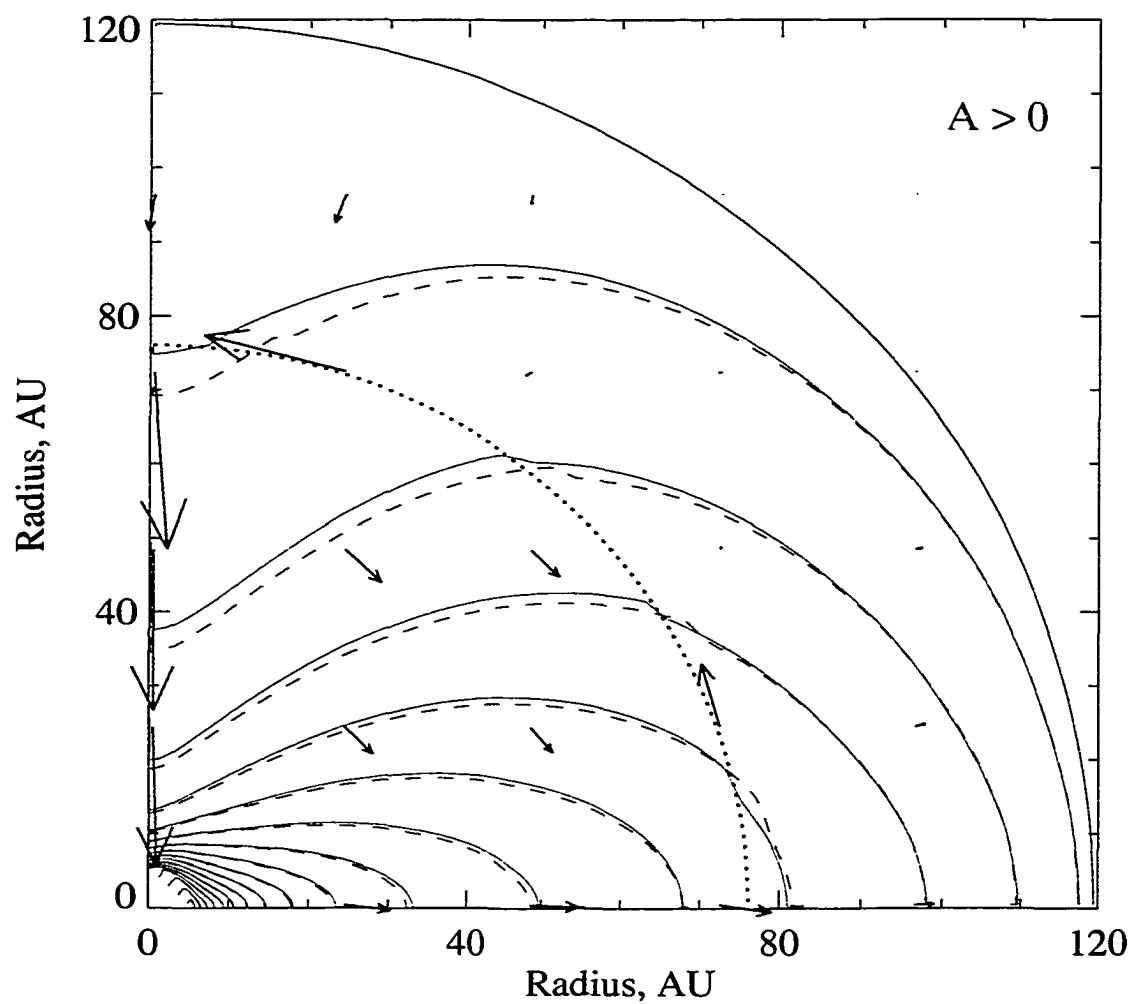


Figure 2.5 Cosmic-ray intensity contours for 1.6 GeV protons (solid lines) for $A > 0$. Test-particle results are shown for comparison with dashed lines. Contours are evenly spaced at 5% increments. Green arrows show drift velocities, the length of an arrow is proportional to $(v_d)^{1/2}$.

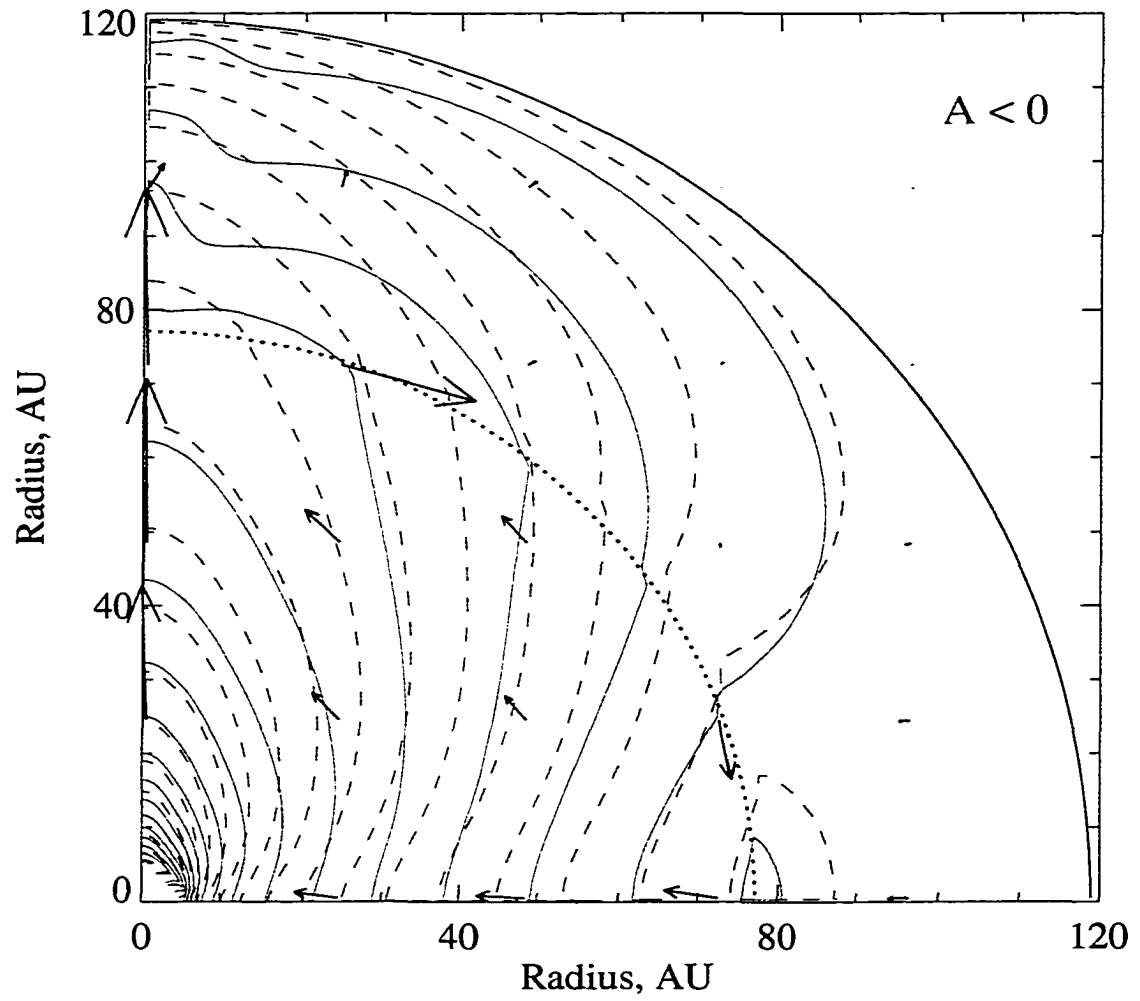


Figure 2.6 Same as in Fig. 2.5, but for $A < 0$. Note that the direction of drifts is reversed.

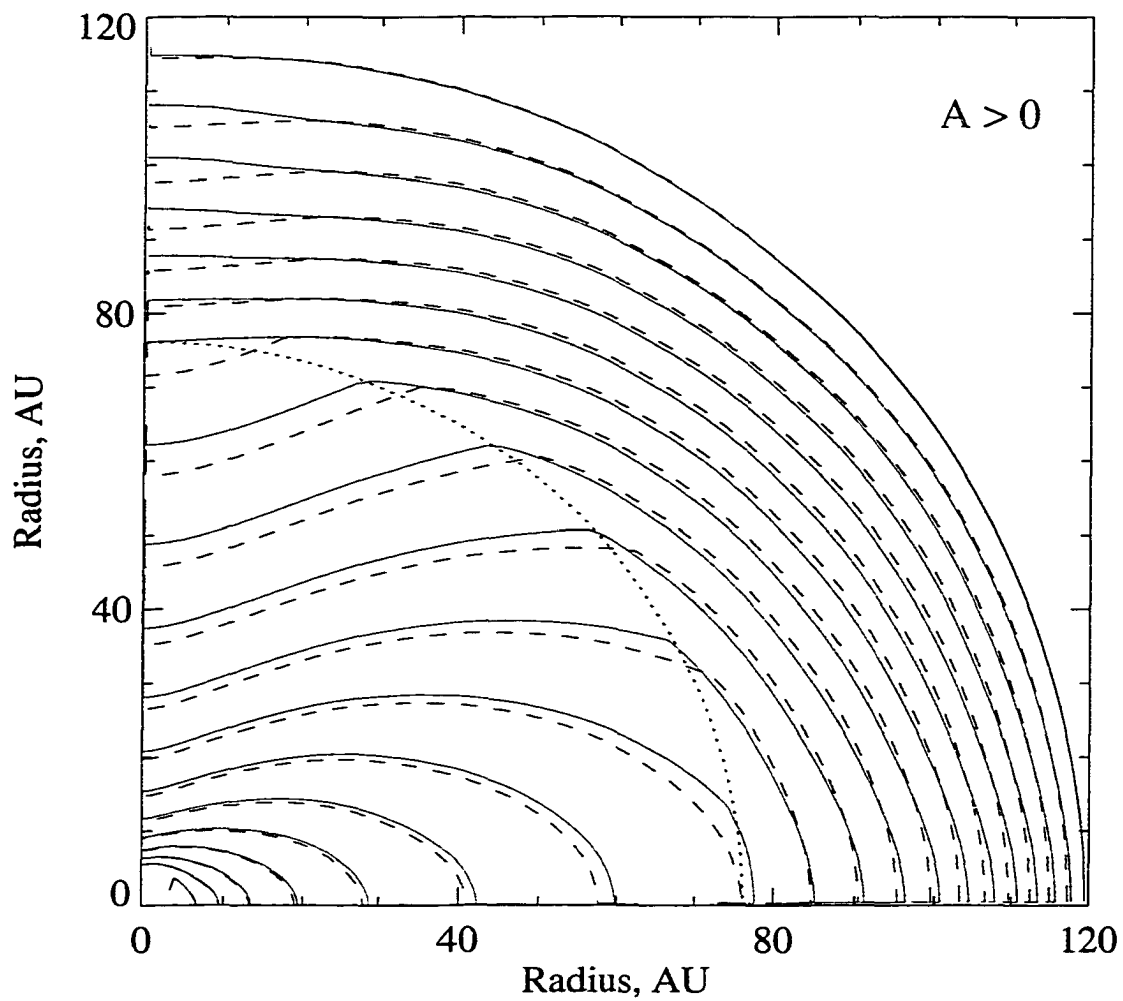


Figure 2.7 Same as in Fig. 2.5 but for 72MeV protons. The contours are more evenly spaced than in Fig. 2.5 because the drift velocities (not shown) are much smaller at low energies and hence latitudinal differences are less pronounced.

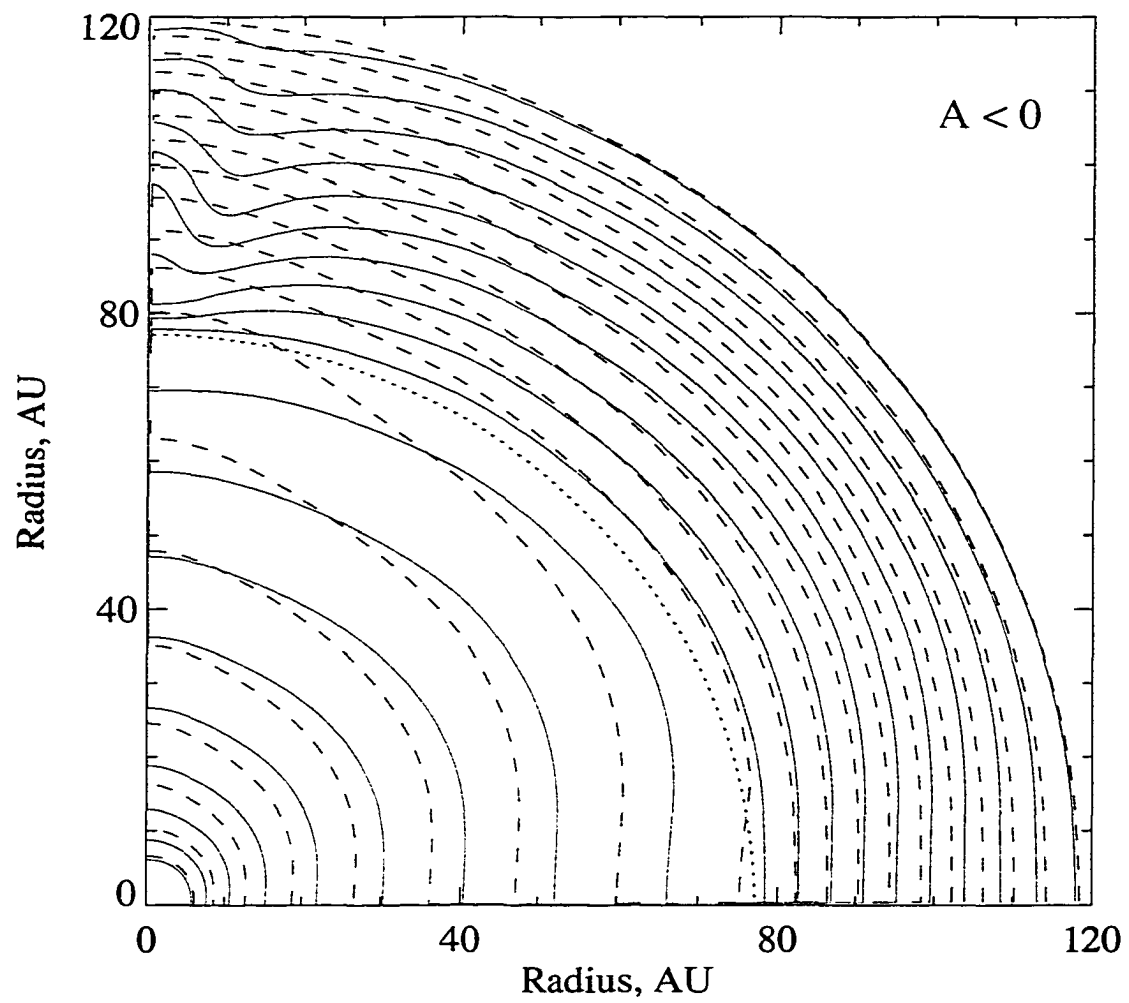


Figure 2.8 Same as in Fig. 2.7, but for $A < 0$. Latitudinal effects are the least important in this case and the contours are nearly spherical.

winds were ignored. The difference is quite small for $A > 0$ and is actually due to the changed position of the shock (the shock itself is drawn with dotted lines). However, for $A < 0$ there is a larger difference in particle intensity at high latitudes. This is the result of a higher degree of wind modification near the pole than in the $A > 0$ case.

Figures 2.8 and 2.10 show spectra of GCRs in the equatorial plane and over the pole for both solar cycles. Data plotted are from various balloon (BESS, LEAP) and Earth-orbiting spacecraft (IMP 8) experiments for the time periods close to the 1987 ($A < 0$) and 1996 ($A > 0$) solar minima. While spectra computed are somewhat higher, there will be additional modulation below 15 AU reducing the intensity at intermediate energies. Because the model does not extend to small radii, comparison with 1 AU observations is difficult, especially at the lowest energies. The focus of this research was on possible effects on the wind, rather than the study of the GCR modulation and therefore no special effort was taken to fit the data to the observation (such fits often require making rather arbitrary assumptions about the diffusion coefficient, see Section 1.1). Still, spectra computed are, in general, in good agreement with modulation models (e.g., *Burger and Hattings*, 1998). At about 1 GeV energy, there is a barely visible crossover in the spectra near the shock for $A < 0$. This is a result of re-acceleration happening at the shock, also seen by *le Roux and Ptuskin* (1995).

Radial distributions of the cosmic-ray pressure as well as the wind parameters are shown in Figures 2.4a,b. Notice that P_c has a maximum at the shock at low latitudes in the $A < 0$ case as a result of re-acceleration (this effect was described in *Kota and Jokipii*, 1993). In all cases the gas pressure near the shock is seen to adjust to conserve $P_c + P_g$

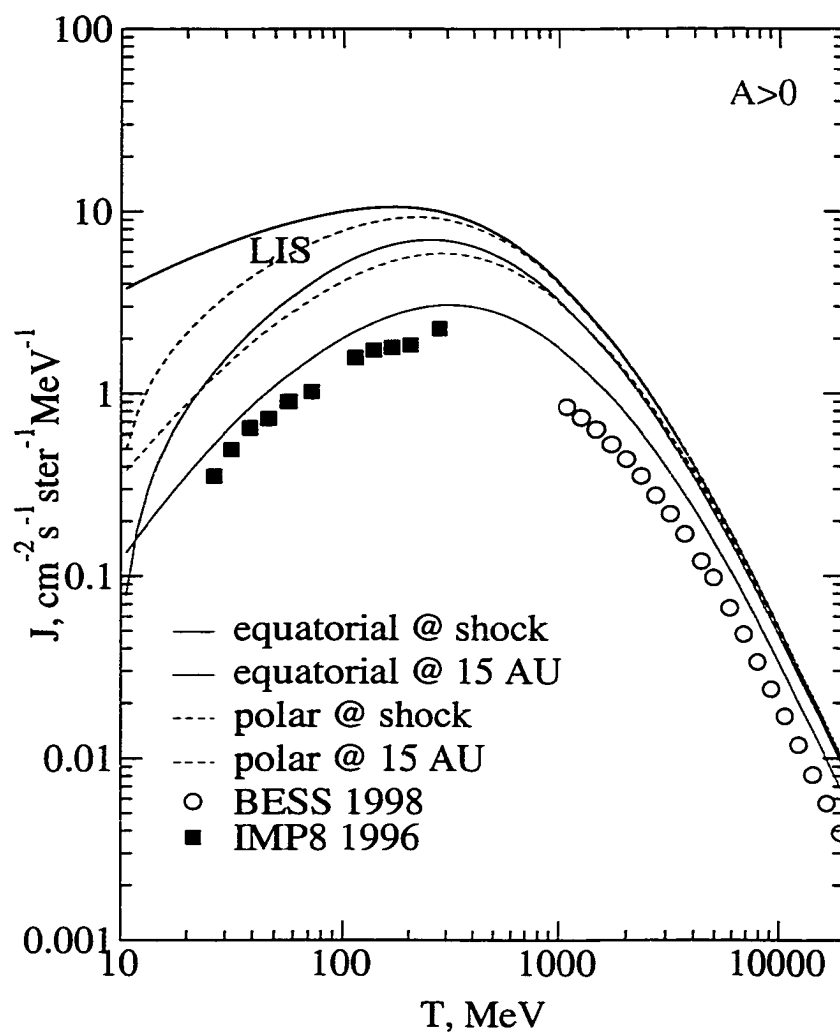


Figure 2.9 GCR spectra at 0 and 90 degrees latitude for $A > 0$. The curve labelled LIS is the assumed local interstellar spectrum at the modulation boundary. 1998 BESS data is from *Sanuki et al.* (1999); 1996 IMP 8 data is from *McDonald* (1998).

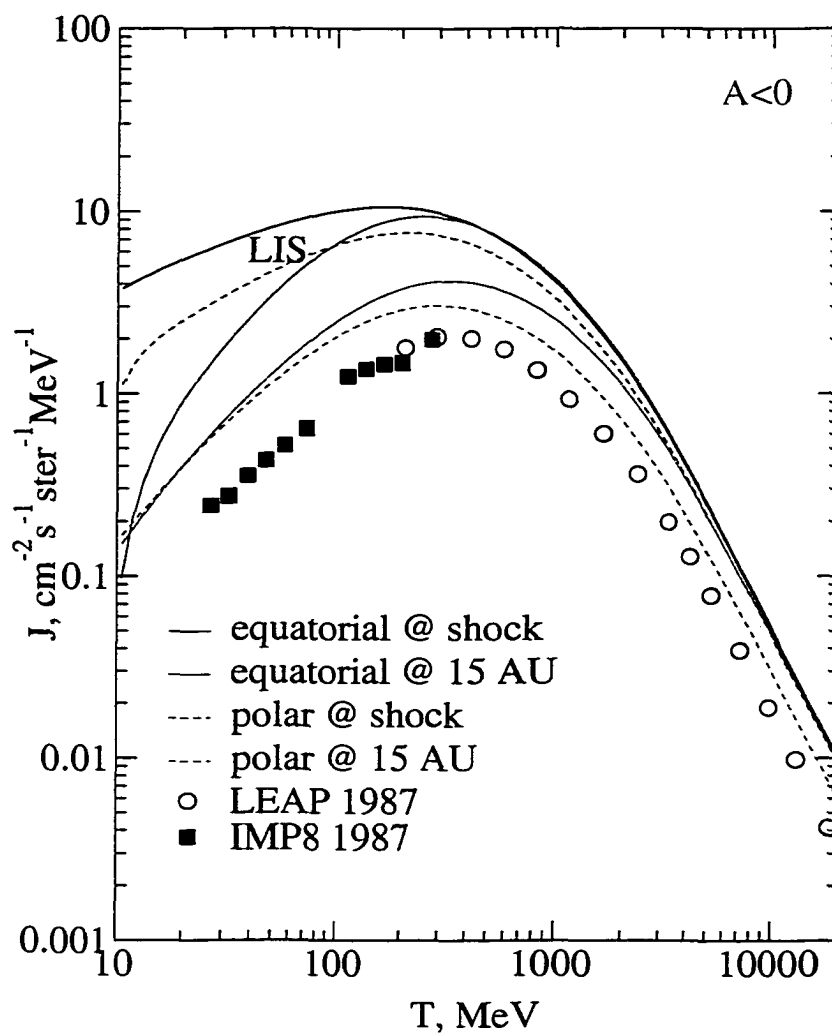


Figure 2.10 Same as Fig. 2.9, but for $A < 0$. 1987 solar minimum LEAP data are from *Seo et al.* (1991); 1987 IMP 8 data are from *McDonald* (1998).

according to (1.22) although the effect is not as visible in 2 dimensions.

2.9 Discussion

To determine what causes the wind deflection we performed a number of tests with some of the transport modes turned off. This let us determine that the major physical process that caused this effect was large and nonuniform radial drift. The general drift pattern described above creates strong latitudinal gradients in P_c , which deflect the wind in the ϑ direction. In fact, we were able to reproduce essentially the flow structure shown in Figure 2.2 by artificially imposing a time-independent cosmic-ray pressure gradient in only the ϑ direction (i.e., with $\partial P_c / \partial r = 0$). Because latitudinal drifts and diffusion tend to smooth ϑ gradients, the wind will be less affected if the diffusion coefficient were larger. The fact that the shock remains spherical despite an obviously non-spherical GCR distribution is probably due to the pressure boundary conditions which are spherically symmetric.

As mentioned before, we have found that the system continues to evolve on timescales comparable to the 11-year solar cycle. We would expect the flow to oscillate between the states shown in Figures 2.2 and 2.3. When following the system for a longer period of time, an inflow will occur in the polar region (for $A > 0$) or at the equator (for $A < 0$), because the flow turns aside and the fluid may enter from outside the domain. This situation cannot be handled adequately by the model because it would require specification of two more boundary conditions (for u and ρ), which are unknown. Should

an inflow occur, the magnetic field would be dragged along the lines separating the external flow and the solar wind. Because the field offers no resistance in this model, both B_θ and $B_{\theta,m}$ can become quite large in that region. Potentially, this would create magnetic "traps" with a very small diffusion coefficient, where particles would pile up and reach very high intensities. However, because this picture does not describe the real heliosphere (which has a contact surface separating the two flows), we have always stopped the simulation once an inflow was detected.

Conclusion: We have shown that an asymmetric solar wind flow pattern is possible in the region downstream of the termination shock, caused by galactic cosmic ray latitudinal pressure gradient. Because this is a purely 2-dimensional effect, caused by drifts, it has been overlooked in previous self-consistent models of the heliosphere.

CHAPTER 3

ANOMALOUS COSMIC RAYS IN A SELF-CONSISTENT MODEL

3.1 Introduction

We now turn to the study of the anomalous cosmic-ray effects on the solar wind in the framework of a kinetic, self-consistent model. As stated in Section 1.2, ACRs start out as interstellar pickup ions, directly injected into the acceleration process at the shock or pre-accelerated to higher energies in the other regions of the heliosphere. Pickup ions themselves are primarily produced by charge exchange of interstellar hydrogen with the solar wind protons. A newly created ion has have a speed $-u$ in the solar wind frame causing it to gyrate about the mean magnetic field in that frame. However, in the rest frame, the $u \times B$ electric field will cause it to drift \perp to B with the perpendicular (relative to B) component of the solar wind speed, which is essentially u everywhere at sufficiently large solar distances, except near the poles. The initial anisotropic distribution quickly relaxes to a spherical shell in velocity space due to rapid pitch-angle scattering by plasma waves with a subsequent "filling" of the interior of the shell due to adiabatic deceleration (*Vasyliunas and Siscoe, 1976*). At sufficient solar distances (beyond a few AU), the spectra have a "flat top" shape in the rest frame, extending to $2u$ in velocity space. These spectra were used to obtain the equation of state for the PUIs in the form $P_i \sim \rho_i u^2$ (where P_i is the PUI pressure and ρ_i is the PUI density) by *Chalov and*

Fahr (1996) and by *Fahr et al.* (2000). The problem with this approach, however, is that such an equation of state is locally isothermal and is not consistent with the polytropic equation of state that the authors used to describe both species. Additionally, pickup ion pressure described by the equation above would drop at the shock, which is physically incorrect – this equation therefore cannot be used in the downstream region.

Further evolution of the PUI distribution is possible if the diffusion in momentum space is fast enough. In this case the PUIs will relax to a Maxwellian distribution with a temperature different from that of the solar wind. This possibility has been studied by *Isenberg* (1986). Finally, the two species may reach a thermal equilibrium with each other. This possibility was rejected by *Isenberg* (1986) who obtained equilibrium times of thousands of years. However, in many cases the two–fluid equations may be combined together to yield a set of single–fluid equations as we will see in Appendix A. We adopt such an approach in this work with the exception of the pickup ion number density, which is computed separately for the purposes of the ACR injection (see Section 3.3).

The distribution of the neutral hydrogen atoms in the LIM and the heliosphere has also been a popular topic for global heliospheric modeling. To summarize the major findings, the interstellar neutrals are expected to pile up in the region of the LISM near the heliopause in the upstream region of the interstellar wind (*Baranov and Malama, 1993; Pauls et al., 1995; Zank, 1999*). This phenomenon, called the "hydrogen wall", can be understood by noting that the speed of the interstellar protons is considerably smaller than that of the neutrals in this regions (10 km/s vs. 25 km/s), because the former had their speed reduced at the bow shock and are being deflected by the heliopause. Because some of the H^0 is deflected around the heliopause, its density inside the heliosphere is

substantially lower than in the LISM (the effect known as filtration).

In the current work we do not include the hydrogen as a separate fluid, because the model does not extend into the interstellar medium. A simpler approach, using an analytic expression derived for the standard solar wind, is appropriate here, considering other limitations of the model.

This chapter is structured as follows. Section 3.2 describes the solar wind model used, including the PUI production from the interstellar neutrals. Then, in Section 3.3, we discuss the diffusion model used and ACR injection. Sections 3.4 and 3.5 focus on numerical routines, in particular, on the adaptive mesh refinement technique used to improve resolution at the shock. Sections 3.6 and 3.7 describe the results and the discussion is given in Section 3.8. In Appendix A we derive a set of three-fluid equations for the PUI-wind appropriate for certain cases when thermalization between the species does not occur. Appendix B offers a discussion of a new feature that we found in ACR spectra.

The contents of this chapter will be included in the paper to be submitted to the *Astrophysical Journal*, currently in preparation (*Florinski and Jokipii, 2001*).

3.2 New solar wind–PUI model

The solar wind model is a direct descendant of the model described in Section 2.2 and reported in *Florinski and Jokipii (1999)*. Several enhancements have been made to accommodate pickup ions and the new ACR injection model, described in the next

section. Both the solar wind and the PUIs are described by single fluid equations. The energy equation can be obtained by adding (A.10) and (A.11) together (see Appendix A). This approach has been used in a majority of heliospheric models (*Baranov and Malama, 1993; Pauls et al., 1995; Banaszkiwicz and Ziemkiewicz, 1997*). A somewhat better approach was introduced by *Isenberg (1986)* who solved individual equations for the three plasma species, similar to (A.10) and (A.11). This however complicates the system considerably because there are 3 temperatures to keep track of. The idea is to solve the total momentum and energy equations which are indistinguishable from the ordinary one-fluid equations, except for the source terms, using the usual Godunov method and then compute T_p and T_e separately to use these in the charge exchange terms (to simplify things, one can use the approximation $T_p=T_e$). Because our primary focus is on cosmic rays, however, a simpler, one-fluid SW approximation is sufficient.

The mass, momentum and energy conservation equations are

$$\frac{\partial \rho}{\partial t} + \frac{1}{r^2} \frac{\partial(\rho u r^2)}{\partial r} + \frac{1}{r \sin \vartheta} \frac{\partial(\rho v \sin \vartheta)}{\partial \vartheta} = 0 \quad (3.1)$$

$$\frac{\partial(\rho u)}{\partial t} + \frac{1}{r^2} \frac{\partial(\rho u^2 r^2)}{\partial r} + \frac{1}{r \sin \vartheta} \frac{\partial(\rho u v \sin \vartheta)}{\partial r} + \frac{\partial P_g}{\partial r} = -\frac{\partial P_c}{\partial r} - Q_{u,ce} \quad (3.2)$$

$$\frac{\partial(\rho v)}{\partial t} + \frac{1}{r^2} \frac{\partial(\rho u v r^2)}{\partial r} + \frac{1}{r \sin \vartheta} \frac{\partial(\rho v^2 \sin \vartheta)}{\partial r} + \frac{1}{r} \frac{\partial P_g}{\partial \vartheta} = -\frac{1}{r} \frac{\partial P_c}{\partial \vartheta} - Q_{v,ce} \quad (3.3)$$

$$\begin{aligned} & \frac{\partial}{\partial t} \left(\frac{\rho(u^2+v^2)}{2} + \frac{P_g}{\gamma-1} \right) + \frac{1}{r^2} \frac{\partial}{\partial r} \left[u r^2 \left(\frac{\rho(u^2+v^2)}{2} + \frac{\gamma P_g}{\gamma-1} \right) \right] \\ & + \frac{1}{r \sin \vartheta} \frac{\partial}{\partial \vartheta} \left[v \sin \vartheta \left(\frac{\rho(u^2+v^2)}{2} + \frac{\gamma P_g}{\gamma-1} \right) \right] = -u \frac{\partial P_c}{\partial r} - \frac{v}{r} \frac{\partial P_c}{\partial \vartheta} \\ & - Q_{e,ce} - Q_{e,inj} - Q_{e,bnd}. \end{aligned} \quad (3.4)$$

The last two terms in (3.4) due to ACR injection and cooling will be discussed in the next section. The terms with the subscript "ce" are due to charge exchange and are considered below. These were derived in *McNutt et al.* (1998) (see also *Holzer, 1972; Pauls et al., 1995*), who obtained collision integrals for the case of two Maxwellian fluids (solar wind protons and neutral atoms). Noting that electrons are not exchanged in the process, the source terms are

$$Q_{u,ce} = \sigma(U_M) N U_M \rho(u - u_H), \quad Q_{v,ce} = \sigma(U_M) N U_M \rho(v - v_H) \quad (3.5)$$

$$Q_{e,ce} = \sigma(U_M) N \left[U \left(P_g - \frac{2\rho kT_H}{m_p} \right) + U_M \frac{\rho(u^2 - u_H^2)}{2} \right], \quad (3.6)$$

where U and U_M are the "effective interaction speeds", σ is the charge exchange cross-section, N is the number density of the neutral atoms and T_H is their temperature. The interaction speeds (from *McNutt et al., 1998*) are:

$$U = \left[\frac{8}{\pi} \left(\frac{P_g}{2\rho} + \frac{kT_H}{m_p} \right) + (u - u_H)^2 \right]^{1/2} \quad (3.7)$$

$$U_M = \left[\frac{128}{9\pi} \left(\frac{P_g}{2\rho} + \frac{kT_H}{m_p} \right) + (u - u_H)^2 \right]^{1/2}. \quad (3.8)$$

The charge exchange cross-sections have been measured by *Fite et al.* (1962). Their dependence on the relative speeds Δw of the two interacting particles (a proton and a neutral atom) is described by the following empirical formula

$$\sigma(\Delta w) = (2.1 \times 10^{-7} - 9.2 \times 10^{-9} \ln \Delta w)^2 \quad (3.9)$$

which gives σ in cm^2 for Δw in cm/s . The characteristic speeds (3.7) and (3.8) were

obtained in *Pauls et al. (1995)* and *McNutt et al. (1998, 1999)* by noting $\sigma \approx \text{const}$ and evaluating transfer integrals to first order in $(\Delta w - U)$.

Because the model described here can only be applied to the upstream heliosphere relative to the interstellar wind, we identify $\vartheta = \pi/2$ with the direction towards the "nose" of the heliopause. This approximation is quite good because the interstellar wind is moving approximately parallel to the ecliptic plane (*Suess and Nerney, 1997*). The neutral atoms then have these velocities in the chosen coordinate frame:

$$u_H = -V \sin \vartheta, \quad v_H = -V \cos \vartheta, \quad (3.10)$$

where $V = 25 \text{ km/s}$ (*Frisch, 1997*) is the relative speed of the solar system in the local interstellar medium. The density of the neutrals was taken from *Axford (1972)*

$$N = N_{HP} \exp \left[-\frac{r_0 (\pi/2 - \vartheta)}{r \cos \vartheta} \right]. \quad (3.11)$$

This expression takes into account the attenuation due to charge exchange and the fact that the neutrals have to traverse a larger "optical depth" at high latitudes. The penetration depth r_0 is 4AU (*Axford, 1972*), and N_{HP} is the density of interstellar hydrogen inside the heliopause (i.e., after attenuation by the filtration region). This quantity is not very well known due to large uncertainties in current measurements. It is generally agreed that the LISM density of hydrogen is $0.1\text{--}0.2 \text{ cm}^{-3}$ from measurements of Lyman α absorption from nearby stars (*Frisch, 1997*). Additionally, back-scattering of the solar ultraviolet light from hydrogen atoms in the heliosphere allows more direct measurement of the the local H^0 density. Such measurements, are, however, model dependent and the results vary significantly (*Qu  merais et al., 1996*). *Gloeckler et al.*

(1997) obtained N_{HP} between 0.09 and 0.14cm⁻³ by measuring the actual PUI distribution at Ulysses and modeling PUI production in the solar wind. In this work we use $N_{HP}=0.1\text{cm}^{-3}$ because larger N would produce an unreasonably large amount of solar wind deceleration. The temperature of the neutral hydrogen was taken to be $T_H=10^4\text{K}$, which is in agreement with model calculations based on temperature in the LISM of $8\times 10^3\text{K}$ (e.g., *Fahr et al.*, 2000).

The solar wind density and speed were allowed to vary in latitude according to the modern concept of the solar wind's origin (fast, hot wind from the coronal holes, slow, cooler wind from the streamer belt region, see *Axford and McKenzie*, 1997). This produces a variation in the wind dynamic pressure $\rho u^2/2$ with latitude. Because the dynamic pressure is higher in the polar regions, the termination shock will be located farther away over the poles than in the ecliptic, according to (2.12) i.e., the shock is no longer spherical (see *Barnes* 1998 for an analytic model of the latitude-varying solar wind). We use the following expression for the wind speed variation:

$$u(\vartheta)=u_0\left\{1+a\left[1+\text{Erf}\left(b\sin(\vartheta-\pi/4)-c\right)\right]\right\}, \quad (3.12)$$

and a similar one for the density. The actual values of the solar wind parameters appropriate for the time near the solar minimum that determine the coefficients a , b and c , are from the Ulysses measurements reported by *Goldstein et al.* (1996). The solar wind parameters at 1AU are summarized in Table 3.1. In this model, $b=6.2$, $c=1.9$, and $a=0.65$ for the density and -0.2 for the radial velocity.

The solar wind dynamic pressure is 20% higher over the poles which means the shock will be located approximately 10% farther away from the Sun. At intermediate latitudes,

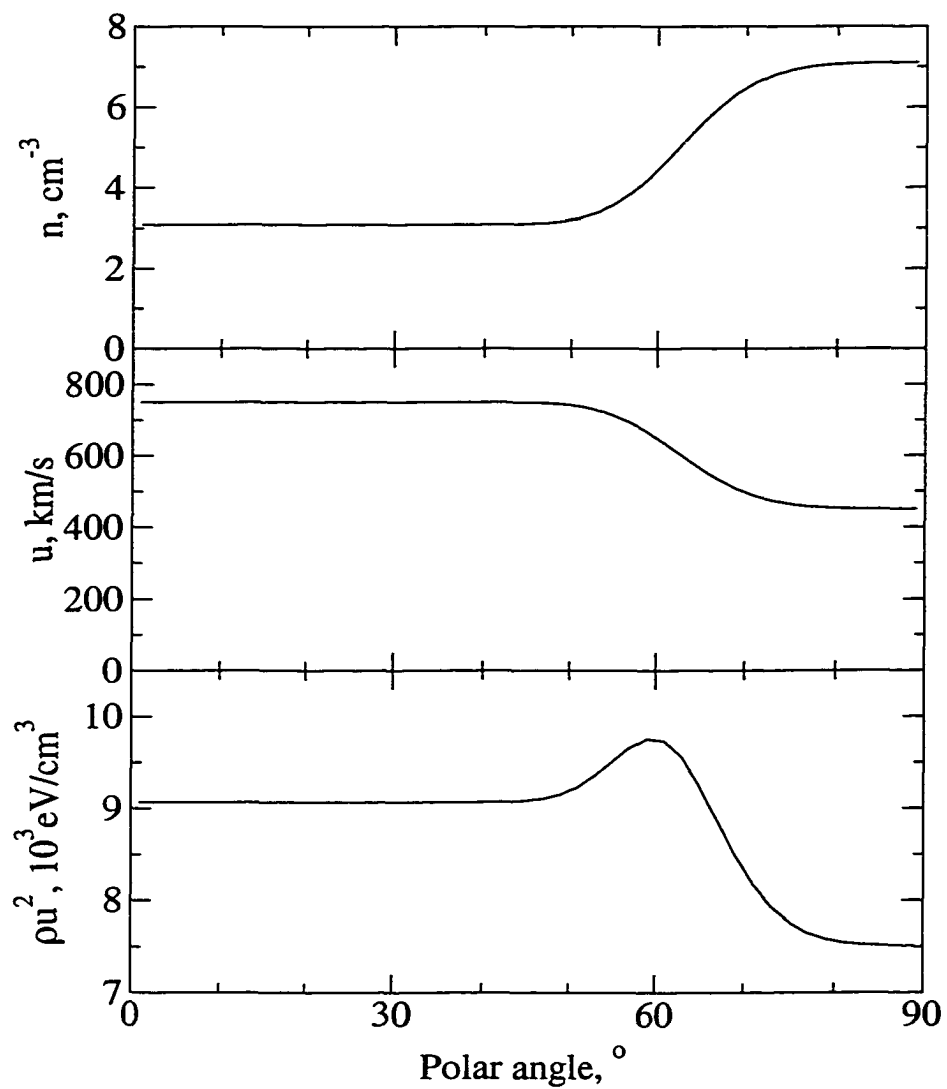


Figure 3.1 Solar wind number density, velocity and momentum flux at 1 AU as a function of latitude. The functional dependence approximates the Ulysses measurements (*Goldstein et al.*, 1996).

we assume an error–function–like dependence of ρ and u on latitude with the slow wind extending to about 30% above the ecliptic plane, while the temperature varies linearly with u , according to *Goldstein et al.* (1996). Density, velocity and dynamic pressure in the solar wind at 1 AU are shown in Figure 3.1.

Table 3.1 Solar wind parameters at 1 AU.

	u , km/s	n , cm ⁻³	T , K	$\rho u^2/2$, eV/cm ³
Fast wind	750	3.1	2.6×10^5	9.1×10^3
Slow wind	450	7.1	1.1×10^5	7.5×10^3

For the magnetic field we use the model as described in Section 2.3 (also *Florinski and Jokipii*, 1999), including the modified component and a wide current sheet. The external gas pressure was 1.45 eV/cm^3 for case I, for the shock location between 80 AU in the ecliptic and 90 AU at the poles, and 1.1 eV/cm^3 for case II, positioning the shock between 90 and 100 AU. The amount of deceleration due to pickup ions was of the order of 50 km/s, so that the wind slowed down to 390 km/s at 60 AU in the equatorial regions, which is consistent with the recent Voyager measurements (*Wang et al.*, 2000).

3.3 New ACR model

Both galactic and anomalous cosmic rays are described by the same transport equation from Chapter 2 (Eq. 2.25 for the case of GCRs). The only difference is that for the ACRs injection needs to be included in the transport equation. Before discussing injection, however, we will describe the diffusion coefficients we use here, which are different

from (2.32).

The choice of the parallel diffusion coefficient was prompted by the work of *Zank et al.* (1998) and *le Roux et al.* (1999) who used the coefficient predicted by the QLT. As shown in *Jokipii* (1966), diffusion parallel to the mean magnetic field is caused by resonant pitch–angle scattering off the turbulence in the solar wind. The power spectrum of the turbulence contains two distinctly different regions: an energy interval at small wavenumbers (k), where turbulence is generated, and an inertial interval at large wavenumbers, where energy is transferred to smaller and smaller scale fluctuations (a process called the turbulent cascade). The spectral shape is such that in the energy range the power spectrum is a constant while in the second regime $P_{\perp} \sim k_{\parallel}^{-5/3}$ (Kolmogorov law) for a slab turbulence (where \perp and \parallel are relative to the mean field \mathbf{B}). Cosmic rays scatter mostly off of the turbulence with wavelengths of the order of their gyroradii ($k_{\parallel} \sim r_g^{-1}$). For a power spectra of the form

$$P_{\perp} = \frac{C}{1 + (k_{\parallel} l_c)^{5/3}}, \quad (3.13)$$

where l_c is the correlation length and corresponds to the transition between energy and inertial intervals, *le Roux et al.* (1999) and *Giacalone and Jokipii* (1999) compute the QLT parallel diffusion as

$$\kappa_{\parallel} \simeq \frac{27}{35} \frac{r_g^{1/3} l_c^{2/3} w}{A^2} \left[\frac{7}{27} \left(\frac{r_g}{l_c} \right)^{5/3} + 1 \right], \quad (3.14)$$

where $A^2 = \delta B_{\perp}^2 / B^2$ is the amplitude of only the slab turbulence. Equation (3.14) shows that diffusion scales as $p^{1/3}$ for low–energy particles, but changes to p^2 at high energies.

This is due to the fact that lower energy particles resonantly interact with waves in the inertial range, while high energy particles interact in the flat part of the spectrum in the energy interval.

The behavior of the amplitude A and correlation length l_c of the fluctuations in the heliosphere has been studied by *Zank et al.* (1996) and used to obtain diffusion coefficients in *le Roux et al.* (1999). In the short wavelength limit (WKB approximation), the amplitude of Alfvénic turbulence $\delta B_{\perp}^2 \sim r^{-3}$ (*Hollweg, 1974*) when there is no source of turbulence except at the Sun. When including sources, such as interactions of fast and slow solar wind streams and wave generation by the pickup ion isotropization process, the situation is considerably more complex and the fluctuation power decreases less rapidly with distance (between r^{-1} and r^{-3} , depending on which process dominates). Comparison with Pioneer and Voyager magnetometer observations performed by *Zank et al.* (1996) indicate that an intermediate value agrees best with the data. One would therefore expect A^2 at high latitudes to increase if $B^2 \sim r^{-4}$ and to be a constant if $B^2 \sim r^{-2}$ (same as at low latitudes). In this work, we take a constant value of $A=0.06$ everywhere in the heliosphere, with a correlation length $l_c=0.03\text{AU}$ ($l_c \equiv \text{const}$ in the WKB limit). These values produce the best agreement between computed and observed ACR spectra.

For the perpendicular diffusion coefficient we use a form similar to (2.33) for the GCRs, in this case

$$\kappa_{\perp} = \frac{1}{2} A^2 \kappa_{\parallel}. \quad (3.15)$$

This dependence is consistent with hybrid simulation results of *Giacalone and Jokipii (1999)*. However, the absolute value used here is larger, even if we take the slab

turbulence to be 20% of the total slab+2D. For this κ_{\perp} , perpendicular diffusion is the primary ACR transport mechanism in the solar wind near the termination shock because drifts are significantly smaller at such low energies.

Before we describe the injection model, it is important to establish the lower energy limit on the process of diffusive shock acceleration. The condition $\kappa_{rr}/u > r_g$ (Jokipii, 1987) may not be sufficient, despite being used by *le Roux and Fichtner* (1997) to argue that 1keV pickup ions can be readily injected into the acceleration process. A more appropriate condition is that the total anisotropy (*Gleeson and Axford*, 1967) should be small:

$$|\xi| = \frac{3|S|}{4\pi J} \ll 1, \quad (3.16)$$

where $J = fp^2$ is the differential intensity. To evaluate this upstream of the shock, consider that the CR gradients are mostly in the radial direction. We can estimate the radial gradient from the condition that diffusion balances convection, i.e.,

$$\frac{\partial f}{\partial r} \simeq \frac{u}{\kappa_{rr}} f. \quad (3.17)$$

The streaming flux (2.28) can be written as (assuming $B_{\theta} \simeq 0$ and $f \sim p^{-4}$):

$$S = -\frac{4\pi p^2}{w} \left[\left(\kappa_{rr} \frac{\partial f}{\partial r} + \frac{up}{3} \frac{\partial f}{\partial p} \right) e_r - \frac{pcw}{3e} \frac{B_{\phi}}{B^2} \frac{\partial f}{\partial r} e_{\theta} \right]. \quad (3.18)$$

Evaluating (3.16) and using (3.14) and (3.15) then gives the following condition:

$$|\xi| = \begin{cases} \frac{u}{w}, & \parallel \text{ shock (pole)} \\ \frac{u}{w} \sqrt{1 + \left(\frac{35}{81} \frac{r_g^{4/3}}{l_c^{4/3}} \right)^2}, & \perp \text{ shock (equator)} \end{cases} \quad (3.19)$$

using the low energy limit in (3.14). One can see that the basic condition for the diffusion theory to be valid remains essentially the same for perpendicular shocks, i.e., $u \ll w$ (this is due to a weak dependence of κ_{\perp} on momentum at low energies), which means that the lowest ACR energies allowed are a few tens of keV.

Because there is a gap in energy between keV PUIs and the ACRs that cannot be modeled with a transport equation, we are compelled to use certain assumptions about the production rate. We assume that a certain portion of PUIs is accelerated to the injection energy T_{inj} , which is taken to be 100keV here. The injection term is similar to (1.23), but with gas density replaced by pickup ion density n_i :

$$Q_{inj} = \frac{\eta}{4\pi p_{inj}^2} n_i u \delta(r - r_{sh}) \delta(p - p_{inj}), \quad (3.20)$$

where p_{inj} is the momentum corresponding to T_{inj} and r_{sh} is the shock distance. This term has to be added to the right hand side of Eq. (3.4). The free parameter η describes the efficiency of PUI preacceleration to 100keV and is chosen by comparing resulting ACR spectra with the Voyager data.

To conserve total energy, appropriate terms must be subtracted from the combined SW+PUI equation (3.4) to balance injection. Taking the second moment of (3.20) we obtain

$$Q_{e,inj} = \eta n_i u T_{inj} \delta(r - r_{sh}). \quad (3.21)$$

To find PUI density, we use a separate continuity equation (see A.5):

$$\frac{\partial n_i}{\partial t} + \frac{1}{r^2} \frac{\partial(n_i u r^2)}{\partial r} + \frac{1}{r \sin \vartheta} \frac{\partial(n_i v \sin \vartheta)}{\partial \vartheta} = \sigma(U) N U \left(\frac{\rho}{m_p} - n_i \right). \quad (3.22)$$

The correct term on the RHS would include U computed using solar wind temperature only. Eq. (3.22) should be a good approximation in the upstream region, where $n_i \ll n_p$.

Energy lost through the lower momentum boundary due to cooling can be found by integrating the transport equation (2.25) from p_{min} to ∞ (see Zank *et al.*, 1993). This has to be added to the SW+PUI energy equation:

$$Q_{e,bnd} = \frac{4\pi}{3} T_{min} p_{min}^3 f(p_{min}) (\nabla \cdot \mathbf{u}), \quad (3.23)$$

where T_{min} is the energy corresponding to p_{min} . In this paper we use $T_{inj} = T_{min}$. Note that cooling below the energy threshold is handled by (2.25) automatically and there is no need for a boundary condition in this case. The computational domain in momentum space contains 140 logarithmically spaced intervals between $p_{min} = 100 \text{ keV}$ and $p_{max} = 1 \text{ GeV}$. At the largest energy we take $f(p_{max}) = 0$ as a boundary condition.

3.4 Adaptive mesh refinement technique

The numerical model for the solar wind–cosmic ray interaction described in Section 2.5 works quite well for the purely gas dynamic case and for GCR–modified winds. It, however, becomes inadequate should we decide to include the anomalous cosmic rays.

The reason for this is the small diffusive length scale of these low-energy particles. Indeed, for a typical magnetic field strength of $5 \times 10^{-7} \text{Gs}$ just upstream of the termination shock, Eqs. (3.14) and (3.15) give perpendicular diffusion coefficients $\sim 3 \times 10^{24} \text{cm}^2/\text{s}$ for 1GeV protons and $\sim 6 \times 10^{20} \text{cm}^2/\text{s}$ for 1MeV protons. With a wind speed of the order of $5 \times 10^7 \text{cm/s}$, we obtain a radial diffusive length, κ_r/u , of thousands of AU at high energies, but less than 1AU at low MeV energies. Because the ACR distribution is dominated by the low-energy particles, especially at low latitudes, we need a much higher resolution than the 1 AU used in the GCR model of Chapter 2. The problem is, increasing resolution by a factor of 2 in a 2-D model results in an increase in computation time of a factor of 8 and an increase in memory use of a factor of 4 (assuming we are increasing resolution in both dimensions).

Actually, increasing resolution everywhere in the simulation domain is not necessary. The important region is the termination shock itself where ACR acceleration takes place. Indeed, numerically solving Eq. (2.25) will give correct results regardless of how small κ_r is, because the gradients are generally small away from the shock. To solve the problem efficiently, selective refinement of the grid in the vicinity of the shock is required.

There are several ways to achieve this goal. The simplest is to use a variable grid with points concentrated near discontinuities. This approach has a difficulty however: the time step is constrained by the stability criteria for the smallest Δr or $\Delta \theta$. Even when the refined area is small, the rest of the domain still has to be computed using this finer time step. Additionally, it doesn't work well in 2 dimensions, because concentrating points in

some area means they must spread apart more elsewhere, and it is impossible to have more grid points than there were initially in any direction.

Adaptive mesh refinement (AMR) is a more sophisticated approach. Here the goal is to cover a discontinuity with a set of grid points or grid patches with a significantly smaller Δr and $\Delta \theta$. Methods that refine individual grid points are not very popular due to the complicated bookkeeping involved. These have been used for cometary winds (e.g., *Gombosi et al.*, 1994). The more popular method that we also adopt here refines rectangular patches (also called grids) rather than individual cells. The method we use was first introduced in *Berger and Olinger* (1984) and further developed in *Berger and Colella* (1989).

The numerical solution algorithms for the solar wind work exactly the same on adaptive grids as they do on a single fixed grid. From now on we will assume that the refinement factor is always 2, i.e., each level l grid cell may be covered by 4^{l+1} grid cells (level 0 being the original unrefined grid, also called the base grid). In this way, we solve equations (3.1)–(3.4), for instance by the same second–order Godunov–type method described in Chapter 2. Finer grids have a smaller value of the time step, Δt (to satisfy numerical stability criteria), and thus have to be integrated more often than the base grid (i.e., twice as often for a level $l+1$ grid, 4 times as often for a level $l+2$ grid, etc.). This is still a huge improvement because only a small part of the domain is covered by the fine grid. The rest is computed using the Δt that corresponds to the coarser grid. Later in this section we will compare typical computation requirements for AMR methods with these for refinement of the entire domain.

Two important points must be made here concerning interactions between coarse and fine grids. First, before taking the next coarse grid time step, a check must be made whether the cell is covered by a fine grid. If it is, values of the variables on the coarse grids are discarded and replaced with the average of the four subgrid cells. Second, the finite differencing scheme (2.46) itself must be modified at coarse grid cells that abut any fine grids, but are not themselves covered by such grids. The latter is actually not implemented in the code because flux conservation is not a problem for smooth flows on both sides of the shock.

The most difficult part about AMR is grid generation. We will now describe the steps that produce a set of nested grids covering a discontinuity region. All operations are performed on all level l grids, except the finest (l_{\max}), in the direction from $l_{\max}-1$ to 0. The result is a set of refined (level $l+1$) grids. These steps are illustrated in Fig. 3.2. The steps are:

- 1) Flag grid points in every grid on level l that contain a discontinuity (Fig. 3.2a). We use the density gradient as a discontinuity check. Once the gradient in either the r or θ direction exceeds a certain limit, the code assumes there is a discontinuity and flags the cell.
- 2) Flag all cells in a "buffer zone" around the discontinuity (Fig. 3.2b). This is done to ensure that discontinuities stay well within the fine grid boundaries, which is particularly important for moving shocks. Even for quasi-stationary shocks it is not desirable for the shock itself to abut the boundary of a coarse grid.
- 3) Flag those cells that are covered by level $l+2$ grids. This ensures that each level

$l+2$ grid will be completely contained within the newly created $l+1$ set of grids.

Note that any particular level $l-2$ grid does not have to be contained within a single $l+1$ grid, but can, in fact, be lie within any number of such grids. This step is not shown in Fig. (3.2).

- 4) Create the initial rectangular grid patch containing all flagged grid cells. This patch is then divided in two along the longest edge. The halves are checked for efficiency, measured as the ratio of the number of flagged cells to the total number of cells. If the required efficiency is reached, the process is stopped and the operation is performed on the next patch. If a grid contains no flagged cells, it is discarded. This procedure is repeated recursively on the newly created patches until the desired efficiency is reached (Fig. 3.2c and 3.2d).
- 5) From Fig. 3.2d, we can see that after the bisection step many small (often only 1×2 cell) patches are created. These will be extremely inefficient to solve because of a large perimeter to area ratio. Indeed, updating boundary conditions for such grids would consume more time than advancing the solution. To eliminate small grids, we use a merging algorithm. This method checks if a larger grid containing any two smaller grids will still satisfy the efficiency criterion, while not increasing the area significantly. In this way, only the smaller grids are incorporated, while larger grids increase in size only slightly (Fig. 3.2e).

The resulting set of grids is then converted to level $l+1$ and filled with data from the old $l+1$ grids, if such are available, or level l grids if not.

Efficient solution of the wind and cosmic-ray equations for each grid requires fast and

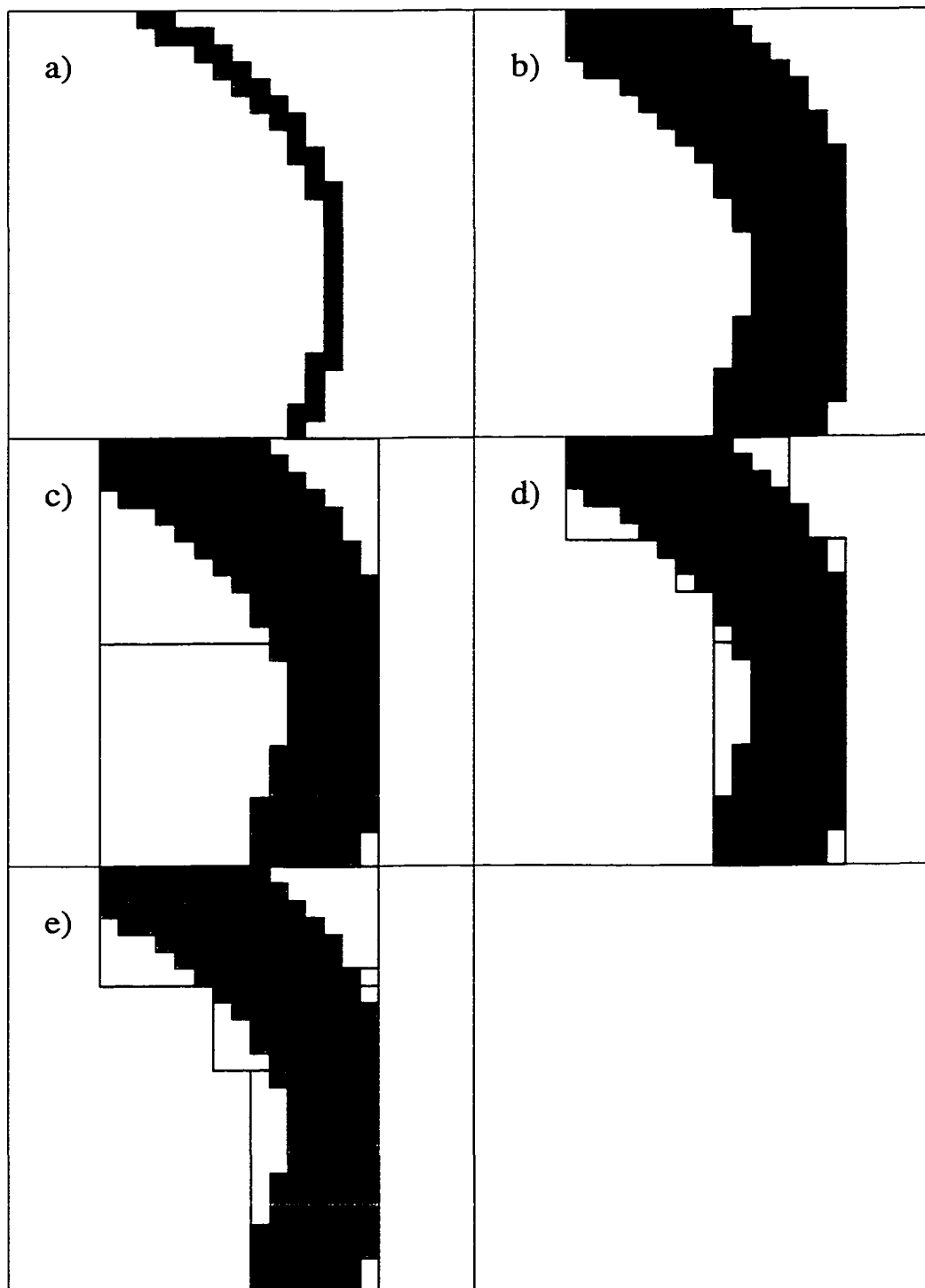


Figure 3.2 "Snapshots" of the AMR grid generation procedure used in this work. Each step is explained in the text.

easy access to neighboring, intersecting, parent or nested grids. Our numerical code uses an object-oriented approach to a multiple grid situation. Each grid is represented by an object (Fig. 3.3) that contains pointers to other grids that are in various relationships with it. In particular, intersecting and parent grids are needed to fill in boundary conditions, while subgrids are used to update the solution from the fine grids, which will be more accurate. Each grid contains a set of solvers (solar wind, cosmic-ray or magnetic field in our case) that have both the data arrays and the procedures to advance the solution. Because of this modular architecture, a new solver can be easily added, if desired, without modifying to the rest of the code. The grids themselves are linked in a list with each grid pointing to the next. A special set of four border grids at the end of the list is used to fill in physical boundary conditions for grids whose edges are part of the global boundary of the domain. The code is written in the C++ language and is capable of using multiple CPUs on shared-memory computers by running several threads from within the single program.

We will now demonstrate the efficiency of the AMR approach on a simple example. Suppose we have a shock that is mostly aligned with θ -gridlines (this is the case for the TS). Suppose also that the original domain is $N \times M$ grid cells. Because of the linear nature of the discontinuity, each level of refinement contains a fixed number of cells (K) in the r direction. The total number of cells can be estimated as

$$N_{cells} = NM + \sum_{l=1}^{l_{max}} 2^l KM, \quad (3.24)$$

and the total number of time steps required can be written as

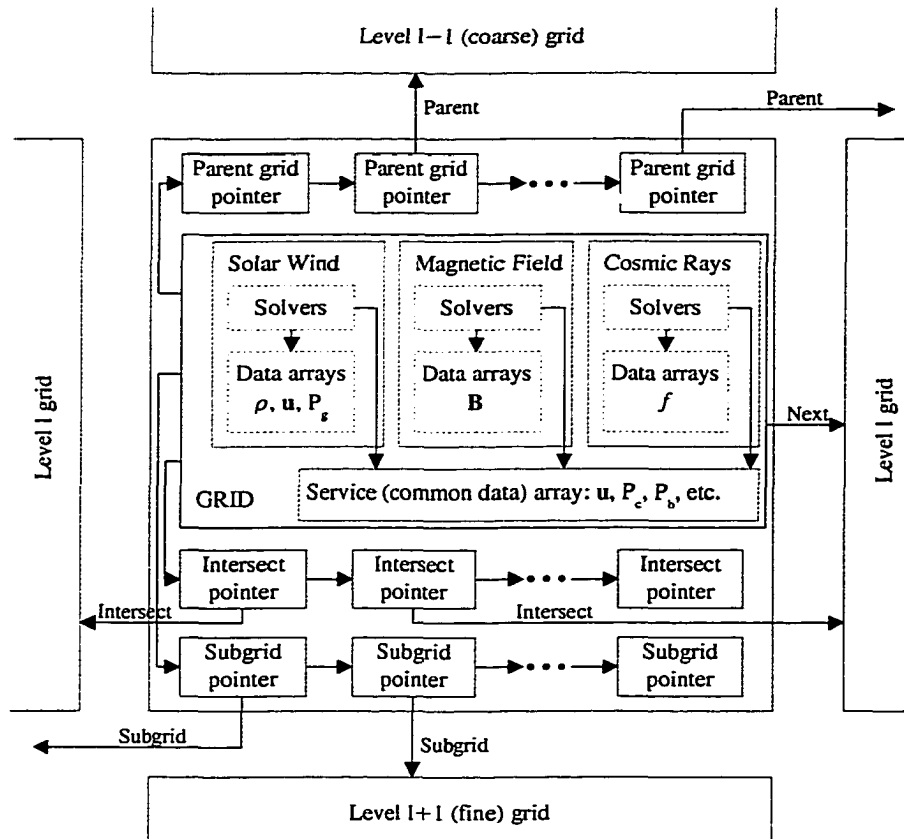


Figure 3.3 Computer representation of the adaptive mesh hierarchy based on an object-oriented model. Each grid structure (shown in the middle) contains data arrays and solvers as well as pointers to parent-, intersecting- and sub-grids.

$$T_{comp} = T \left(1 + \sum_{i=1}^{l_{max}} 2^{2i} \frac{K}{N} \right), \quad (3.25)$$

where T is the number of time steps required to solve the problem without the mesh refinement. Taking $N=100$, $M=50$, $K=10$ and 3 levels of refinement, we find that $N_{cells}=12000$ which is only a factor of 2.4 increase. A full refinement of course requires a factor of 64 increase in storage requirements. The results are even more impressive for the computation time which give $T_{comp}=8.4T$ for AMR vs. 512 (!) for a full refinement. In reality, the improvement is somewhat lower due to the fact that the shock is not always aligned with the gridlines, grid inefficiency factor, and boundary overhead. Still, even for a typical value of $T_{comp} \sim 15T$, AMR has a commanding lead over any other method of solution.

3.5 Numerical integration of the cosmic-ray equation

The numerical scheme similar to that described in Section 2.6 was used to solve the transport equation 2.25 with the source term 3.20. One should remember that the scheme is no longer strictly implicit because the nested grids do not extend all the way to the physical boundaries. At the boundaries of the fine grids, fixed (Dirichlet) conditions must be used with values taken from the coarse (or adjacent fine) grids. This implies that the scheme is no longer unconditionally stable, and the time step has to be reduced. Experimenting, we found that reducing the time step by at least a factor of 2 was required to achieve stability. In addition, we found that the cosmic-ray code requires

more frequent grid updates than the solar wind part, thus adding more overhead to the scheme.

Two important modifications were made to improve stability in the AMR case. First, a third step was added in addition to (2.59) and (2.60) to calculate advection in momentum space implicitly:

$$\left(1 - \frac{\Delta t}{2} L_{pp}\right) f^{new} = f^{t+1} - \frac{\Delta t}{2} L_{pp} f^t, \quad (3.26)$$

where f was computed in (2.60). This step improves stability for the advection in momentum space at the shock, where L_{pp} is the largest.

The second improvement involved drift velocities at high energies at the shock. For a shock aligned with the ϑ grid lines, drift velocity (2.30) becomes very large due to a jump in B_ϕ . What's more, while the jump itself remains constant for grids on all levels, the gradient is larger on the finer grids, due to smaller Δr . We found that this could lead to an instability in some cases. There is, however, a simple way to overcome this difficulty. As noted in *Isenberg and Jokipii* (1979), particles sample the field along their gyroorbit so that drift velocities may be averaged over scales smaller than r_g with no loss of accuracy. This averaging is particularly easy to perform in the AMR scheme because the average values can be simply taken from coarser grids. This step incurs almost no computational overhead.

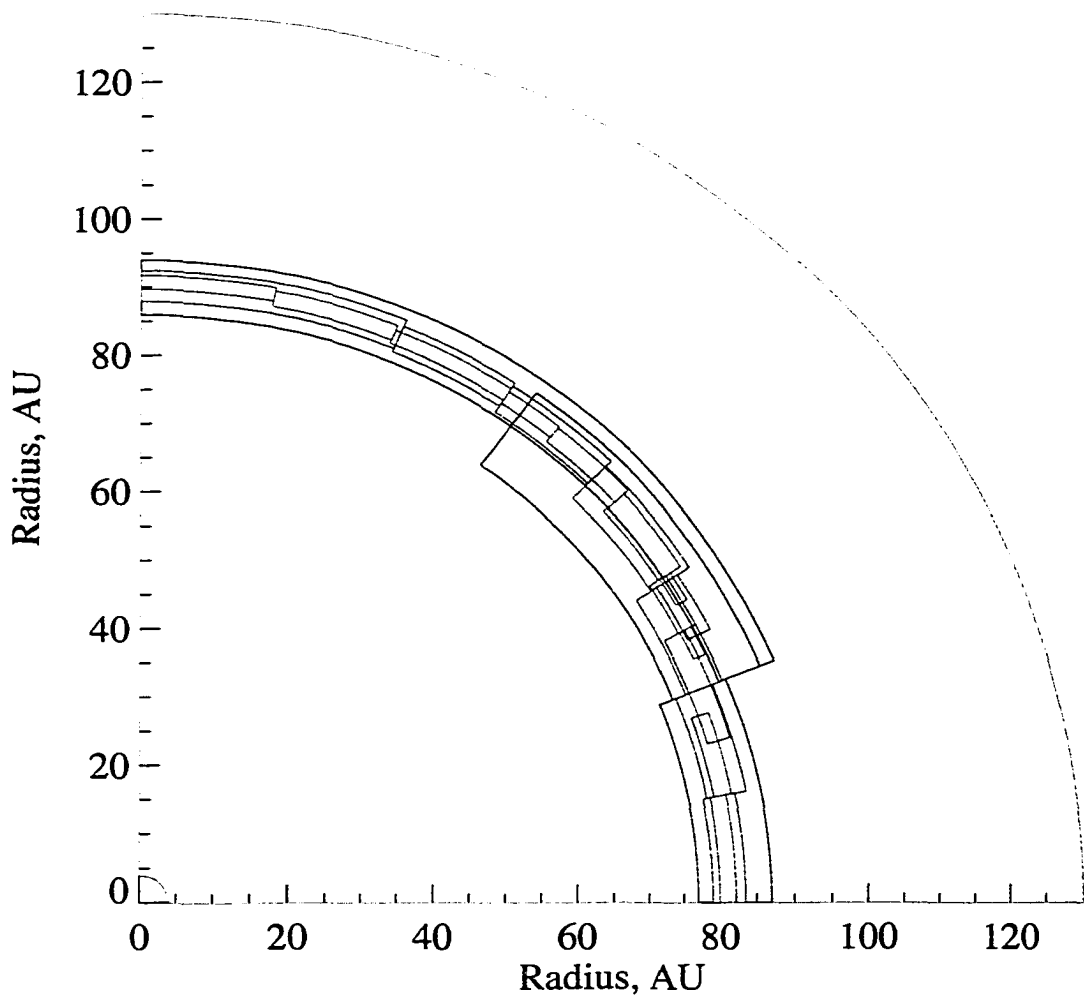


Figure 3.4 Grid structure for case I. A single level 0 grid is shown yellow, level 1 grids are blue, level 2 green and level 3 red.

3.6 Grid structure and the solar wind flow

We performed numerical simulations using a non-uniform wind model described in Sections 3.2 and 3.3 with a termination shock between 80 and 90 AU (case I) and 90 and 100 AU (case II). Both cases have $A > 0$ to allow comparison with the recent Voyager ACR data. The CR injection efficiency, η , was 1×10^{-4} and 3×10^{-4} for the two cases, respectively. The higher injection rate for a shock at larger heliospheric distance is required to conform with the measurements at 70 AU, due to additional modulation between the shock and the spacecraft. The computational domain spans the radial distance between 4 and 130 AU and latitude angle of 90° . The coarse grid resolution was 126 by 45 grid cells in r and θ , respectively, with 140 grid points in momentum space.

Figure 3.4 shows the complete grid structure with grids of different levels shown with different colors. Despite their small sizes, the finest (level 3) grids actually contain the most cells (about 10,000, vs. 5,000 for the single large level 0 grid). Because the finest grids must be updated 8 times as often as the coarsest, the bulk of the computer time is spent on the former.

The radial wind velocity contours for case I are shown in Fig. 3.5 (cf. Fig. 2.1). The upstream flow clearly shows a transition between the fast and slow wind at 30° latitude as well as deceleration due to pickup ions. The shock is elongated in the poleward direction. Unlike Fig. 2.1, the case without the ACRs is not shown here because the dynamical effects of the cosmic rays are too small (see below) and the non-radial flow is due mostly to the fact that the wind speed is no longer \perp to the surface of the shock. The exception is the polar region downstream of the shock, where the radial velocity falls off

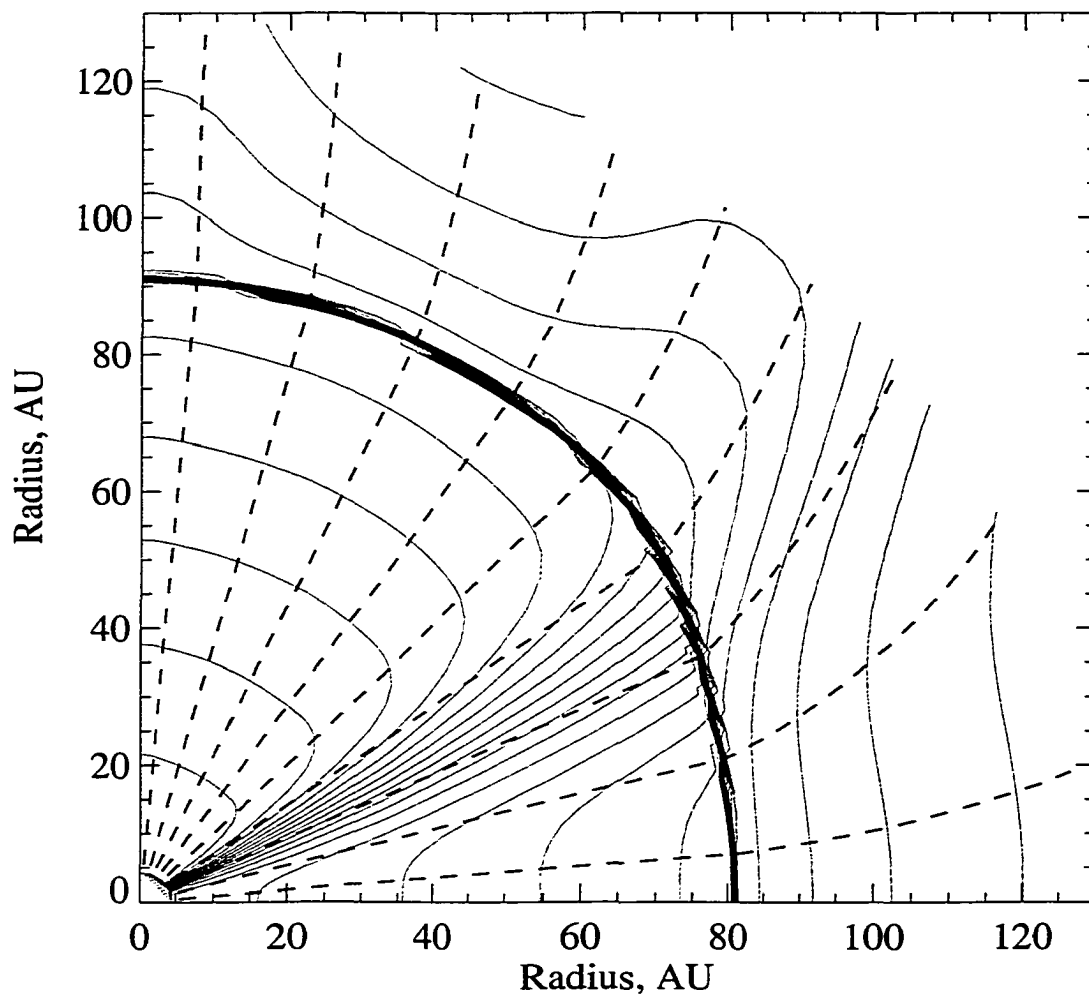


Figure 3.5 Radial solar wind velocity contours for case I (TS between 80 and 90 AU). The transition between the fast and the slow solar wind is clearly seen in the upstream region. The non-spherical wind flow downstream are due to TS asymmetry. Contours are evenly spaced at 2.5% increments between 0 and 750 km/s. Streamlines (dashed) turn towards high latitudes because of the obliquity of the shock.

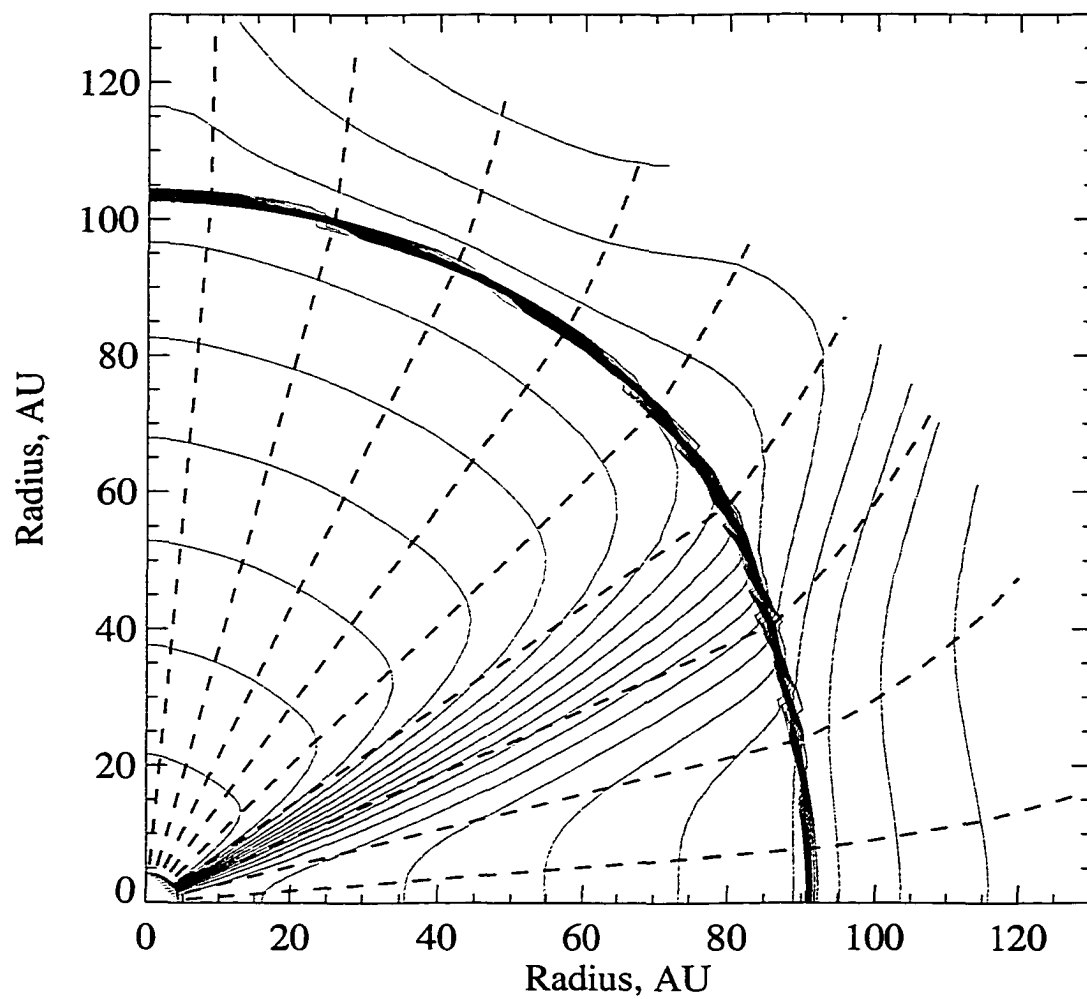


Figure 3.6 Same as Figure 3.5, but for case II (shock between 90 and 100 AU).

slower than r^{-2} , as in the case without the pickup ions. Radial wind velocity for case II is plotted in Fig. 3.6.

Figures 3.7 and 3.8 show radial profiles of the solar wind speed and gas+PUI pressure, as well as the pressure of the anomalous cosmic rays. The solar wind undergoes essentially linear deceleration in the supersonic region (Lee, 1997; Zank and Pauls, 1997) by the PUIs. By 80AU the SW flow slows down by 110km/s at 90° and by 90km/s at 0° . Because the Mach number in the hot PUI-SW mixture is not very high, the shock is relatively weak. The compression ratio varies between 3.2 and 3.3 between 0° and 90° latitude for case I and between 3.2 and 3.0 for case II when ACR dynamical effects are neglected. The total plasma (gas+PUI) pressure is falling off much more slowly than the $r^{-10/3}$ adiabatic law because of the high temperature of the pickup ions. The postshock flow is decelerating faster than the usual r^{-2} near the equator. This effect is different from that described in Section 2.7, and is due to the non-sphericity of the shock, which causes the streamlines to bend polewards after the discontinuity. The flow is thus expanding faster at low latitudes. The ACR pressure is quite small, even near the equator, where more particles are injected. The largest ACR pressure (near the shock) is $0.05\text{eV}/\text{cm}^3$ for case I and $0.12\text{eV}/\text{cm}^3$ for case II. These numbers are larger than those used by Fahr *et al.* (2000), but less than those obtained in le Roux and Fichtner (1997) from their high injection efficiency model. For all cases, the ACR pressure is less than 10% of the dominating pressure exerted by the plasma (whether dynamic or thermal).

The bottom panels on Figures 3.7 and 3.8 show magnified velocity profiles near the shock. The shock does move outward, as predicted by the theory (Ko and Webb, 1988;

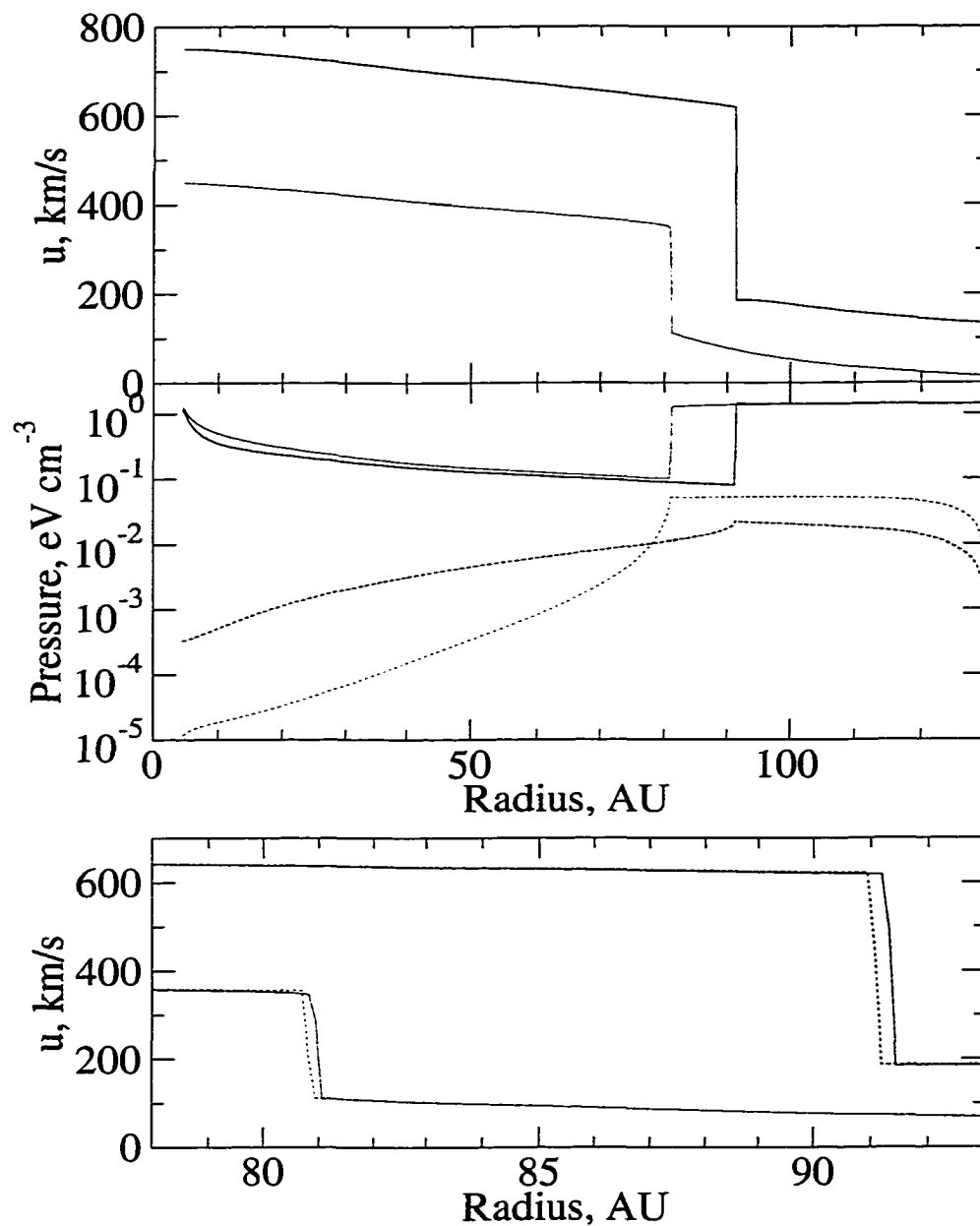


Figure 3.7 Top panel: radial SW velocity profiles at 0° (red) and 90° (blue) latitudes for case I. Middle panel: gas (solid lines) and ACR (dashed lines) pressures at 0° (red) and 90° (blue) latitudes. Bottom panel: expanded SW speed profiles near the shock (color as above). Solar wind speed without ACR pressure effects is shown with dashed lines.

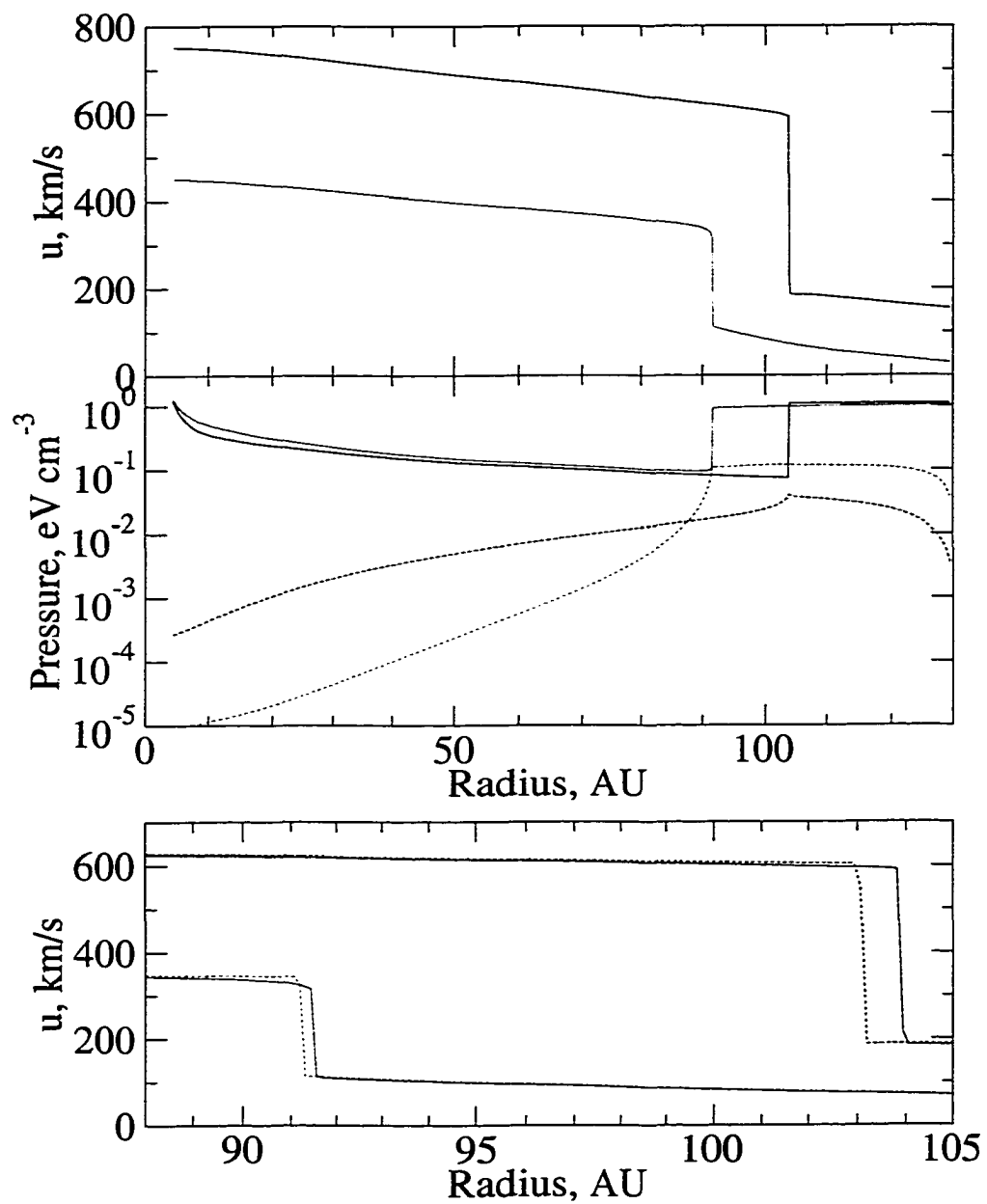


Figure 3.8 Same as Figure 3.7, but for case II. Notice the visible shock precursor in the bottom panel.

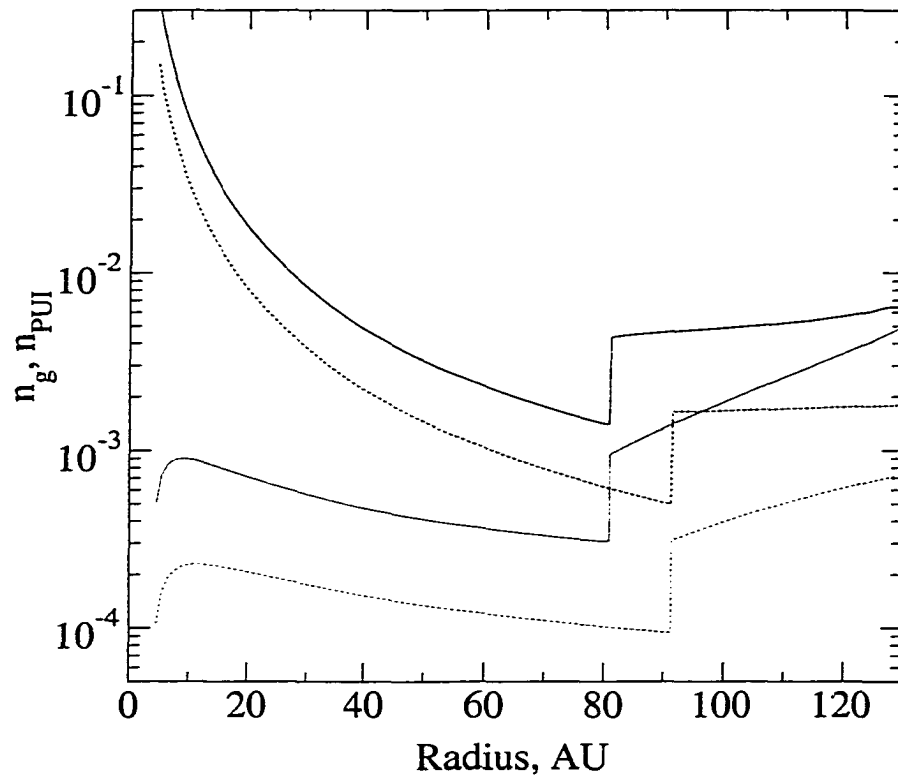


Figure 3.9 Solar wind proton density (blue) and pickup ion number density (red) for 0° (solid lines) and 90° (dashed lines) latitude.

Lee, 1997). However the magnitude of this shift is quite small (less than 1 AU). In the polar region, the shock moves farther away, despite the smaller ACR pressure. This is most likely caused by the fact that ∇P_c is much larger at the equator due to smaller diffusion and opposing drift, which slows down the wind and creates a precursor ~ 3 AU in size (the subshock compression ratio is reduced to 2.9). The situation near the equator is similar to the GCR case, discussed in Chapter 2.

The small increase in the ACR pressure downstream of the TS is due to the fact that u falls off faster than r^{-2} , so that $\nabla \cdot \mathbf{u} < 0$ in this region, causing some additional acceleration. Note that the subsonic downstream flow tends to be incompressible, and the radial slow-down (convergence) will tend to be compensated by the latitudinal expansion (divergence). The acceleration effect can easily be demonstrated by assuming that κ is small downstream and can be neglected. Then, the spherically-symmetric transport equation is simply

$$u \frac{\partial f}{\partial r} = \frac{1}{3} \frac{1}{r^2} \frac{\partial(r^2 u)}{\partial r} \frac{\partial f}{\partial \ln p}. \quad (3.27)$$

With $u = u_{sh}(r_{sh}/r)^\alpha$, where u_{sh} is the wind speed just downstream of the shock, (3.27) can be written as an advection equation in phase space:

$$\frac{\partial f}{\partial \ln r} + \frac{(\alpha-2)}{3} \frac{\partial f}{\partial \ln p} = 0. \quad (3.28)$$

This equation means that f and therefore P_c can increase with distance if $\alpha > 2$. This is what Figs. (3.7) and (3.8) demonstrate for the equatorial case (in the polar regions, diffusion is larger and Eq. 3.28 does not apply).

The solar wind and the pickup ion number densities are shown in Figure 3.9. Most

PUIs are produced in the inner heliosphere (where the optical depth for the hydrogen atoms becomes ~ 1 ; see Eq. 3.11), but their production elsewhere is responsible for the slower than r^{-2} radial falloff (*Vasyliunas and Siscoe, 1976; Isenberg, 1986*) and the enhancement downstream of the shock.

3.7 Anomalous cosmic-ray distribution and spectra

The two-dimensional maps of the 10 MeV ACRs are shown in Figures 3.10 and 3.11 for the cases I and II, respectively. The maximum at low latitudes occurs in the region of the highest injection rate (because of the higher PUI flux). The maximum is actually some distance downstream of the shock, due to post-acceleration (see previous section). The second maximum is at higher latitudes and is most likely caused by the particles gaining energy by drifting along the shock face, as explained in Section 1.2. The location of this maximum agrees with the 2-dimensional calculations of *Jokipii (1986)* for the $A > 0$ case.

The ACR spectra are plotted in Figures 3.12 and 3.13 for 30° latitude. Voyager 1 and 2 measured spectra are shown for comparison (in 1998, Voyager 1 was at about 70 AU while Voyager 2 was at 55 AU heliospheric distance). As in the previous chapter, we put less emphasis on fitting the observations, than on the physics of the problem. The computed ACR gradients are larger than observed with the current diffusion model, as was noted by *le Roux et al. (1999)*. Still, spectra calculated are in a reasonable agreement with the observations (better fits are achieved in modulation models, see, e.g., *Steenberg,*

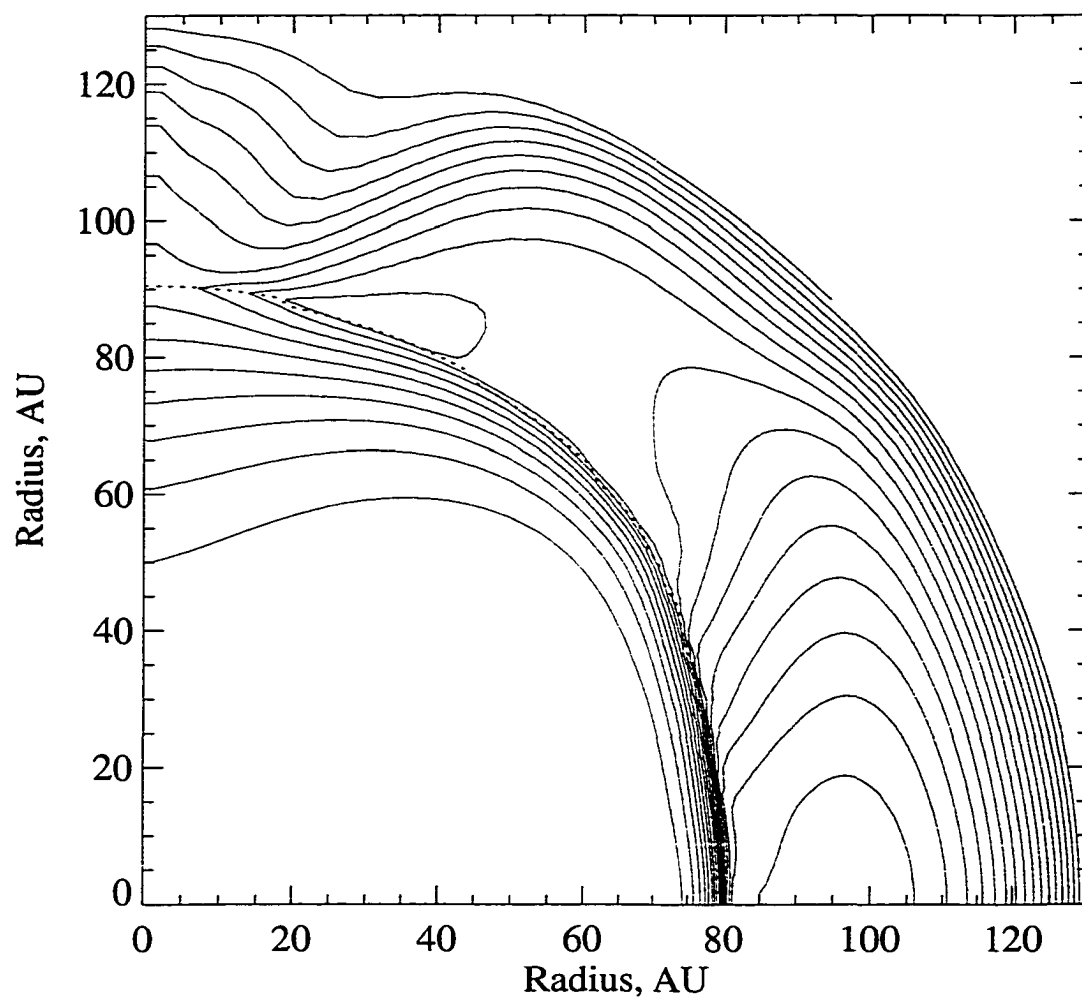


Figure 3.10 10 MeV ACR intensity profiles for case I. The contours are evenly spaced at 5% increments. The position of the TS is shown with a dotted line. The presence of the two maxima is explained in the text.

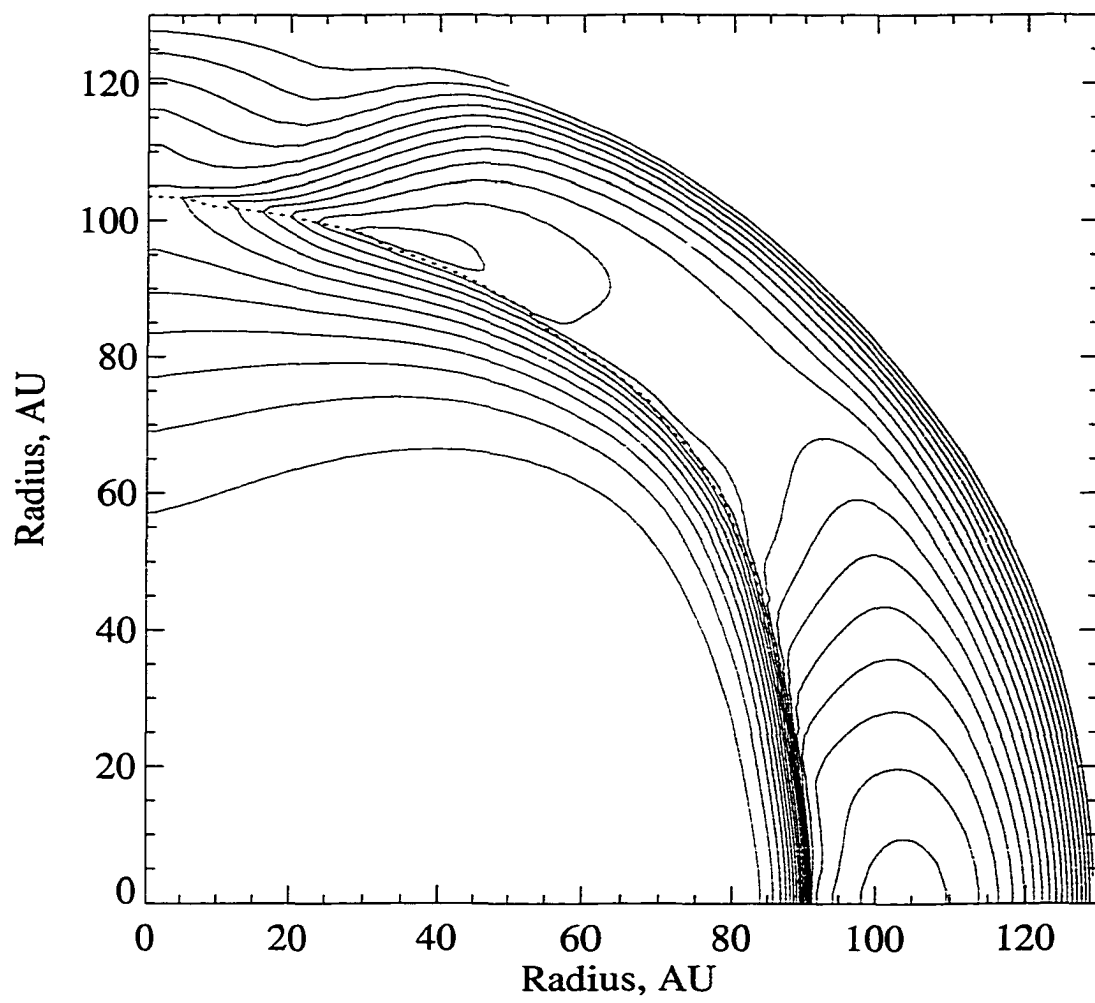


Figure 3.11 Same as Figure 3.10, but for case II.

et al., 1999, but require rather strong assumptions about the diffusion coefficient). Part of the discrepancy can be explained by the fact that Voyagers 1 and 2 are in different hemispheres and by the additional ACR travel time between the two spacecraft. Spectral maxima are located at ~ 30 MeV in both cases, in agreement with the data. The low-energy spectra have the expected $J \sim T$ dependence at small r (see Section 1.1). The spectral slope is approximately -1.2 for case I and -1.35 for case II (all at 30° latitude), which is consistent with the shock compression ratios reported in the previous section.

When comparing Figures 3.12 and 3.13, a feature is seen in the ACR spectra at the shock at several tens of MeV. This enhancement or bump, is visible in case I, and is much smaller in case II. Figure 3.14 shows an enlarged portion of the spectra at the shock below the cutoff for case I. Note that the bump is present only at mid-latitudes. While it is tempting to ascribe this to drift effects, further tests with drifts excluded didn't eliminate the bump. It is difficult to say what causes the bump. Because it occurs predominantly in the region of transition between the slow and the fast wind, shock geometry may have this effect on the spectra. We also found that a similar bump occurs in a 1-dimensional (spherically-symmetric) case. Appendix B discusses in some detail the conditions required for the bump to occur in the 1-D case. The height of the 1-D bump can be controlled by varying the downstream diffusion coefficient as well as moving the outer boundary. The ratio κ_2/κ_1 up- and downstream for high-energy particles is $\sim (B_1/B_2)^2$, which is close to $1/10$. In case II, the distance between the shock and the outer boundary is smaller and the bump is less pronounced (the ACRs are accelerated to slightly higher cutoff energy in case I because fewer particles are escaping

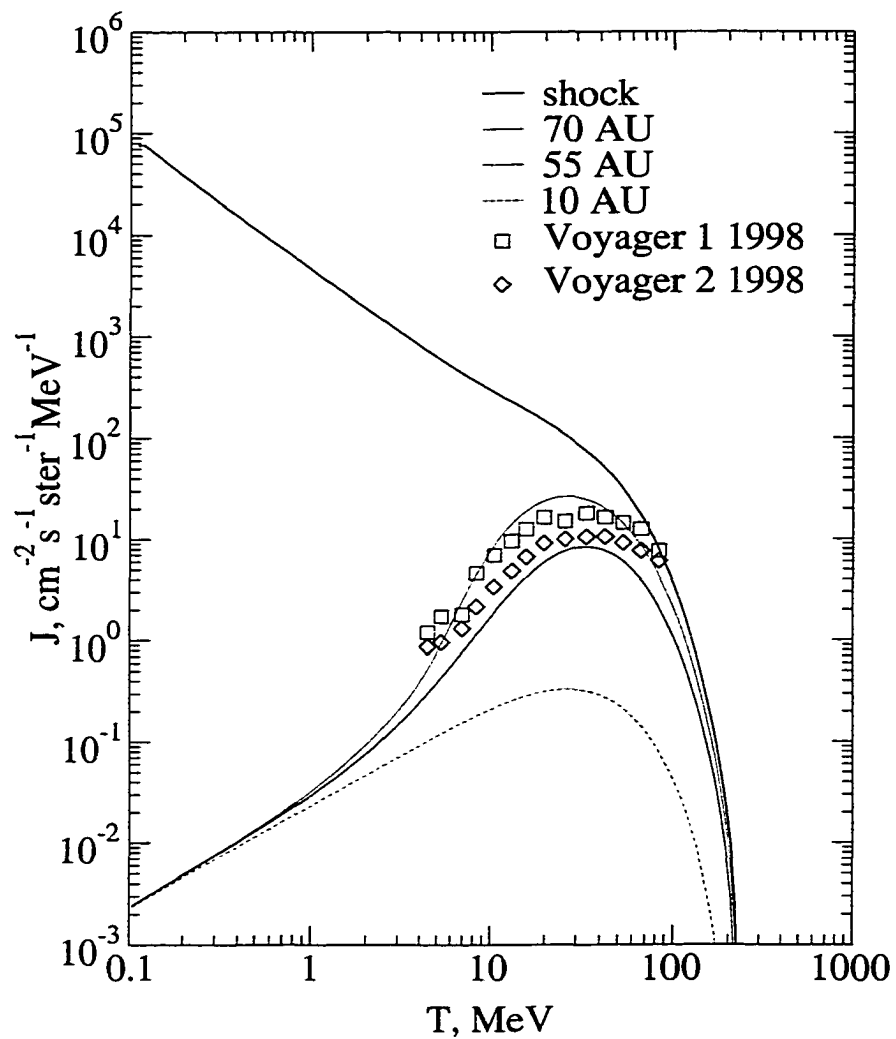


Figure 3.12 Computed ACR spectra for case I at 30° latitude. The Voyager 1 and 2 measured spectra (from *Stone et al.*, 1999) are shown for reference. In 1998, Voyager 1 was at 70 AU and 34° north while Voyager 2 was at 55 AU and 23° south latitude.

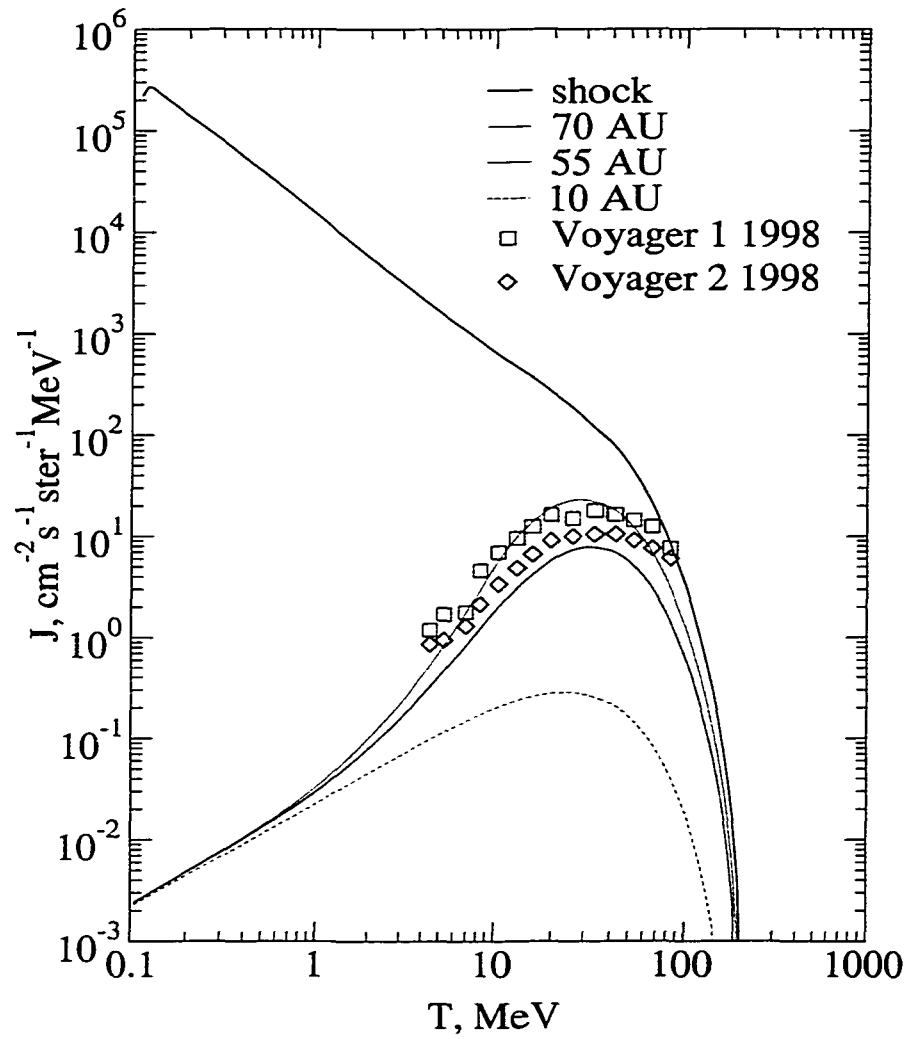


Figure 3.13 Same as in Figure 3.12, but for case II. Notice that the shock spectrum is softer due to a smaller subshock compression ratio.

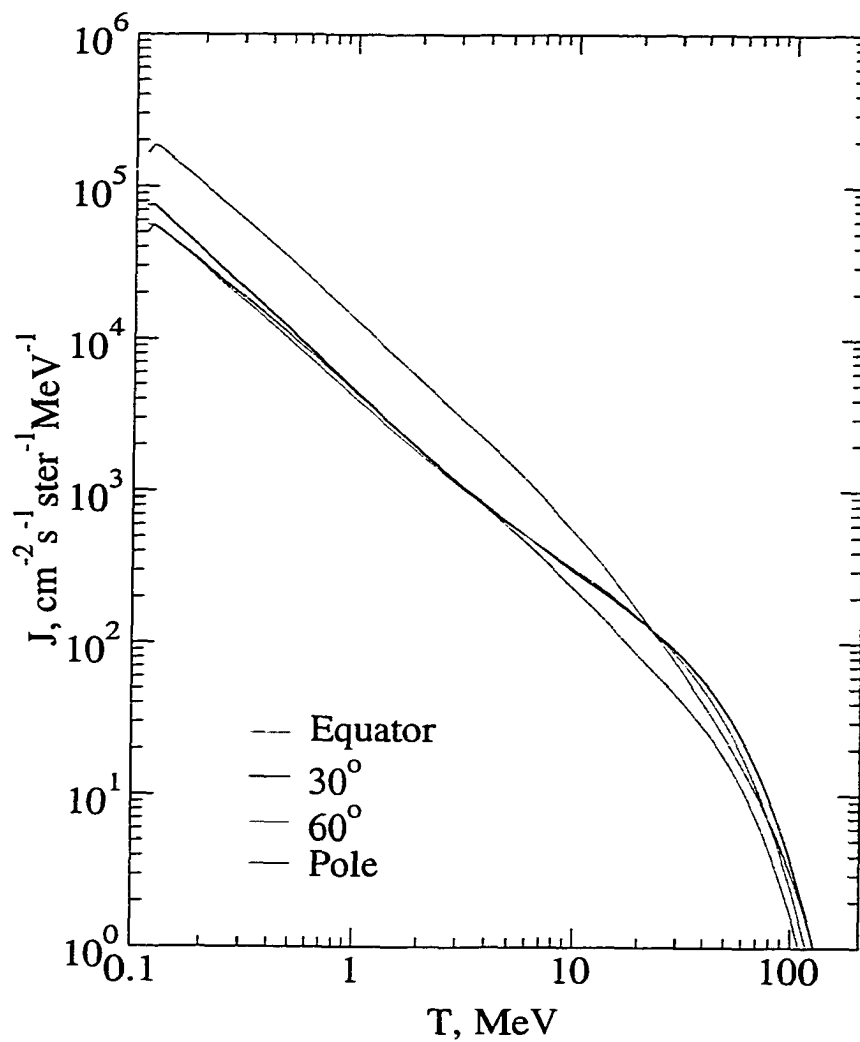


Figure 3.14 Magnified ACR spectra before the cutoff for case I for four different latitudes at the shock. The "bump" (see text) is clearly seen at mid-latitudes.

through the modulation boundary). The spectra are harder for case I because the shock compression ratio is greater (3.2 vs. 2.9).

3.8 Discussion

The model described in this chapter is a significant improvement over the GCR model described in Chapter 2 and is an important step in the direction of building a global model of the heliosphere. By using an adaptive mesh we are able to properly study the acceleration and propagation of the anomalous cosmic rays with small diffusive scales and their effects on the solar wind. The major finding is that the ACRs have little, if any, dynamical effect on the wind because their pressure must be small (as constrained by the spectra observed). A somewhat higher P_c is possible if the shock is located between 90 and 100AU, in which case there is a precursor to the shock. The notion of small P_c is consistent with the work of *Fahr et al.* (2000), but we are actually able to justify this notion with our model.

There are no visible latitudinal effects due to ACRs. Pickup ions do influence the wind upstream of the shock, reducing its ram pressure. Compared with the no-PUI case, the shock distance is reduced by 15AU (the no-PUI shock distance was computed using Eq. 2.12 with data from Table 3.1). The only visible latitudinal PUI effect is the increase in the wind speed over the poles.

While the lower ACR momentum boundary of 100keV, used in our simulations, is considerably higher than that in *le Roux and Fichtner* (1997), it is unlikely that including

lower-energy particles in the transport equation would have had much effect on the shock. Indeed, all particle spectra we obtained give harder than p^{-5} power-law dependence of the PSD, meaning most energy is contained in the region of the cutoff (it is trivial to show that at low energies $d\ln E_c/d\ln p \sim fp^{-5}$, see Eq. 1.20). Additionally, particles with energies between 1 and 10keV cannot be described by the diffusion-convection equation. They would, in fact, only affect the injection process.

Our simulation support the idea that the maximum energy attained by ACRs at the termination shock is determined by one-dimensional factors, such as the upstream shock parameter, κ/ur , and the distance to the outer boundary. Shock drift apparently plays only a minor role in the acceleration process, at least for the diffusion parameters we used. The second maximum in Figures 3.10 and 3.11 is weak compared to the primary maximum at low latitudes, because drift acceleration does not offset the decrease in source strength towards the polar region.

The one-dimensional spectral enhancement, described in the previous section, is apparently a new effect, essentially overlooked by previous research (although, a similar "bump" can be seen in several other numerical models, such as *Potgieter and Moraal, 1988*). There is a similar feature 2-D simulations of *Jokipii, 1997*, although in their case the bump was attributed to drift effects. We offer a tentative explanation for this phenomenon in Appendix B. An analytic solution would help understand it better, but obtaining a complete solution upstream of the shock for a momentum-dependent κ and with cooling included is extremely difficult (the work of *Webb et al. 1985*, which we mentioned several times before, addressed the simpler case when κ is independent of

energy; even so, their solution is still very complicated). Additional research will be needed to study this effect in more detail.

Conclusion: We have shown that anomalous cosmic rays modify the wind very slightly. Particle acceleration is similar to a spherically-symmetric case, and shock drifts do not produce visible change in the spectra. The spectral bump, seen at some latitudes, is a combination of 1-dimensional effects and shock geometry. Its physical meaning is not clear at this point and requires further investigation.

CONCLUSIONS AND FUTURE WORK

Cosmic rays are an important constituent of the interplanetary matter. These particles exert a pressure that is, in some cases, comparable to the dynamic and thermal pressures of the solar wind plasma. Large cosmic-ray pressure gradients can significantly change the plasma flow patterns in the heliosphere.

This possibility has been studied in this work by developing a 2-dimensional, time-dependent heliospheric model. The cosmic rays were incorporated self-consistently, so that their energy was included in the total energy of the system. Unlike most previous models, we used a kinetic description for the energetic particles. Transport coefficients were computed in a consistent fashion, using very general expressions for diffusion coefficients and drift velocities. Magnetic field was also included in the simulation, although not self-consistently. In this work, we for the first time computed the modified polar field for arbitrary solar wind flows. Our numerical model features a second-order wave propagation solar-wind solver, a fully-implicit second-order cosmic-ray solver, and uses an adaptive mesh algorithm to improve resolution in the shock vicinity.

Based on the results obtained, the following conclusions may be drawn:

- 1) Both galactic and anomalous cosmic rays have a dynamic effect on the solar wind flow. GCRs affect the wind substantially, while the ACR effects are small.
- 2) GCRs deflect the solar wind towards the ecliptic plane downstream of the shock. This effect is caused latitudinal GCR gradients, which, in turn, are due to variation with latitude of the radial drift velocity.
- 3) The termination shock moves inward by 3–4AU under the influence of the GCRs

and less than 1AU outward due to ACR pressure gradient.

- 4) The subshock compression ratio changes very little (by 0.1–0.2) in all cases.
- 5) ACR acceleration follows a 1–dimensional pattern. Shock drift effects are overshadowed by the latitudinal variations in the source strength.
- 6) A "bump" is visible in ACR spectra at mid–latitudes. We attribute this phenomenon to 1–dimensional effects as well as the shock geometry, rather than the shock drift.
- 7) Particle spectra are, in general, consistent with both ACR and GCR observations.

Cosmic–ray and pickup ion effects on the wind are compared in Table C.1, where P_{up} is the pressure of the species just upstream of the shock. The last column is the change in the subshock compression ratio.

Table C.1 A comparison of the dynamical effects of the various particle species.

	P_{up} , eV/cm ³	Δr_{sh} , AU	$\Delta(u_1/u_2)$
GCR	0.4	–3.5	0.2
ACR	0.1	0.3	0.1
PUI	0.1	–15	1.0

As far as the future of the model is concerned, its current physical framework and the AMR numerical code can be used to build global heliospheric models. The following is a summary of improvements we will be focusing on in the future:

- 1) The simulation domain should be extended to include the region outside the heliopause and the LISM. This, most likely, will require a 3–dimensional model if we want to retain the latitudinal effects caused by the solar magnetic field. This move will require massive computer power, but such power is within the limits of current supercomputers. Similar 3–D simulations (without cosmic rays) have been

available for several years now (*Pauls and Zank, 1996; Linde et al., 1998*).

- 2) We should ultimately move to the full MHD description of the plasma (the magnetic field is dynamically important near the heliopause; see *Nerney et al., 1993*). This will require a new Riemann solver because of an increased number of degrees of freedom and or wave modes. A bibliography on MHD Riemann solvers can be found in *Le Veque (1997)*.
- 3) A more accurate pickup ion model may be needed, and the neutral hydrogen must be included as a separate population, either as a fluid (*Pauls et al., 1995*) or kinetically (*Baranov and Malama, 1993*). The latter is a requirement to properly model the "hydrogen wall". Availability of the computed PUI velocity distribution may help solve the injection problem, described in Section 1.2.
- 4) The numerical code may need to be revised in the future, especially if a 3-D model is attempted. As was mentioned before, the cosmic-ray code is not very efficient at this point (i.e., requires a small time step). It is possible that some benefits can be gained by more accurately computing numerical fluxes at grid interfaces (*Johansen and Colella, 1998*).
- 5) Finally, it would be interesting to apply the current model to other particle species, such as He and heavier nuclei in anomalous CRs. While the latter would almost certainly have no effect on the solar wind, a model with self-consistently computed plasma flow patterns and diffusion coefficients would be a big improvement over the modulation models.

APPENDIX A

3-FLUID PUI-SOLAR WIND EQUATIONS

In this Appendix, we shall briefly derive a set of fluid equations for the three components of the solar wind plasma: protons (p), electrons (e) and PUI (i) with an additional notation (H) for neutral hydrogen. All derivations are valid for the supersonic regime only (upstream region), which assumes that $\rho u^2 \gg nkT$ and $u^H \ll u$. For the pickup ions, we assume that the distribution function is characterized by an effective temperature which is of the order of $m_p u^2/2k$ (k is the Boltzmann constant). The moment equations for any plasma component (a) can be found in *Burgers* (1969), Chapters 12 and 13 (see also *Braginskii*, 1965). These can be written as follows, assuming isotropic temperatures: mass conservation:

$$\frac{\partial}{\partial t}(n^a m^a) + \frac{\partial}{\partial x_i}(n^a m^a u_i^a) = Q^{n,a}, \quad (\text{A.1})$$

momentum conservation:

$$\begin{aligned} & \frac{\partial}{\partial t}(n^a m^a u_i^a) + \frac{\partial}{\partial x_i}(n^a m^a u_i^a u_j^a + n^a kT^a \delta_{ij} + P_{ij}^a) - n^a e^a \left(E_i + \epsilon_{ijk} \frac{u_j^a}{c} B_k \right) \\ & = \sum_b n^a \mu^{ab} \nu^{ab} (u_i^b - u_i^a) + \frac{3}{5} \sum_b \frac{\mu^{ab} \nu^{ab}}{k n^b} \frac{m^b n^b q^a - m^a n^a q^b}{m^a T^b + m^b T^a} + Q_i^{u,a}, \end{aligned} \quad (\text{A.2})$$

total energy conservation:

$$\begin{aligned} & \frac{\partial}{\partial t} \left(\frac{n^a m^a (u^a)^2}{2} + \frac{3}{2} n^a kT^a \right) + \frac{\partial}{\partial x_i} \left[u_i \left(\frac{n^a m^a (u^a)^2}{2} + \frac{5}{2} n^a kT^a \right) + P_{ij}^a u_j^a + q_i^a \right] \\ & - n^a e^a u_i^a E_i = 3 \sum_b n^a \mu^{ab} \nu^{ab} \frac{k(T^b - T^a)}{m^a + m^b} + Q^{e,a}. \end{aligned} \quad (\text{A.3})$$

In these equations, P_{ij} is the viscous stress tensor, q is the heat flux, $m^{ab} = m^a m^b / (m^a + m^b)$

is the reduced mass, and ν^{ab} is the collision frequency between species for momentum exchange. The Q terms describe charge exchange with the neutrals and will be written in explicit form for each species below.

The mass conservation equations are written immediately:

$$\frac{\partial}{\partial t}(n^p m^p) + \frac{\partial}{\partial x_i}(n^p m^p u) = -n^p m^p \nu^{pH} \quad (\text{A.4})$$

$$\frac{\partial}{\partial t}(n^i m^p) + \frac{\partial}{\partial x_i}(n^i m^p u) = n^p m^p \nu^{pH}, \quad (\text{A.5})$$

where ν^{pH} is the charge exchange frequency (*Holzer, 1972; McNutt et al., 1998*).

To estimate the importance of various terms in (A.1)–(A.3), we note that in the solar wind, in general, $n^e \simeq n^p$, while $n^i \sim 0.1n^e$ and $T^i \sim 1.5 \times 10^7 \text{K} \gg T^e, T^p$. In the inner heliosphere $m^e T^i \ll m^p T^e$, while the opposite is true beyond several tens of AU. The collision frequency is (*Spitzer, 1962, p. 135; Burgers, 1969, p. 164*):

$$\nu^{ab} = \frac{4\sqrt{2}\pi}{3} \frac{e^4 n^b}{k^{3/2} (\mu^{ab})^{1/2}} \left(\frac{m^a + m^b}{m^b T^a + m^a T^b} \right)^{3/2} \ln \Lambda, \quad (\text{A.6})$$

where Λ is the Coulomb logarithm. Both ν^{ee} and ν^{pp} are approximately independent of radius because $n \sim T^{3/2}$ in a polytropic wind. These have to be compared with cyclotron frequencies $\omega_g = eB/mc$. The results are as follows, for a typical $r = 10$ AU:

$$\nu^{ee} \sim \nu^{ep} = 6 \times 10^{-6} \text{s}^{-1}, \quad \nu^{pp} = 10^{-7} \text{s}^{-1}, \quad \nu^{ei} = 2 \times 10^{-6} \text{s}^{-1}$$

$$\omega_g^e = 300 \text{s}^{-1}, \quad \omega_g^p = \omega_g^i = 0.2 \text{s}^{-1}.$$

In view of small collision frequencies compared with the gyrofrequencies, transport coefficients P_{ij} and q in the direction perpendicular to the mean magnetic field will be

determined by the magnetic field alone, rather than by collisions, with cyclotron radius acting as a mean free path. In particular, the heat flux is found from Eq. (12.9) of *Burgers* (1969) as

$$\frac{5}{2} n^a k^2 T^a \frac{\partial T^a}{\partial x_i} = e^a \epsilon_{ijk} \frac{q_j}{c} B_k \quad (\text{A.7})$$

The magnitude of the heat flux is estimated as $q \sim nk^2 T^2 c / (eBL)$, where $L \sim r$ is the characteristic length scale of the system. This has to be compared with $nkTu$, the advective thermal energy flux. The results for 10 AU solar distance are as follows:

$$q^e \sim q^p = 10^{-14} \text{erg cm}^{-2} \text{ s}^{-1}, \quad q^i = 3 \times 10^{-9} \text{erg cm}^{-2} \text{ s}^{-1}$$

$$n^e k T^e u^e \sim n^p k T^p u^p = 3 \times 10^{-9} \text{erg cm}^{-2} \text{ s}^{-1}, \quad n^i k T^i u^i = 5 \times 10^{-4} \text{erg cm}^{-2} \text{ s}^{-1}.$$

Again, the heat fluxes are much smaller than the advective fluxes and can be neglected in (A.3) and the thermal force (second term on the right in A.2) can also be omitted. Estimates similar to those above also show that the viscous stresses are very small as well, i.e., $P_{ij} \ll nkT$.

The heat exchange terms on the right hand side of (A.3) can be neglected in the proton and PUI equations because the effective frequency for energy exchange, $m^e/m^p v^{ee}$, is small compared with the inverse dynamic time scale, u/L , but should probably be retained in the electron energy equation (the collisional PUI heating of the electron component is the most efficient in this case).

The bulk speed difference $\Delta \mathbf{u} = \mathbf{u}^a - \mathbf{u}^b$ creates the electric current necessary to support the magnetic field \mathbf{B} . This can be estimated from the Maxwell's law using the expression for the current $\mathbf{j} \sim ne\Delta \mathbf{u}$, to obtain

$$\Delta \mathbf{u} \simeq \frac{c \nabla \times \mathbf{B}}{4 \pi n e}. \quad (\text{A.8})$$

From an order of magnitude estimate, this is a few cm/s. Taking $\mathbf{u}^i \simeq \mathbf{u}^p = \mathbf{u}$ and $\Delta \mathbf{u} = \mathbf{u}^e - \mathbf{u}$, the total current \mathbf{j} is as above. When momentum equations (A.2) are added together, collisional terms cancel and with $n^e = n^p + n^i$ and neglecting terms containing m^e , we obtain

$$\begin{aligned} \frac{\partial}{\partial t} (n^e m^p u_i) + \frac{\partial}{\partial x_i} (n^e m^p u_i u_j + P^i) + \frac{1}{c} \epsilon_{ijk} j_j B_k \\ = m^p (n^p \nu^{pH} + n^i \nu^{iH}) (u_i^H - u_i), \end{aligned} \quad (\text{A.9})$$

where $P^i = n^i k T^i$ and ν^{iH} is the charge exchange frequency for the PUIs.

When writing separate energy equations for the SW protons and the PUIs, we must take into account the energy spent on accelerating the PUIs to the solar wind speed while simultaneously increasing their thermal energy. Equations (A.3) can be somewhat simplified if $T^e \simeq T^p$ (while this is not true in general, this approximation does not introduce problems in the supersonic region, where proton and electron pressures are small anyway). We can now add the electron energy equation, multiplied by n^p/n^e , to the proton equation, and in a similar way, to the PUI equation. The results are as follows:

$$\begin{aligned} \frac{\partial}{\partial t} \left(\frac{n^p m^p u^2}{2} + 3P^p \right) + \frac{\partial}{\partial x_i} \left[u_i \left(\frac{n^p m^p u^2}{2} + 5P^p \right) \right] - P^p u_i \left(\frac{1}{n^p} \frac{\partial n^p}{\partial x_i} - \frac{1}{n^e} \frac{\partial n^e}{\partial x_i} \right) \\ - \frac{n^p}{n^e} j_i E_i = -\nu^{pH} \left(\frac{n^p m^p u^2}{2} + 3P^p \right) - \nu^{pH} n^p \left(\frac{m^p (u^2 - (u^H)^2)}{2} + \frac{m^p (u_i - u_i^H)^2}{2} \right) \end{aligned} \quad (\text{A.10})$$

$$\begin{aligned}
& \frac{\partial}{\partial t} \left(\frac{n^i m^p u^2}{2} + \frac{3}{2} P^i \right) + \frac{\partial}{\partial x_i} \left[u_i \left(\frac{n^i m^p u^2}{2} + \frac{5}{2} P^i \right) \right] - \frac{n^i}{n^e} j_i E_i \\
& = -v^{iH} n^i \left[\frac{m^p (u^2 - (u^H)^2)}{2} + \frac{3}{2} \frac{P^i}{n^i} - \frac{3}{2} kT^H \right] \\
& + v^{pH} n^p \left[\frac{m^p u^2}{2} + \frac{m^p (u_i - u_i^H)^2}{2} + \frac{3}{2} kT^H \right].
\end{aligned} \tag{A.11}$$

In deriving Eq. (A.10) we assumed that the "pickup energy" comes from the solar wind and the PUI components according to their charge exchange rates. The extra term in the SW equation comes from using (A.4) for $\partial n^p / \partial t$; this term is absent in (A.11) because $P^i \gg P^p$. The electric field, E , on the right hand side can be expressed through u , B , and j using a generalized Ohm's law (see e.g., *Sturrock*, 1994, p 174), the most commonly used form of which is simply $j = \sigma(E + 1/cu \times B)$, where σ is the conductivity. The charge exchange frequency may actually be different for momentum and energy exchange so that v^{pH} and v^{iH} in (A.9) are not the same as in (A.10) and (A.11). Note also that if $n^i \ll n^p$, Eqs. (A.10) and (A.11) can be added together to obtain a single-fluid equation, similar to (3.4) with the source term (3.6).

Fluid equations in the downstream region can be written in a similar fashion. However it is more difficult to justify the assumption that $T^e \simeq T^p$ in this case because the thermal energy of the SW protons and electrons dominates the energy of the system and their difference can be significant. In general, Eq. (A.9) will have total pressure $P^p + P^e + P^i$ instead of P^i , while Eq. (A.11) will have extra terms proportional to P^e .

APPENDIX B

SPECTRAL "BUMP" IN SPHERICALLY–SYMMETRIC GEOMETRY

As described in Section 3.6, anomalous CR spectra show an enhancement (bump) at an energy of several tens of MeV, just before the cutoff. Similar features were seen in the simulation by *Jokipii* (1997), where they were attributed to drift effects. In our case, however, we found that the bump was present in 1–dimensional simulations as well. It follows then that the bump is either a numerical artifact, or a new feature of spherically–symmetric shock spectra. In Figure 3.14, this effect is most prominent for certain values of the diffusion coefficient κ_{rr} (or more precisely, the ratio κ_{rr}/ur_{sh}), typical for the heliosphere at mid–latitudes in the framework of the diffusion model described in Section 3.3.

To verify that the bump is not an artifact of the finite difference scheme used we solved the spherically–symmetric transport equation with a variety of phase space resolutions and solution methods. The transport equation (1.1) can be written in two different ways. The first is similar to (2.25) with the injection term (3.20):

$$\frac{\partial f}{\partial t} + \left(u - \frac{\partial \kappa_{rr}}{\partial r} - \frac{2\kappa_{rr}}{r} \right) \frac{\partial f}{\partial r} - \kappa_{rr} \frac{\partial^2 f}{\partial r^2} = \frac{1}{3} \left(\frac{\partial u}{\partial r} + \frac{2u}{r} \right) \frac{\partial f}{\partial \ln p} + Q_{inj}. \quad (\text{B.1})$$

Alternatively, Eq. (1.1) can be written in the spherically–symmetric case with $g=fr^2$ as

$$\frac{\partial g}{\partial t} + \frac{\partial}{\partial r} \left[g \left(u + \frac{\partial \kappa_{rr}}{\partial r} + \frac{2\kappa_{rr}}{r} \right) \right] - \frac{\partial^2 (g\kappa_{rr})}{\partial r^2} = \left(\frac{\partial u}{\partial r} + \frac{2u}{r} \right) \left(\frac{1}{3} \frac{\partial g}{\partial \ln p} + g \right) + Q_{inj} r_{sh}^2 \quad (\text{B.2})$$

We should note here that Eq. (B.2) should not be used in the numerical solution if κ_{rr} undergoes a jump at the shock (this is usually the case), because it contains the second

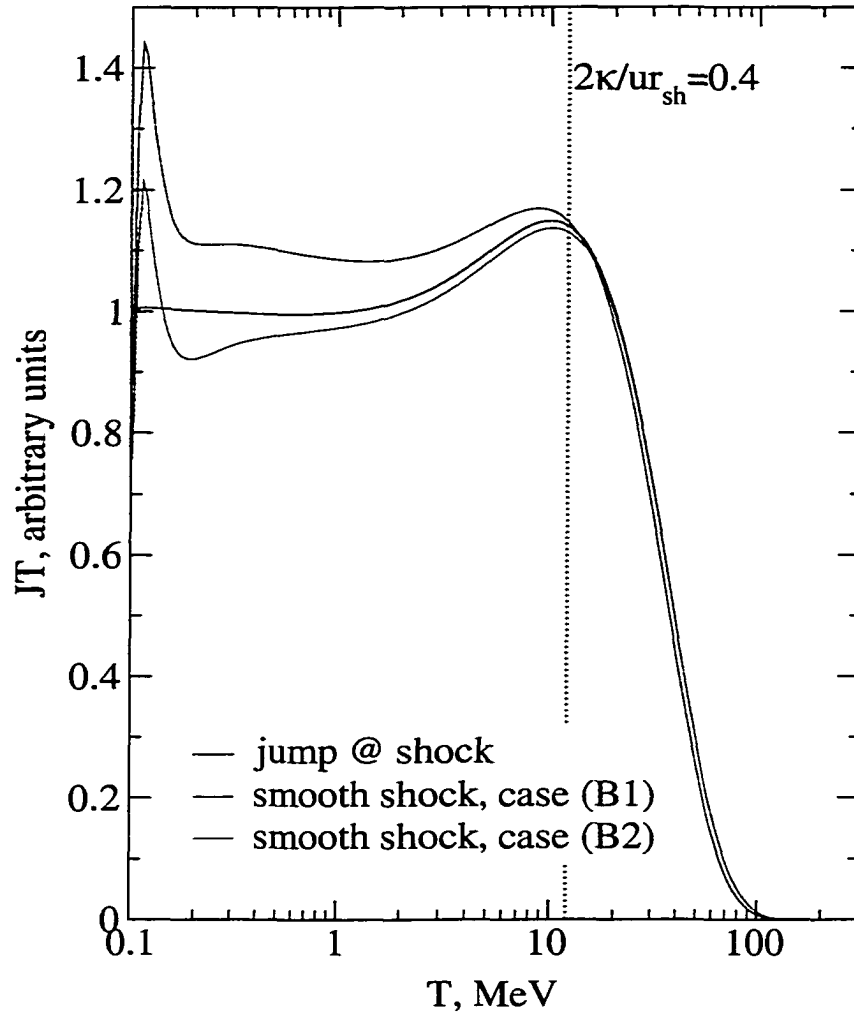


Figure B.1 Particle spectra resulting from solving Equations (B.1) and (B.2) with both a jump in the transport coefficients (κ , ν) and a smooth shock. The dotted line corresponds to the energy where the upstream shock parameter is equal to 0.4 (see text).

derivative of the diffusion coefficient. The numerical algorithm therefore contains two extremely large coefficients with the first and second derivatives in f , which must be subtracted to almost cancel each other – a situation that should be avoided at all costs to avoid rounding errors. Therefore we solved (B.2) using a smooth shock spread over at least 10–15 grid points. To achieve this, the radial resolution had to be increased by an order of magnitude. For Eq. (B.1) we used both jump and smooth shock conditions. For simplicity, diffusion coefficient was taken to be $\kappa_r = \kappa_0 (p/m_p c)^2$ with $\kappa_0 = 3.75 \times 10^{23}$ cm²/s upstream of the shock and 4.70×10^{23} cm²/s downstream. Equations (B.1) and (B.2) were solved using a 1–dimensional implicit scheme which is a simplified version of the 2–D scheme described in Section 2.6 with a prescribed wind velocity (400 km/s upstream, $100(r_{sh}/r)^2$ km/s downstream).

Results of these tests are shown in Figure B.1. The quantity that is plotted is intensity (J), multiplied by the kinetic energy T . For an ideal strong shock, $f \sim p^{-4}$, so that $JT \sim \text{const}$ at non–relativistic energies. There are some discrepancies between the models at the lowest energies, where the diffusive length is too small for the particles to "see" the entire smooth shock structure. However, all three models show the bump at the same energy and of the same magnitude. The bump is, in fact, unaffected by the change in either spatial or momentum resolution.

We have also performed tests using an alternative solution method of *Potgieter and Moraal* (1988). The idea is to replace the shock with a boundary condition, derived from the solution of the transport equation in the downstream region (the latter is easy to obtain because there is no cooling downstream). These tests were performed for the case

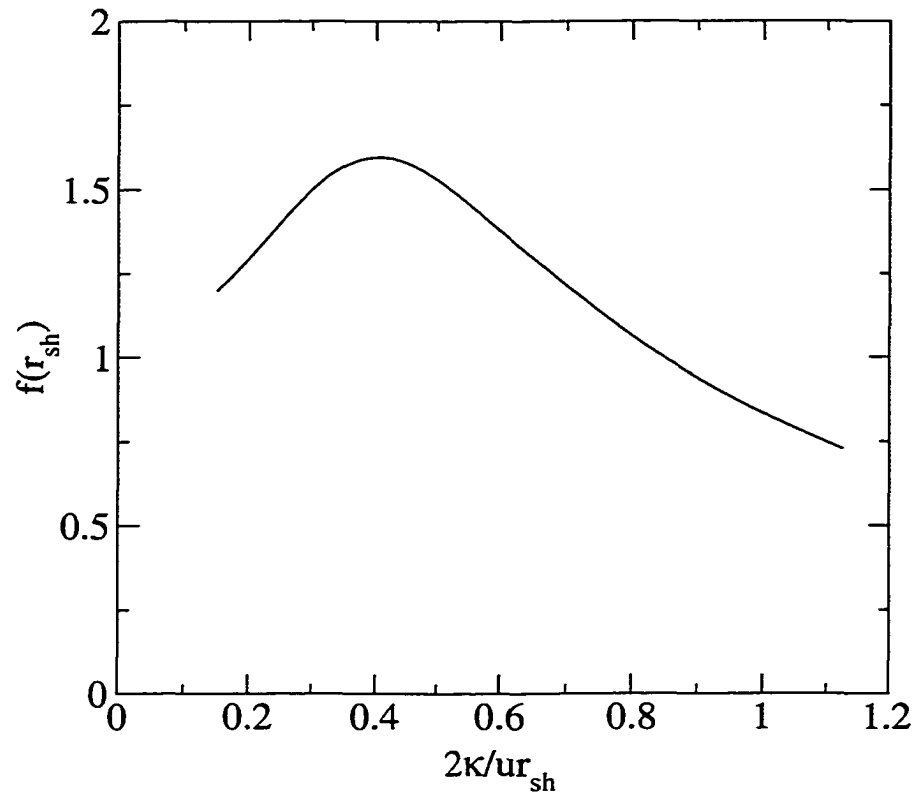


Figure B.2 Particle concentration at the source, according to Eq. (B.4). The maximum occurs near the energy (or diffusion κ) where the shock parameter is close to 1.

$\kappa_0=0$ downstream and cannot be directly compared with Fig. B.1. However, the bump was present in these simulations as well. This let us to believe that the bump is indeed a spectral feature rather than an artifact.

At this point it is useful to find an analytic solution to the transport equation in the absence of the shock or cooling, thus ignoring the momentum dependence in f . This problem is similar to the diffusion and convection of smoke from a chimney of constant output Q , but in the spherical geometry. With constant u and k , the transport equation can be written as

$$\frac{d^2 f}{dr^2} + \left(\frac{2}{r} - a \right) \frac{df}{dr} = -\frac{Q}{\kappa} \delta(r - r_{sh}) \quad (\text{B.3})$$

where $a=u/\kappa$. The boundary conditions for Eq. (B.3) are $f(r_1)=f(r_2)=0$, where r_1 and r_2 are the lower and upper boundaries, respectively. The source is located at r_{sh} , i.e., where a shock would normally be. The solution to (B.3) can be easily found to be

$$f(r) = \begin{cases} \frac{Q r_{sh}^2 e^{-ar} (\Phi(r_2) - \Phi(r_{sh})) (\Phi(r) - \Phi(r_1))}{k (\Phi(r_2) - \Phi(r_1))}, & r < r_{sh} \\ \frac{Q r_{sh}^2 e^{-ar} (\Phi(r_2) - \Phi(r)) (\Phi(r_{sh}) - \Phi(r_1))}{k (\Phi(r_2) - \Phi(r_1))}, & r > r_{sh} \end{cases}, \quad (\text{B.4})$$

where the function Φ is defined

$$\Phi(r) = a Ei(ar) - \frac{e^{ar}}{r}, \quad (\text{B.5})$$

where $Ei(x)$ is the exponential integral (Jeffrey, 1995).

The solution (B.4) depends parametrically on the ratio $2\kappa/ur_{sh}$, (shock parameter) and, hence, on particle energy. In any case, there is a maximum at the source. In Figure B.2

we plotted $f(r_{sh})$ as a function of the shock parameter. The graph shows a maximum at $2\kappa/ur_{sh} \sim 0.4$, which is close to 1. The physical interpretation of this effect is that the effective advection speed, $u - 2\kappa/r$ becomes close to 0, in which case the transport of particles from the source is inhibited, resulting in a higher concentration near the source.

While the actual situation with ACRs is considerably more complicated due to acceleration and cooling, the same effect can act to enhance the spectra at certain energies. The bump in the numerical simulation described earlier does occur below the energy where $2\kappa/ur_{sh} = 1$ (Fig. B.1). In reality, of course, there is no source of constant strength at the shock, therefore one has to be very careful when drawing analogies between this simple analytic solution and the actual case.

The distance to the far boundary has the following effect on the bump. When this distance is small, the cutoff happens at lower energies because of particles escaping through the boundary. The bump is not visible in this case, because its location is set by the upstream shock parameter. We see the bump only when the distance to the boundary is large enough, so that the cutoff is also determined by the upstream shock parameter.

LIST OF ACRONYMS USED IN THE TEXT

ACR	anomalous cosmic ray.
AMR	adaptive mesh refinement.
BC	boundary condition.
CIR	corotating interaction region.
CR	cosmic ray.
GCR	galactic cosmic ray.
GMIR	global merged interaction region.
HNS	heliospheric neutral sheet.
HP	heliopause.
LISM	local interstellar medium.
MF	magnetic field.
MHD	magnetohydrodynamic.
PSD	phase space density.
PUI	pickup ion.
QLT	quasi-linear theory.
SW	solar wind.
TS	termination shock.

REFERENCES

- Axford, W. I., The interaction of the solar wind with the interstellar medium, in *Solar Wind*, eds. Sonnett, C. P., Coleman, Jr., P. J., and Wilcox, J. M., NASA, 1972.
- Axford, W. I., Leer, E., and McKenzie, J. F., The structure of cosmic ray shocks, *Astron. Astrophys.*, **111**, 317, 1982.
- Axford, W. I., and McKenzie, J. F., The solar wind, in *Cosmic Winds and the Heliosphere*, eds. Jokipii, J. R., Sonett, C. P., and Giampapa, M. S., Tucson: University of Arizona press, 1997.
- Axford, W. I., and Newman, R. C., The effect of cosmic ray friction on the solar wind, *Proc. 9 Int. Cosmic Ray Conf.*, **1**, 173, 1965.
- Baranov, V. B., and Malama, Yu. G., Model of the solar wind interaction with the local interstellar medium: numerical solution of self-consistent problem, *J. Geophys. Res.*, **98**, 15,157, 1993.
- Barnes, A., Shape of the heliospheric termination shock: effects of latitude variations of solar wind dynamic pressure, *J. Geophys. Res.*, **103**, 2015, 1998.
- Berger, M. J., Data structures for adaptive grid generation, *SIAM J. Sci. Stat. Comput.*, **7**, 904, 1986.
- Berger, M. J., and Colella, P., Local adaptive mesh refinement for shock hydrodynamics, *J. Comput. Phys.*, **82**, 64, 1989.
- Berger, M. J., and Olinger, J., Adaptive mesh refinement for hyperbolic partial differential equations, *J. Comput. Phys.*, **53**, 484, 1984.
- Biermann, P. L., The origin of cosmic rays, *Space Sci. Rev.*, **74**, 385, 1995.
- Braginskii, S. I., Transport processes in a plasma, in *Reviews of Plasma Physics*, Vol 1, ed. Leontovich, M. A., New York: Consultants Bureau, 1965.
- Burger, R. A., and Hattingh, M., Steady-state drift-dominated models modulation models for galactic cosmic rays, *Astrophys. Space Sci.*, **230**, 375, 1995.
- Burger, R. A., and Hattingh, M., Towards a realistic diffusion tensor for galactic cosmic rays, *Astrophys. J.*, **505**, 244, 1998.
- Burger, R. A., and Potgieter, M. S., The calculation of neutral sheet drift in two-

dimensional cosmic-ray modulation models, *Astrophys. J.*, **339**, 501, 1989.

Burgers, J. M., Flow equations for composite gases, New York: Academic Press, 1969.

Chalov, S. V., and Fahr, H. R., A three-fluid model of the solar wind termination shock including a continuous production of anomalous cosmic rays, *Astron. Astrophys.*, **311**, 317, 1996.

Chalov, S. V., and Fahr, H. R., A two-fluid model of the solar wind termination shock modified by shock-generated cosmic rays including energy losses, *Astron. Astrophys.*, **288**, 973, 1994.

Colella, P., Multidimensional upwind methods for hyperbolic conservation laws, *J. Comput. Phys.*, **87**, 171, 1990.

Cummings, A. C., and Stone, E. C., Anomalous cosmic rays and solar modulation, *Space Sci. Rev.*, **83**, 51, 1998.

Dolginov, A. Z., and Topygin, I. N., Cosmic rays in the interplanetary magnetic fields, *Icarus*, **8**, 54, 1968.

Donohue, D. J., and Zank, G. P., Steady state and dynamical structure of a cosmic-ray-modified termination shock, *J. Geophys. Res.*, **98**, 19,005, 1993.

Drury, L. O'C., An introduction to the theory of diffusive shock acceleration of energetic particles in tenuous plasmas, *Rep. Prog. Phys.*, **46**, 973, 1983.

Drury, L. O'C., and Falle, S. A. E. G., On the stability of shocks modified by particle acceleration, *Mon. Not. Royal Astron. Soc.*, **223**, 353, 1986.

Drury, L. O'C., Völk, H. J., Hydromagnetic shock structure in the presence of cosmic rays, *Astrophys. J.*, **248**, 344, 1981.

Einfeldt, B., Munz, C. D., Roe, P. L., and Sjogreen, B., On Godunov-type methods near low densities, *J. Comput. Phys.*, **92**, 273, 1991.

Duffy, P., Drury, L. O'C., and Völk, H. J., Cosmic ray hydrodynamics at shocks fronts, *Astron. Astrophys.*, **291**, 613, 1994.

Ellison, D. C., Baring, M. G., and Jones, F. C., Nonlinear particle acceleration in oblique shocks, *Astrophys. J.*, **473**, 1029, 1996.

Fahr, H. J., Fichtner, H., and Grzedzielski, S., The influence of the anomalous cosmic-ray component on the dynamics of the solar wind, *Solar Phys.*, **137**, 355, 1992.

- Fahr, H. J., Kausch, T., and Scherer, H., A 5–fluid hydrodynamic approach to model the solar system–interstellar medium interaction, *Astron. Astrophys.*, **357**, 268, 2000.
- Falle, S. A. E. G., and Giddings, J. R., Time–dependent cosmic ray modified shocks, *Mon. Not. Royal. Astr. Soc.*, **225**, 399, 1987.
- Fichtner, H., Production of Energetic Particles at the Heliospheric Shock, *Rev. Modern Astr.*, **9**, 191, 1996.
- Fisk, L. A., The interactions of energetic particles with the solar wind, in *Solar system plasma physics*, eds. Kennel, C. F., Lanzerotti, L. J., and Parker, E. N., **1**, Amsterdam: North–Holland, 1979.
- Fisk, L. A., Forman, M. A., and Axford, W. I., Solar modulation of galactic cosmic rays. 3. Implications of the Compton–Getting coefficient, *J. Geophys. Res.*, **78**, 995, 1973.
- Fisk, L. A., Gleeson, L. J., and Axford, W. I., Approximation in the theory of solar–cycle modulation, *Proc. 11 Int. Cosmic Ray Conf.*, **2**, 105, 1969.
- Fisk, L. A., Kozlovsky, B., and Ramaty, R., An interpretation of the observed oxygen and nitrogen enhancements in low–energy cosmic rays, *Astrophys. J.*, **190**, L115, 1974.
- Fite, W. L., Smith, A. C. H., and Stebbings, R. F., Charge transfer in collisions involving symmetric and asymmetric resonance, *Proc. Royal Soc. London, Ser A.*, **268**, 527, 1962.
- Fletcher, C. A. J., Computational techniques for fluid dynamics, Berlin: Springer–Verlag, 1988.
- Florinski, V., and Jokipii, J. R., Solar–wind acceleration by energetic particles, *Geophys. Res. Lett.*, **24**, 2383, 1997.
- Florinski, V., and Jokipii, J. R., A two–dimensional, self–consistent model of galactic cosmic rays in the heliosphere, *Astrophys. J.*, **523**, L185, 1999.
- Florinski, V. and Jokipii, J. R., Do anomalous cosmic rays modify the termination shock?, *Astrophys. J.*, in preparation, 2001.
- Forman, M. A., Jokipii, J. R., and Owens, A. J., Cosmic–ray streaming perpendicular to the mean magnetic field, *Astrophys. J.*, **192**, 535, 1974.
- Frisch, P. C., The interstellar cloud surrounding the solar system, in *Cosmic Winds and the Heliosphere*, eds. Jokipii, J. R., Sonett, C. P., and Giampapa, M. S., Tucson: University of Arizona press, 1997.
- Garcia–Munoz, M., Mason, G. M., and Simpson, J. A., The anomalous ^4He component

in the cosmic-ray spectrum at ≤ 50 MeV per nucleon during 1972–1974, *Astrophys. J.*, **202**, 265, 1975.

Giacalone, J., and Jokipii, J. R., Injection and acceleration of pickup ions at the termination shock, *Space Sci. Rev.*, **83**, 282, 1998.

Giacalone, J., and Jokipii, J. R., The transport of cosmic rays across a turbulent magnetic field, *Astrophys. J.*, **520**, 204, 1999.

Giacalone, J., Jokipii, J. R., Decker, R. B., Krimigis, S. M., Scholer, M., and Kucharek, H., Preacceleration of anomalous cosmic rays in the inner heliosphere, *Astrophys. J.*, **486**, 471, 1997.

Giacalone, J., Jokipii, J. R., and Kota, J., Ion injection and acceleration at quasi-perpendicular shocks, *J. Geophys. Res.*, **99**, 19,351, 1994.

Gleeson, L. J., The equations describing the cosmic-ray gas in the interplanetary region, *Planet. Space Sci.*, **17**, 31, 1969.

Gleeson, L. J., and Axford, W. I., Cosmic rays in the interplanetary medium, *Astrophys. J.*, **149**, L115, 1967.

Gleeson, L. J., and Axford, W. I., Solar modulation of galactic cosmic rays, *Astrophys. J.*, **154**, 1011, 1968.

Gloeckel, G., Composition of energetic particle populations in interplanetary space, *Rev. Geophys. Space Phys.*, **17**, 569, 1979.

Gloeckler, G., Fisk, L. A., and Geiss, J., Anomalously small magnetic field in the local interstellar cloud, *Nature*, **386**, 374, 1997.

Godunov, S. E., Zabrodin, A. V., and Prokopov, G. P., A differencing scheme for two-dimensional nonstationary fluid mechanical problems and computing of a flow with a departed shock wave, *J. Comput. Math. Math. Phys.*, **1**, 1020, 1961 (in Russian).

Goldstein, B. E., Neugebauer, M., Phillips, J. L., Bame, S., Gosling, J. T., McComas, D., Wang, Y.-M., Sheeley, N. R., and Suess, S. T., Ulysses plasma parameters: latitudinal, radial, and temporal variations, *Astron. Astrophys.*, **316**, 296, 1996.

Gombosi, T. I., Powell, K. G., and De Zeeuw, D. L., Axisymmetric modelling of cometary mass loading on an adaptively refined grid, *J. Geophys. Res.*, **99**, 21,525, 1994.

Haasbroek, L. J. and Potgieter, M. S., The modulation of cosmic rays in the high latitude heliosphere: a computer simulation, *Space Sci. Rev.*, **72**, 385, 1995.

- Harten, A., Lax, P. D., and Van Leer, B., On upstream differencing and Godunov-type schemes for hyperbolic conservation laws, *SIAM Rev.*, **25**, 35, 1983.
- Heber, B., Dröge, W., Ferrando, P., Haasbroeck, L. J., Kunow, H., Müller-Mellin, R., Paizis, C., Potgieter, M. S., Raviart, A., and Wibberenz, G., Spatial variation of >40 MeV/n nuclei fluxes observed during the Ulysses rapid latitude scan, *Astron. Astrophys.*, **316**, 538, 1996.
- Hollweg, J. V., Transverse Alfvén waves in the solar wind: arbitrary \mathbf{k} , v_0 , \mathbf{B}_0 , and $|\delta\mathbf{B}|$, *J. Geophys. Res.*, **79**, 1539, 1974.
- Holzer, T. E., Interaction of the solar wind with the neutral component of the interstellar gas, *J. Geophys. Res.*, **77**, 5407, 1972.
- Holzer, T. E., and Axford, W. I., The theory of stellar winds and related flows, *Ann. Rev. Astron. Astrophys.*, **8**, 31, 1970.
- Isenberg, P. A., Interaction of the solar wind with interstellar neutral hydrogen: three-fluid model, *J. Geophys. Res.*, **91**, 9965, 1986.
- Isenberg, P. A., and Jokipii, J. R., Gradient and curvature drift in magnetic field with arbitrary spatial variation, *Astrophys. J.*, **234**, 746, 1979.
- Izmodenov, V. V., Nodulation of galactic cosmic rays in the region of interaction of the local interstellar medium with the solar wind: hydrodynamic approximation, *Astronomy Lett.*, **23**, 221, 1997.
- Jeffrey, A., Handbook of mathematical formulas and integrals, San Diego: Academic Press, 1995.
- Johansen, H., and Colella, P., A cartesian grid embedded boundary method for Poisson's equation on irregular domains, *J. Comput. Phys.*, **147**, 60, 1998.
- Jokipii, J. R., Cosmic-ray propagation. I. Charged particles in a random magnetic field, *Astrophys. J.*, **146**, 480, 1966.
- Jokipii, J. R., Particle drift, diffusion, and acceleration at shocks, *Astrophys. J.*, **255**, 716, 1983.
- Jokipii, J. R., Particle Acceleration at a termination shock. I. Application to the solar wind and the anomalous component, *J. Geophys. Res.*, **91**, 2929, 1986.
- Jokipii, J. R., Rate of energy gain and maximum energy in diffusive shock acceleration, *Astrophys. J.*, **313**, 842, 1987.

- Jokipii, J. R., Constraints on the acceleration of anomalous cosmic rays, *Astrophys. J.*, **393**, L41, 1992.
- Jokipii, J. R., and Giacalone, J., The theory of anomalous cosmic rays, *Space Sci. Rev.*, **83**, 123, 1998.
- Jokipii, J. R., and Kopriva, D. A., Effects of particle drift on the transport of cosmic rays. III. Numerical models of galactic cosmic-ray modulation, *Astrophys. J.*, **234**, 384, 1979.
- Jokipii, J. R., and Kota, J., The energy spectrum of anomalous cosmic rays, *Proc. 25 Int. Cosmic Ray Conf*, **2**, 229, 1997.
- Jokipii, J. R., Kota, J., Giacalone, J., Horbury, T. S., and Smith, E. J., Interpretation and consequences of large-scale magnetic variances observed at high heliographic latitudes, *Geophys. Res. Lett.*, **22**, 3385, 1995.
- Jokipii, J. R., and Morfill, G. M., Cosmic rays and the acceleration of the solar wind, *Proc. 23 Int. Cosmic Ray Conf*, **3**, 179, 1993.
- Jones, F. C., Baring, M. G., and Ellison, D. C., The acceleration of pick-up ions at the solar wind termination shock: a non-linear Monte Carlo calculation, *Space Sci. Rev.*, **83**, 278, 1998.
- Jones, F. C., and Ellison, D. C., The plasma physics of shock acceleration, *Space Sci. Rev.*, **58**, 259, 1991.
- Jones, T. W., and Kang, H., Time-dependent evolution of cosmic-ray-mediated shocks in the two-fluid model, *Astrophys. J.*, **363**, 499, 1990.
- Kang, H., and Jones, T. W., Diffusive cosmic-ray acceleration: two-fluid models with in situ injection, *Astrophys. J.*, **353**, 149, 1990.
- Ko, C. M., and Webb, G. M., Cosmic-ray-modified stellar winds. I. Solution topologies and singularities, *Astrophys. J.*, **323**, 657, 1987.
- Ko, C. M., and Webb, G. M., Cosmic-ray-modified stellar winds. II. A perturbation approach, *Astrophys. J.*, **325**, 296, 1988.
- Ko, C. M., Jokipii, J. R., and Webb, G. M., Cosmic-ray-modified stellar winds. III. A numerical iterative approach, *Astrophys. J.*, **326**, 761, 1988.
- Kota, J., and Jokipii, J. R., Cosmic-ray gradients in the outer heliosphere, *Adv. Space Res.*, **13**, (6)257, 1993.
- Kucharek, H., and Scholer, M., Injection and acceleration of interstellar pickup ions at

the heliospheric termination shock, *J. Geophys. Res.*, **100**, 1745, 1995.

Landau, L. D., and Lifshitz, E. M., *Gidrodinamika (Fluid Mechanics)*, Moscow: Nauka, 1988.

Lapidus, L., Pinder, G. F., *Numerical solutions of partial differential equations in science and engineering*, New York: John Wiley & Sons, 1982.

Lee, M. A., Effects of cosmic rays and interstellar gas on the dynamics of a wind, in *Cosmic Winds and the Heliosphere*, eds. Jokipii, J. R., Sonett, C. P., and Giampapa, M. S., Tucson: University of Arizona press, 1997.

Lee, M. A., and Axford, W. I., Model structure of a cosmic-ray mediated stellar or solar wind, *Astron. Astrophys.*, **194**, 297, 1988.

le Roux, J. A., and Fichtner, H., A self-consistent determination of the heliospheric termination shock structure in the presence of pickup, anomalous, and galactic cosmic ray protons, *J. Geophys. Res.*, **102**, 17,365, 1997.

le Roux, J. A., Potgieter, M. S., and Ptuskin, V. S., A transport model for the diffusive shock acceleration and modulation of anomalous cosmic rays in the heliosphere, *J. Geophys. Res.*, **101**, 4791, 1996.

le Roux, J. A., and Ptuskin, V. S., Galactic cosmic-ray mediation of a spherical solar wind flow. I. The steady state cold gas hydrodynamical approximation, *Astrophys. J.*, **438**, 427, 1995a.

le Roux, J. A., and Ptuskin, V. S., Galactic cosmic-ray mediation of a spherical solar wind flow. II. The steady state hydromagnetic approximation, *Astrophys. J.*, **452**, 423, 1995b.

le Roux, J. A., and Ptuskin, V. S., The self-consistent stochastic pre-acceleration of pickup ions in the heliosphere, *Space Sci. Rev.*, **83**, 286, 1998.

le Roux, J. A., Zank, G. P., and Ptuskin, V. S., An evaluation of perpendicular diffusion models regarding cosmic ray modulation on the basis of a hydromagnetic description for solar wind turbulence, *J. Geophys. Res.*, **104**, 24,845, 1999.

Linde, T. J., Gombosi, T. I., Roe, P. L., Powell, K. G., and DeZeeuw, D. L., Heliosphere in the magnetized local interstellar medium: results of a three-dimensional MHD simulation, *J. Geophys. Res.*, **103**, 1889, 1998.

Lockwood, J. A., Webber, W. R., and Hoeksema, J. T., Interplanetary cosmic ray latitudinal gradients in 1984 to 1987 using IMP 8 and Voyager data, *J. Geophys. Res.*, **93**, 7521, 1988.

McDonald, F. B., Cosmic-ray modulation in the heliosphere: A phenomenological study, *Space Sci. Rev.*, **83**, 33, 1998.

McDonald, F. B., Heikkila, B., Lal, N., and Stone, E. C., The relative recovery of galactic and anomalous cosmic rays in the distant heliosphere: evidence for modulation in the heliosheath, *J. Geophys. Res.*, **105**, 1, 2000.

McDonald, F. B., Teegarden, B. J., Trainor, J. H., and Webber, W. R., The anomalous abundance of cosmic-ray nitrogen and oxygen nuclei at low energies, *Astrophys. J.*, **187**, L105, 1974.

McKee, S., and Mitchell, A. R., Alternating direction methods for parabolic equations in two space dimensions with a mixed derivative, *Computer J.*, **13**, 81, 1970.

McNutt Jr, R. L., Lyon, J., and Goodrich, C. C., Simulation of the heliosphere: Model, *J. Geophys. Res.*, **103**, 1905, 1998.

McNutt Jr, R. L., Lyon, J., and Goodrich, C. C., Simulation of the heliosphere: Generalized charge-exchange cross section, *J. Geophys. Res.*, **104**, 14,803, 1999.

McNutt Jr, R. L., Lyon, J., Goodrich, C. C., and Wiltberger, M., 3D MHD simulations of the heliosphere-VLSM interaction, in *Solar Wind Nine*, ed. Habbal, S. R., Esser, R., Hollweg, J. V., and Isenberg, P. A., American Institute of Physics, New York, 1999.

Meyer, P., Cosmic rays in the galaxy, *Ann. Rev. Astron. Astrophys.*, **7**, 1, 1969.

Myasnikov, A. V., Alexashov, D. B., Izmodenov, V. V., and Chalov, S. V., Self-consistent model of the solar wind interaction with three-component circumsolar interstellar cloud: Mutual influence of thermal plasma, galactic cosmic rays and H atoms, *J. Geophys. Res.*, **105**, 5167, 2000.

Myasnikov, A. V., Izmodenov, V. V., Alexashov, D. B., and Chalov, S. V., Self-consistent model of the solar wind interaction with two-component circumsolar interstellar cloud: Mutual influence of thermal plasma and galactic cosmic rays, *J. Geophys. Res.*, **105**, 5179, 2000.

Nerney, S., Suess, S. T., and Schmahl, E. J., Flow downstream of the heliospheric terminal shock: the magnetic field on the heliopause, *J. Geophys. Res.*, **98**, 15,169, 1993.

Owens, A. J., and Jokipii, J. R., Cosmic-ray modulation by an angle-dependent solar wind, *Astrophys. J.*, **167**, 169, 1971.

Palmer, I. D., Transport coefficients of low-energy cosmic rays in interplanetary space, *Rev. Geophys. Space Phys.*, **20**, 335, 1982.

- Parker, E. N., The hydrodynamic theory of solar corpuscular radiation and stellar winds, *Astrophys. J.*, **132**, 821, 1960.
- Parker, E. N., Interplanetary dynamical processes, New York: Wiley Interscience, 1963.
- Parker, E. N., Dynamical theory of the solar wind, *Space Sci. Rev.*, **4**, 666, 1965.
- Pauls, H. L., and Zank, G. P., Interaction of a nonuniform solar wind with the local interstellar medium, *J. Geophys. Res.*, **101**, 17,081, 1996.
- Pauls, H. L., Zank, G. P., and Williams, L. L., Interaction of the solar wind with the local interstellar medium, *J. Geophys. Res.*, **100**, 21,595, 1995.
- Potgieter, M. S., Time-dependent cosmic-ray modulation: role of drifts and interaction regions, *Adv. Space Res.*, **13**, (6)239, 1993.
- Potgieter, M. S., The long-term modulation of galactic cosmic rays in the heliosphere, *Adv. Space Res.*, **16**, (9)191, 1995.
- Potgieter, M. S., The modulation of galactic cosmic rays in the heliosphere: theory and models, *Space. Sci. Rev.*, **83**, 147, 1998.
- Potgieter, M. S., le Roux, J. A., and Burger, R. A., Interplanetary cosmic ray gradients with steady state modulation models, *J. Geophys. Res.*, **94**, 2323, 1989.
- Potgieter, M. S., and Moraal, H., A drift model for the modulation of galactic cosmic rays, *Astrophys. J.*, **294**, 425, 1985.
- Potgieter, M. S., and Moraal, H., Acceleration of cosmic rays in the solar wind termination shock. I. A steady state technique in a spherically symmetric models, *Astrophys. J.*, **330**, 445, 1988.
- Quémerais, E., Malama, Y. G., Sandel, B. R., Lallement, R., Bertaux, J-L, and Baranov, V. P., Outer heliosphere Lyman α background derived from two-shock model hydrogen distribution: application to the Voyager UVS data, *Astron. Astrophys.*, **308**, 279, 1996.
- Roe, P. L., Approximate Riemann solvers, parameter vectors, and difference schemes, *J. Comput. Phys.*, **43**, 357, 1981.
- Rossi, B and Olbert, S., Introduction to the physics of space, New York: McGraw-Hill, 1970.
- Sanuki, T., Motoki, M., Matsumoto, H., Seo, E. S., Wang, J. Z., Abe, K., Anraku, K., Asaoka, Y., Fujikawa, M., Imori, M., Ishino, M., Maeno, T., Makida, Y., Matsui, N., Matsunaga, H., Mitchell, J., Mitsui, T., Moiseev, A., Nishimura, J., Nozaki, M., Orito,

S., Ormes, J., Saeki, T., Sasaki, M., Shikaze, Y., Sonoda, T., Streitmatter, R., Suzuki, J., Tanaka, K., Ueda, I., Yajima, N., Yamagami, T., Yamamoto, A., Yoshida, T., Yoshimura, K., A precise measurement of cosmic-ray proton spectrum with BESS spectrometer, *Proc. 26 Int. Cosmic Ray Conf*, **3**, 93, 1999.

Seo, E. S., Ormes, J. F., Streitmatter, R. E., Stochaj, S. J., Jones, W. V., Stephens, S. A., and Bowen, T., Measurement of cosmic-ray proton and helium spectra during the 1987 solar minimum, *Astrophys. J.*, **378**, 763, 1991.

Steenberg, C. D., Cummings, A. C., and Stone, E. C., Drift calculations on the modulation of anomalous cosmic rays during the 1998 solar minimum period, *Proc. 26 Int. Cosmic Ray Conf*, **7**, 593, 1999.

Stone, E. C., and Cummings, A. C., The distance to the solar wind termination shock in 1993 and 1994 from observations of anomalous cosmic rays, *J. Geophys. Res.*, **101**, 11,017, 1996.

Stone, E. C., Cummings, A. C., Hamilton, D. C., Hill, M. E., and Krimigis, S. M., Voyager observations of anomalous and galactic cosmic rays during 1998, *Proc. 26 Int. Cosmic Ray Conf*, **7**, 551, 1999.

Sturrock, P. A., Plasma physics: an introduction to the theory of astrophysical, geophysical, and laboratory plasmas, Cambridge: Cambridge University Press, 1994.

Suess, S. T., The heliopause, *Rev. Geophys.*, **28**, 97, 1990.

Suess, S. T., Hathaway, D. H., and Dessler, A. J., Asymmetry of the heliosphere, *Geophys. Res. Lett.*, **14**, 977, 1987.

Suess, S. T., and Nerney, S., The termination shock and the heliosheath, in *Cosmic Winds and the Heliosphere*, eds. Jokipii, J. R., Sonett, C. P., and Giampapa, M. S., Tucson: University of Arizona press, 1997.

Valylius, V. M., and Siscoe, G. L., On the flux and the energy spectrum of interstellar ions in the solar system, *J. Geophys. Res.*, **81**, 1247, 1976.

Wang, C., Richardson, J. D., and Gosling, J. T., Slowdown of the solar wind in the outer heliosphere and the interstellar neutral hydrogen density, *Geophys. Res. Lett.*, **27**, 2429, 2000.

Whang, Y. C., Burlaga, L. F., and Ness, N. F., Locations of the termination shock and the heliopause, *J. Geophys. Res.*, **100**, 17,015, 1995.

Webb, G. M., Separation of steady-state cosmic ray equation of transport: a generalization, *Astrophys. Space Sci.*, **81**, 215, 1982.

Webb, G. M., Forman, M. A., and Axford, W. I., Cosmic-ray acceleration at stellar wind terminal shocks, *Astrophys. J.*, **298**, 684, 1985.

Webb, G. M., and Gleeson, L. J., Galactic cosmic rays in the finite solar cavity, *Proc. Astron. Soc. Australia*, **2**, 299, 1977.

Webb, G. M., Zank, G. P., Ko, C. M., and Donohue, D. J., Multidimensional Green's function and the statistics of diffusive shock acceleration, *Astrophys. J.*, **453**, 178, 1995.

Webber, W. R., and Lockwood, J. A., Interplanetary radial cosmic-ray gradients and their implication for a possible large modulation effect at the heliospheric boundary, *Astrophys. J.*, **317**, 534, 1987.

Webber, W. R., and Lockwood, J. A., Intensities of anomalous and galactic cosmic rays in the outer heliosphere near heliospheric equator in 1987 and during the period from 1994 to 1996, *J. Geophys. Res.*, **102**, 9773, 1997.

Webber, W. R., Potgieter, M. S., and Burger, R. A., A comparison of predictions of a wavy neutral sheet drift model with cosmic-ray data over a whole modulation cycle: 1976–1987, *Astrophys. J.*, **349**, 634, 1990.

Zank, G. P., The large-scale structure of the heliosphere, in *Solar Wind Nine*, ed. Habbal, S. R., Esser, R., Hollweg, J. V., and Isenberg, P. A., American Institute of Physics, New York, 1999.

Zank, G. P., Matthaeus, W. H., Bieber, J. W., and Moraal, H., The radial and latitudinal dependence of the cosmic ray diffusion tensor in the heliosphere, *J. Geophys. Res.*, **103**, 2085, 1998.

Zank, G. P., Matthaeus, W. H., and Smith, C. W., Evolution of turbulent magnetic fluctuation power with heliospheric distance, *J. Geophys. Res.*, **101**, 17,093, 1996.

Zank, G. P., and Pauls, H. L., Shock propagation in the outer heliosphere, *J. Geophys. Res.*, **102**, 7037, 1997.

Zank, G. P., Pauls, H. L., Cairns, I. H., and Webb, G. M., Interstellar pickup ions and quasi-perpendicular shocks: implications for the termination shock and interplanetary shocks, *J. Geophys. Res.*, **101**, 457, 1998.

Zank, G. P., Webb, G. M., and Donohue, D. J., Particle injection and the structure of energetic-particle-modified shocks, *Astrophys. J.*, **406**, 67, 1993.